Evolution of radiation induced defects in SiC:

A multiscale simulation approach

by

Hao Jiang

A dissertation submitted in partial fulfillment of

the requirements for the degree of

Doctor of Philosophy

(Materials Science)

at the

University of Wisconsin-Madison

2017

Date of final oral examination: 06/09/2017

The dissertation is to be approved by the following members of the Final Oral Committee:

Izabela Szlufarska, Professor, Department of Materials Science and Engineering

Dane Morgan, Professor, Department of Materials Science and Engineering

Paul Voyles, Professor, Department of Materials Science and Engineering

Jake Blanchard, Professor, Department of Engineering Physics

Kumar Sridharan, Professor, Department of Engineering Physics

Acknowledgement

Pursing a Ph.D. degree is a valuable life experience. Along this journey, I have received supports, guidance and helps from many great people in both work and life.

First, I would like to sincerely thank Prof. Izabela Szlufarska for the Ph.D. opportunity in her group, for her guidance on the interesting and challenging research projects, and for all her supports on my career developments. I'm very grateful to Prof. Szlufarska for the offer of a research assistance position to work in her team on nuclear materials using atom simulations. This has been my primary research interest in my senior year after completing a minor project on nuclear materials and taking a course on atom simulations. Her broad knowledge in this field and extensive experience in simulations have helped to navigate research directions, to overcome challenges and to finish these projects with fruitful outputs. Her hardworking spirit also motivated me over the years in Madison and will always do so in the future. Prof. Szlufarska has been very supportive regarding my career development. I received valuable helps from her on revising resume, referral for positions, and supports for internships.

I also would like to thank the committee members, Prof. Dane Morgan, Prof. Paul Voyles, Prof. Jake Blanchard, and Prof. Kumar Sridharan for being on my thesis committee. Through meetings with them, I have received many insightful suggestions and comments on my research projects. I appreciate Prof. Dane Morgan for his suggestions and ideas to highlight the motivations and implications of research projects. I want to thank Prof. Paul Voyles on his helps to interpret electron microscopy data and to conduct microscopy image simulations. I acknowledge Prof. Jake Blanchard and Prof. Kumar Sridharan for their insights and comments from the perspective of nuclear engineering.

In my first two years in Madison, I have the honor to work with Dr. Chao Jiang and Dr. Mingjie Zheng. They taught me lots of simulation methods and provided hands-on tutorial on several simulation tools. I sincerely thank them for their patience and time. I also want to thank the group members in Computational Materials Group for years' valuable discussions, technical support and assistance. I acknowledge the support from the funding source of Deport of Energy, Office of Basic Energy Sciences Grant No. DE-FG02-08ER46493.

I want to thank Dr. Derek Stewart and Western Digital RAMP program for the internship experience at Western Digital Corporation. It was a great opportunity to get exposed to the vast semiconductor industry in the bay area. I have learnt lots of knowledge on semiconductor materials, memory technologies, and simulation techniques through this experience. The work spirit and life style of colleagues inside the company have inspired me to work more efficiently and to seek better life-work balance.

Last but most importantly, I want to send my deepest gratefulness to my parents, Deju Jiang and Haijuan Xing, to my sister, Lei Jiang, and to my lovely nice, Xinyu Jiang. I cannot complete the Ph.D. degree without their continual supports, encouragement and love. This thesis is dedicated to them. I also want to thank my girlfriend Ni Zhang for her extraordinary supports and patience along this journey. My life has become more and more colorful and joyful ever since I met her.

Abstract

Because of many excellent properties, SiC has been proposed for many applications in nuclear reactors including the cladding layer in fuel rod, fission products container in TRISO fuel, and first wall/blanket in magnetic controlled fusion reactors. Upon exposure to high energy radiation environments, point defects and defect clusters are generated in materials in amounts significantly exceeding their equilibrium concentrations. The accumulation of defects can lead to undesired consequences such as crystalline-to-amorphous transformation, swelling, and embrittlement, and these phenomena can adversely affect the performance of SiC based components in nuclear reactors. It is of great importance to understand the accumulation process of these defects in order to estimate change in properties of this material and to design components with superior ability to withstand radiation damages.

Defect clusters are widely observed in SiC irradiated at the operation temperatures of various reactors. These clusters are believed to cause more than half of the overall swelling of irradiated SiC and can potentially lead to lowered thermal conductivity and mechanical strength. It is critical to understand the formation and growth of these clusters. Diffusion of these clusters is one importance piece to determine the growth rate of clusters; however it is unclear so far due to the challenges in simulating rare events. Using a combination of kinetic Activation Relaxation Technique with empirical potential and ab initio based climbing image nudged elastic band method, I performed an extensive search of the migration paths of the most stable carbon tri-interstitial cluster in SiC. This research reveals paths with the lowest energy barriers to migration, rotation, and dissociation of the most stable interstitial cluster in SiC. Based on these energy barriers, I concluded defect clusters are thermally immobile at temperatures lower than 1500 K and can dissociate into smaller clusters and single interstitials at temperatures beyond that.

Even though clusters cannot diffuse by thermal vibrations, it is found that they can migrate at room temperature under the influence of electron radiation. This discovery was enabled by the collaboration with electron microscopy scientists within the department and I contributed to this project by data analysis and model building. This is the first direct observation of radiation-induced diffusion of defect clusters in bulk materials. We show that the underlying mechanism of this athermal diffusion is elastic collision between incoming electrons and cluster atoms. Our findings suggest that defect clusters may be mobile under certain irradiation conditions, changing current understanding of cluster annealing process in irradiated SiC. With the knowledge of cluster diffusion in SiC demonstrated in this thesis, we now become able to predict cluster evolution in SiC with good agreement with experimental measurements. This ability can enable us to estimate changes in many properties of irradiated SiC relevant for its applications in reactors.

Internal interfaces such as grain boundaries can behave as sinks to radiation induced defects. The ability of GBs to absorb, transport, and annihilate radiation-induced defects (sink strength) is important to understand radiation response of polycrystalline materials and to better design interfaces for improved resistance to radiation damage. Nowadays, it is established GBs' sink strength is not a static property but rather evolves with many factors, including radiation environments, grain size, and GB microstructure. In this thesis, I investigated the response of small-angle tilt and twist GBs to point defects fluxes in SiC. First of all, I found the pipe diffusion of interstitials in tilt GBs is slower than bulk diffusion. This is because the increased interatomic distance at dislocation cores raises the migration barrier of interstitial dumbbells. Furthermore, I show that both the annihilation of interstitials at jogs and jog nucleation from clusters are diffusion-controlled and can occur under off-stoichiometric interstitial fluxes. Finally,

a dislocation line model is developed to predict the role of tilt GBs in annihilating radiation damage. The model predicts the role of tilt GBs in annihilating defects depends on the rate of defects segregation to and diffusion along tilt GBs. Tilt GBs mainly serve as diffusion channel for defects to reach other sinks when defect diffusivity is high at boundaries. When defect diffusivity is low, most of the defects segregated to tilt GBs are annihilated by dislocation climb.

Up-to-date, the response of twist GBs under irradiation has been rarely reported in literature and is still unclear. It is important to develop atom scale insight on this question in order to predict twist GBs' sink strength for a better understanding of radiation response of polycrystalline materials. By using a combination of molecular dynamics and grand canonical Monte Carlo, here I demonstrate the defect kinetics in {001} and {111} twist GBs and the microstructural evolution of these GBs under defect fluxes in SiC. I found because of the deep potential wells for interstitials at dislocation intersections within the interface, the mobility of defects on dislocation grid in twist GBs is low. The retard defect diffusion along twist GBs can lead to defect accumulation at GBs in many cases. Furthermore, I found that in order to absorb accumulated interstitials at the interface, both types of twist GBs have to form mixed dislocations with edge components. The formation of mixed dislocation is either by interstitial loop nucleation or by dislocation reactions. The continuous formation and climb of these mixed dislocations make twist GBs unsaturatable sinks to radiation induced defects.

Table of Contents

List of Publications & Presentations

Publications

1. **Jiang H.,** and Szlufarska I., "Atomic insight on small angle twist grain boundaries as defect sinks in SiC under irradiation", *in preparation*

2. Wang X., **Jiang H.**, Liu C., Idrobo J.-C., Morgan D., Voyles P., Szlufarska I,, "Radiation-induced compositional evolution of grain boundaries in 3C-SiC", *Submitted*

3. **Jiang H.**, Stewart D., "Using dopants to tune oxygen vacancy formation in transition metal oxide resistive memory", ***ACS Appl. Mater. Interfaces*** 9 (19) 16296-16304 (2017)

4. **Jiang H.**, Wang X., and Szlufarska I., "The multiple roles of small angle tilt grain boundaries in annihilating defects in SiC", ***Sci. Rep.*** 7, 42358 (2017)

5. **Jiang H.**, Stewart D., "Enhanced oxygen vacancy diffusion in Ta_2O_5 resistive memory due to infinitely adaptive oxide crystal structure ", ***J. Appl. Phys.*** 119, 134502 (2016)

6. **Jiang H.**, Li H., Voyles P., Morgan D. and Szlufarska I., "Electron radiation induced diffusion of small defect clusters in covalent materials", ***Phys. Rev. B*** 94, 024107 (2016)

7. Li H., **Jiang H.**, Zhai Y., Liu C., Szlufarska I., Tyburska-Puschel B., Sridharan K, Volyes P.,s "Atomic resolution imaging of black spot defects in ion irradiated silicon carbide" ***Microscopy and Microanalysis*** 21 (S3), 1337-1338 (2015)

8. **Jiang H.**, Jiang C., Morgan D. and Szlufarska I., "Accelerated atomistic simulation study on the stability and mobility of carbon tri-interstitial cluster in cubic SiC", ***Comp. Mater. Sci.*** 89 182-188 (2014)

Presentations

1. **Jiang H.**, Xing W., and Szlufarska I., "The multiple roles of small angle tilt grain boundaries in annihilating defects in SiC". ***Materials Research Society***, Phoenix, AZ (2017)
2. **Jiang H.**, Xing W., Voyles P., Morgan D. and Szlufarska I., "Simulation and TEM study on defect clusters and amorphization in SiC". ***The Minerals, Metals & Materials Society conference***, Orlando, FL (2015)
3. **Jiang H.**, Xing W., Voyles P., Morgan D. and Szlufarska I., "Modeling and TEM study on radiation damage in SiC". ***Transformational Technologies in Molecular Simulations***, Madison, WI (2014)

List of Figures

List of Tables

List of Abbreviations

BCC: Body centered cubic

BSD: Black spot defects

cNEB: climbing image nudged elastic band

C_C: Carbon lattice atom

C_i: Carbon interstitial

C_{Si}: Carbon antisite

DFT: Density functional theory

FCC: Face centered cubic

GGA: Generalized-gradient approximation

HCP: Hexagonal closed packing

KMC: Kinetic Monte Carlo

LDA: Local density approximation

MD: Molecular dynamics

MDI: Multiple dislocation intersection

NEB: Nudged elastic band

PAW: Projector augmented wave

PL: Photoluminescence

STEM: Scanning transmission electron microscopy

Si_C: Si antisite

Si_i: Si interstitial

Si_{Si}: Si lattice atom

TEM: Transmission electron microscopy

TRISO: Tristructural-isotropic

V_C: Carbon vacancy

V_{Si}: Si vacancy

Chapter 1 Background

1.1 Structure and polytypes of SiC

Silicon carbide (SiC) is an important non-oxide ceramic that has diverse industrial applications. It has many excellent properties such as high hardness and mechanical strength, good chemical stability, high thermal conductivity, high melting point, good oxidation and erosion resistance, etc. All of these properties make SiC a promising material for applications in abrasion, cutting, high power and high temperature electronics, and nuclear reactors.

Up-to-date more than 200 SiC polytypes have been found[1]. A list of the most common polytypes include 3C, 2H, 4H, 6H, 9R, 5R, etc., where (C), (H), and (R) are the three basic cubic, hexagonal and rhombohedral crystallographic categories, respectively. In the cubic zinc-blend structure, labelled as 3C-SiC or β-SiC, Si and C occupy ordered sites in a diamond framework. The number 3 refers to the number of tetrahedrally bonded Si-C bilayers needed for periodicity, as shown in Figure 1-1a. In hexagonal polytype *n*H-SiC and rhombohedral polytypes *n*R-SiC, generally referred to as α-SiC, Si-C bilayers stack in the primitive unit cell. Examples of the stacking sequence of *n*H samples are shown in Figure 1-1b and 1-1c. The difference in stacking sequence of tetrahedrally bonded Si-C bilayers in various polytypes lead to different properties, especially in electronic properties. For instance, the band gap varies with the polytype from 2.3 eV for 3C-SiC to over 3.0 eV for 6H-SiC to 3.2 eV for 4H-SiC. Among these polytypes, 6H-SiC and 4H-SiC are the only SiC polytypes commercially available in bulk wafer form[2], and that is one reason why the vast electronic industry has been interested in these two polytypes. Poly-crystalline 3C-SiC can be easily fabricated in bulk form by sintering, chemical vapor deposition,

physical vapor deposition[2]. The ability to deposit 3C-SiC in various geometries makes 3C-SiC widely used for components in nuclear reactors.

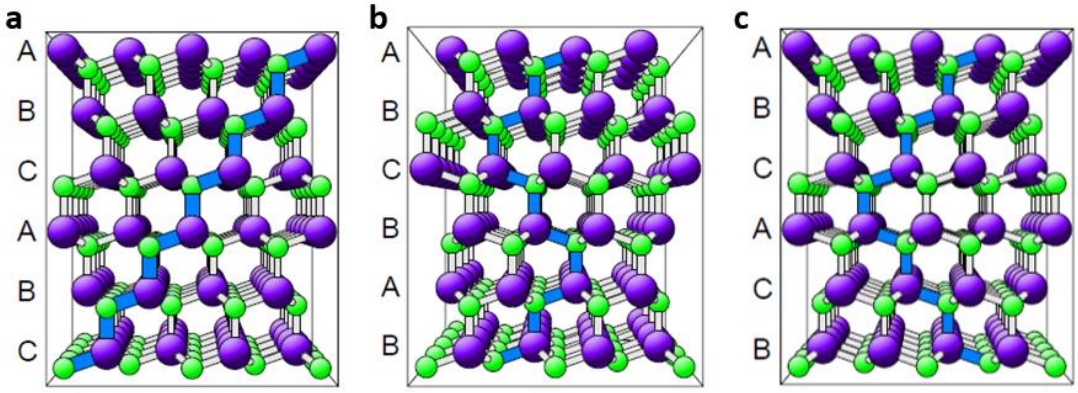

Figure 1-1 | Stacking sequence of Si-C bilayers in **a**, 3C-SiC; **b**, 4H-SiC; and **c**, 6H-Sic.

Here I will focus on the applications of 3C-SiC in nuclear reactors[3-4]. The applications of SiC as structural component in advanced nuclear reactors[5-7], as the buffer layer in advanced nuclear fuel design[8-10], and as immobilizer of nuclear waste[11-12] will be reviewed.

1.2 Application of SiC in nuclear reactor system

SiC is considered as the cladding materials in fuel rods used in light water reactor and other advanced reactor design[5-6]. SiC/SiC composite composed of 3C-SiC-based fibers reinforcing the 3C-SiC matrix is proposed to replace the traditional zirconium alloys for the reasons explained below. The composite form is designed to provide improved strength and fracture toughness as compared to the brittle non-composite form.

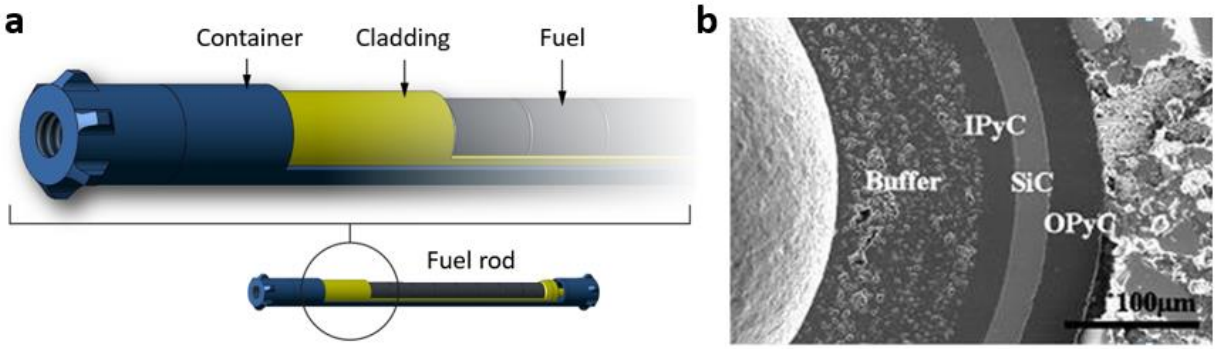

Figure 1-2 | Applications of SiC in nuclear reactors. **a**, Schematic drawing of fuel rod and components insides the rod, reproduced from Ref.[13]; **b**, Structure of tristructural-isotropic (TRISO) fuel[14].

Cladding is the outer layer of fuel rods, separating the coolant and fuel materials (e.g., uranium oxide), as shown in Figure 1-2a. The fission reaction of uranium atoms produces radioactive fragments that emit neutrons, γ rays, α and β partials and can be harmful to human health and natural environments. Therefore fuel cladding is the reactor's primary safety barrier to prevent the fission fragments from escaping the fuel into the coolant. Cladding materials in reactors are exposed to exceptionally aggressive environment due to the combination of intense radiation damage, corrosive coolant, and high temperature and pressure. All these environmental factors can cause the degradation of cladding materials properties or even failure. Zirconium

alloys have been used as cladding materials for nuclear fuel for decades[15-16]. However, zirconium alloys undergo significant reaction with reactor coolant leading to materials loss, growth of a low-thermal-conductivity oxide phase on the cladding surface, hydrating of the cladding interior, and related loss of materials ductility under normal operating conditions[15]. Under the loss of coolant accident (LOCA) conditions, zirconium alloys can undergo phase transition, loss of strength, exothermic reaction with steam, and associated hydrogen production[16]. It is accepted that SiC will react more slowly than zirconium based alloys with steam under LOCA. SiC has demonstrated exceptionally low oxidation rates up to 1700°C and has been shown to withstand temperatures exceeding 2500°C (SiC does not melt and has a very high sublimation temperature of ~2700°C). Currently available data on monolithic SiC samples indicates oxidation rates that are two to three orders of magnitude lower than that of zirconium based alloys[17-18]. The significantly improved corrosion resistance and thermal stability of SiC, together with the good mechanical property in composite form and low neutron capture cross section, make SiC a strong candidate in replacing zirconium alloys for improved accident tolerance in nuclear reactors.

SiC-based cladding design may hold significant potential for use in accident tolerant nuclear fuel, but there are some concerns and challenges which have to be fully addressed. It is well known that the thermal conductivity of SiC degrades rapidly due to the production of point defects created by neutron irradiation[19]. As with most ceramics, the dominant carriers of thermal energy in SiC are phonons. Defects produced by irradiation can heavily scatter phonons and therefore cause degradation in thermal conductivity. For advanced cladding designs, a reduction in thermal conductivity leads to decreased fuel thermal margin and exacerbates issues associated with creep deformation. With a goal to understand and being able to predict the degradation of

thermal conductivity, active theoretical and modeling works using density functional theory (DFT) or molecular dynamics (MD) on the effect of point defects, voids, dislocations, grain boundaries on phonon scattering are being conducted in the community[20-22]. Besides thermal conductivity degradation, the accumulation of radiation induced defects can lead to a saturatable swelling in SiC[23-24]. The combination of temperature gradient, and temperature-dependent swelling would lead to approximately 0.05% elastic strain within the cladding wall[3]. Though this may be mitigated by enhanced creep under irradiation, only limited data is available for irradiation creep behavior of SiC to make any predictions. This magnitude of swelling needs to be properly taken care of to avoid microcracking or lowered fatigue strength. Another concern is that the corrosion of SiC along interfaces. In a recent study on corrosion of SiC in 360°C supercritical water[18], grain boundaries of SiC are found to be dissolved preferentially during the early state of corrosion. Grains became thinner and detached from the surface, thereby leading to accelerated weigh loss. Though this phenomenon was found in supercritical water, a very aggressive coolant, it does alert people to consider the corrosion of poly-crystalline SiC along interfaces and to carefully exam the corrosion of SiC in other coolant systems such as liquid sodium cooled or gas cooled reactors.

SiC has also been proposed to be used as the buffer layer in advanced nuclear fuel designs[8-10] to prevent the releasing of fission produces (e.g., Xe, I, Cs) from fuel particles. This is one of the main functions of the SiC layer in a recently proposed fuel design, tri-structural isotropic (TRISO) coated fuel[8-10]. In TRISO fuel, fuel particles are triple-coated spherical particles of uranium fuel (e.g., UO_2, UC, UCO), less than one millimeter in diameter. A uranium center is coated by a layer of carbon, which is then coated by silicon carbide, with an outer shell of carbon, as shown in Figure 1-2b. The particles are then embedded in graphite or SiC matrix to be

fabricated into fuel pellets. Depending on the design of reactors, these pellets can be assembled into different geometries and then be used in these reactors. As introduced earlier, fission can produces radioactive fragments that emit neutrons, γ rays, α and β partials which are harmful to human health and natural environments. It is of great importance to prevent the release of these fragments into coolants. It has been found that even at 1800°C (more than 200°C greater than postulated accident conditions) most fission products remained inside the TRISO fuel particles. The advantage of TRISO fuel comes from many factors. One factor is the multi-coating design to capsulate the fuel, which in effect, gives each tiny particle its own primary containment system. Another important factor comes from the slow diffusivity of fission products in SiC, as has been confirmed in recent ion implantation studies of fission products in SiC[25-26]. In the case of ion-implantation of Cs and I in SiC, measurable diffusion is not observed until temperatures exceed 1400 K.

Although the layer of SiC effectively retains most fission products under the operating and accident conditions, there have been some observations of an undesirable release of metallic fission product, in particular of radioactive silver[27-28]. The diffusion of implanted Ag in SiC has also been reported in literature at high temperature. In Ref.[27], Ag grain boundary diffusion becomes measurable above 1375 K, while bulk diffusion is not evident until temperatures exceed 1675 K. Such release of Ag could results in Ag deposition within the reactor and thus raises concerns about the reactor's safety, creates maintenance issues, and contributes to restriction on higher operating temperature fuel efficiency. Many studies have been done to understand the release mechanism of Ag through the SiC layer[27, 29-31]. A number of experimental and atomic simulation studies have provided strong evidence supporting the hypothesis that GB diffusion is a dominant pathway for Ag transport in CVD-SiC[31-33]. Besides thermal diffusion, defects such

as point defects and defect complexes may active different diffusion mechanisms of Ag in SiC. Further quantifying the radiation enhanced diffusion and combining it with GB diffusion to model Ag release is very challenging. With all the promising performance in holding majority of fission products and concerns on releasing of some metallic products, both experimental and simulation studies are being conducted worldwide to improve the TRISO fuel design and development for better reactor safety.

The ability of SiC to remain chemically inert and retain fission products, as discussed above, together with its superior mechanical strength, high thermal conductivity, and low thermal expansion, also makes it a promising materials to immobilize nuclear waste[32-34]. Some of the earliest considerations for the use of SiC to coat nuclear waste for fission products immobilization date back to the early 1980s[32-33], and more recently SiC has been proposed for the immobilization of ^{14}C, ^{129}I and ^{85}Kr from the reprocessing of nuclear fuel[34]. The usage of silicon carbide as an inert matrix for the burning or transmutation of long-lived fission products could result in direct disposal of the inert matrix in a geologic repository. Highly burned up TRISO fuel where SiC is the primary barrier to fission product release can also be placed directly in a geologic repository. When SiC is utilized as a coating or monolithic host for the immobilization of fission products, it will only be exposed to beta and gamma radiation from the beta decay of the fission products. Because energetic electrons and beta particles produce only Frenkel pairs at low rate[35], significant irradiation-induced microstructural changes are not expected in SiC as immobilizer of nuclear water under geologic repository environments.

SiC has also been proposed for applications as structural components in nuclear reactors, such as control rod in high temperature gas reactors[3], core structural components in liquid salt-cooled advanced high temperature reactors[36] and gas cooled fast reactors[37]. Beside in advanced

fission reactor design, due to its inherent high-temperature capability and low induced radioactivity, SiC is being considered as a key materials in the development of fusion energy[3, 38-39]. The low radioactivity of SiC, together with the nature of fusion that no long-term radioactive waste is produced, makes it much easier to deal with fission waste proposal. Potential applications of SiC in fusion reactors include the first wall facing plasma, the diverter that intercepts edge plasma, and the blanket that breeds tritium fuel.

1.3 Radiation effects in SiC

The radiation environments in reactors can induce many changes in SiC including degradation of thermal conductivity[19], volume swelling[23-24], creep[23-24], reduction in corrosion resistance[18], and induced radioactivity[40]. A good understanding of radiation effects in SiC on various properties of this material is of critical importance for component design and safety evaluation. In this section, a review on this topic is presented. Energetic particles emitted from nuclear fuels including neutrons, ions and electrons can cause various effects in materials including transmutation, excitation or atom displacements. The effect of transmutation and excitation will be first reviewed in the following two paragraphs, followed by a detailed review on radiation induced atom displacement, change of microstructural and material properties due to long term evolution lattice defects.

1.3.1 Transmutation

Nuclear transmutation is the conversion of one chemical element or an isotope into another. In SiC in nuclear reactor environments, transmutation can happen by the incident of high energy neutrons into C or Si atoms. The transmutation products from C atoms include both gaseous H, He and metallic Li, Be, B. The transmutation products from Si atoms include My, Al, and P[40-41]. The amount of transmutation is insignificant compared to the number of atom displacement in fission reactors. For instance, modeling estimates the ratio of the amount of transmutation products in atom part per million (appm) to the amount of atom displacements (dpa) is blow 10 appm/dpa in Modular Pebble Bed Reactor or High Frequency Isotropic Reactor[40]. While in fusion reactor, due to the sharp energy peak at the high energy range in neutron spectrum, transmutation is expected to be more severe.

Transmutation can modify different materials properties relevant for the applications. One most straightforward impact is the change in electric conductivity[40, 42]. SiC is a stoichiometry high bandgap semiconductor, and it is insulating at low temperatures. Electrical conductivity of SiC is usually determined by the concentration of impurities. N is the common primary impurities in CVD SiC matrix, so SiC/SiC composite is often considered electronically an n-type semiconductor. At the moment atomic displacement effect being ignored, the transmutation in fusion environment is anticipated to compensate and eventually over-compensate the initially n-type SiC. In such a case, the evolution of electrical conductivity at a given temperature could be very drastic during the semiconductor type transition. There are numerous reports on very significant effects of small amount of impurity doping on electronic properties of SiC[43]. Electrical properties of SiC are altered not only by nuclear transmutation but also by the Frenkel defects produced by atomic displacement. While experiments do indicate that all of carrier density, mobility, and electronic level in polycrystalline 3C–SiC are significantly modified after irradiation, the combined effects of transmutation and lattice defect productions on electrical conductivity of SiC make it very challenging to distinguish contributions from either source and make predictions. Another major impact of transmutation on SiC properties is the change of corrosion resistance, which is of critical importance for SiC's role as cladding materials. The outstanding oxidation resistance of SiC is enabled by presence of silica scale formation on its surface. It is known that Al in silica scale can promote corrosion of SiC in the passive oxidation regime by enabling transport of oxygen[44]. Besides, Mg is known to react with silica producing Mg_2Si and MgO, which can potentially alter oxidation behavior of SiC. However, limited data and analysis on the change of SiC corrosion resistant solely due to transmutation is available. Recent investigations show that transmutation products, especially the H and He, may interact

with intrinsic defects such as vacancies and interstitials in SiC. In a recent study on radiation induced creep of SiC, it was found the growth of interstitial clusters was inhibited by implantation of He into SiC[45]. Though the implantation process cannot accurate produce the He distribution in SiC in real reactors, it does suggest the transmuted products can play a role in the long term microstructural evolution of SiC.

Transmutation can make materials radioactive, and the induced radioactivity can pose challenges in nuclear waste disposal. However, the radiation induced radioactivity is generally extremely low for SiC irradiated in any neutron environment. The radioactivity in radioactive SiC is due primarily to ^{32}P[40-41], which is a beta emitter and has a half decay period of 14.29 days. The gamma dose rate of neutron irradiated SiC decreases quickly in post-irradiation period due to the short lived ^{32}P. Long-term radioactivity comes from the slow decay of ^{14}C and ^{26}Al, which are low in concentration and pose little threats to local environments in nuclear waste disposal.

1.3.2 Excitation

Excitation happens when the incident particle interacts with surrounding electrons near atom nuclei and cause the excitation of the electrons from lower energy state to higher energy state, or cause the ejection of the electrons. Excitation usually happens in electron and ion irradiation because the Coulomb interactions between incident particles and electrons. In fact, for high energy ion irradiation, a comparable or even majority of energy is dissipated through ion-electron interaction compared to atom displacement (detailed in Section 1.3.3). Since neutron does not carry any charge, there is little chance of excitation caused by neutron as it travels through the lattice. If core electrons were ejected, the refilling of the core orbital by electrons from higher orbitals can cause the emission of characteristic X-rays. The ejection of electrons can also lead the atom to become charged and a charged defect usually shows different structure

as well as kinetic properties from neutral ones. It has been shown by DFT calculations that in SiC the stable point defect structure, formation energies and diffusion of barriers differs from those of neutral point defects[46]. For instance, the diffusion barrier of C interstitial can raise from 0.5 eV in neutral state to 1.7 eV in +2 charged state. While the most stable charge state of defects is usually determined by the Fermi level of the materials which is set by doping level and external bias potential, the radiation induced charged state of defect is rather temporary.

In the high-energy ion irradiation (such as 870 MeV Pb ions with an electronic energy loss of 33 keV/nm in SiC), the ion energy is mainly deposited to the loosely bound electrons and then, through electron–phonon coupling, transferred into atomic motion (local heating). In recent studies[47], it has been shown the excitation induced local heating effect can drive local structural evolution in SiC, such as annealing pre-existing lattice damages and induce order-disordered transformation. In these studies, 900 keV Si^+ ion irradiated SiC samples were post-irradiated by high energy ions including 4.5 MeV C, 6.5 MeV O, 21 MeV Si or 21 MeV Ni with various fluxes. Scanning transmission electron microscopy (STEM) analysis of the top surface regions where most energy of those MeV ions is dissipated by excitation shows the relative disorder in these regions, which was caused by the Si ion pre-irradiation, is reduced by the post radiation of these high energy ions. As the dose of high energy ions increases, the relative disorder of the pre-damaged regions decreases. The hypothesis that excitation induced local heating can anneal existing damages in SiC was further supported by MD simulations of a pre-damaged SiC supercell using thermal spike model. Given the high amount of charged particles emission in fission reactors, such as electron, H^+, and He^{2+}, this study suggests that excitation induced annealing may extend the performance lifetime of SiC in fusion reactor environments.

1.3.3 Atom displacements

Atom displacements can happen when the incident particle transfers an energy to the atom higher than a displacement threshold energy by elastic collision. The threshold energy is defined as the minimum energy to displace an atom from its lattice site to a neighboring interstitial site. It depends on the crystal orientation of the displacement event. The reported displacement threshold energy can be obtained by MD simulations, and it is approximately 20 eV for C, and 40 eV for Si in SiC[48]. The atom displacement event happens in the following sequence. First, the transfer of kinetic energy (higher than the displacement threshold) to the lattice atom gives rise to a primary knock on atom (PKA). This displaces PKA from its lattice site and enables it to travel in the lattice along certain direction. As the PKA travels, it can interact with other atoms either by elastic collision, which can cause atom displacements if the energy is higher than displacement threshold energy, or by inelastic interaction that causes excitation, ionization, and emission of X-rays. Such interactions will continue until the PKA gradually loses its kinetic energy and rest in the lattice. The continuous displacement of atoms along the trajectory of PKA is referred as displacement cascade. In some cases, the energy of PKA is not high enough to displace other atoms and the PKA rests in a neighboring interstitial site, producing a vacancy and an interstitial which are usually referred as a Frenkel pair. This situation usually occurs during light ion and electron radiation when low energy is transferred to atom. During irradiation with high energy neutrons and heavy ions, displacement cascade can usually happen. It should be noted that displacement cascade happens on the timescale of 10^{-11} s. This short timescale can be covered by MD simulations, and a review on MD simulation of displacement cascade in SiC is shown in the following paragraph.

In displacement cascades, many atoms are displaced from their lattice sites. The term "displacement per atom (dpa)" is defined to quantify and normalize the magnitude of atom displacements. It is defined as the average number of times that an atom is displaced in the materials for a given radiation dose. The concept of dpa makes it convenient to compare the degree of atom displacements in different materials under various radiation conditions. DPA can be calculated by statistics of MD simulation of cascades or analytical model such as the Kinchin and Pease model, as detailed in Ref.[49]. However, the number of stable lattice defects produced in a cascade is usually smaller than the number of displacements. This is because some displaced atoms may hop back to the lattice site by thermal vibration in the cascade timescale, thus the number of defects survived after the cascade is smaller. Different defects can be generated by atom displacement, including both point defects and small defect clusters. So far, extensive MD simulations have been conducted to investigate the production of lattice defects in displacement cascades in SiC. For example, Devanathan *et al*.[50] and Gao *et al*.[51] used MD to simulate the displacement cascade caused by 8 energies selected from 0.25 keV to 50 keV in SiC. Point defect including C and Si vacancies, C and Si interstitials, C and Si antisite, small, and small vacancy clusters such as Di-vacancies and Tri-vacancies clusters were reported. In a recent modeling work of interstitial clusters in SiC[52], the generation of small interstitial clusters in displacement cascades was suggested in order to correctly reproduce experimental measured interstitial cluster concentration. The reason that these interstitial clusters were not reported in previous MD simulation works is attributed to the small cut off distance to identify interstitial clusters used in result analysis. Recent DFT based studies on structures of small interstitial clusters in SiC suggests that a cut off radius of 2nd nearest neighbor is necessary to capture interstitial clusters. To fill the gap of no data reported on small interstitial formation in cascade in

SiC, Liu *et al.*[53] conducted MD simulation of cascade with many PKA energies and directions, and they found a significant amount of small interstitial cluster formation in cascade by using the updated criterion. The above works have been done in single crystal SiC, while in real cases when poly-crystalline SiC is utilized, the existence of grain boundaries may affect the production of defect in cascade. To clarify this, Narasimhan *et al.*[54-55] conducted cascade simulation in bi-crystal supercells with different kinds of grain boundaries. They found that in-grain defect production is not affected by the presence of a GB, and so is the damage in the individual domains constituting the in-grain regions.

1.3.4 Effects of radiation induced defects on SiC properties

The formation and afterward long-term evolution of these point defects and small defect clusters can significantly change material properties and performance of SiC, such as thermal and electric conductivity, swelling, creep, etc. In the following paragraphs, effects of lattice defect formation and diffusion on these properties will be reviewed with an emphasis on the importance to fully understand the radiation induced defects.

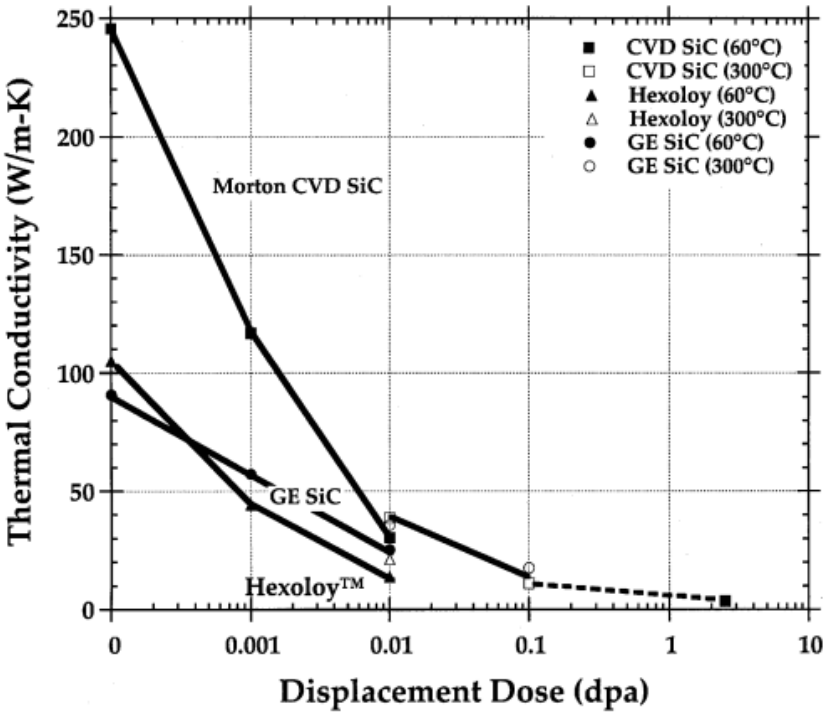

Figure 1-3 | Change in thermal conductivity of irradiated SiC as a function of radiation dose. Adapted from Ref.[19].

One of the most significant change of properties in irradiated SiC is thermal conductivity as shown in Figure 1-3[19]. This is a critical parameter considered for cladding materials in fission reactors and the first wall in fusion reactors, and it determines the magnitude of thermal stress. For advanced cladding designs, a reduction in thermal conductivity can also leads to decreased fuel thermal margin and exacerbates issues associated with creep deformation. The reduction in thermal conductivity in irradiated SiC is because the dominant carriers of thermal energy in SiC are phonons, same as most ceramics, and radiation induced defects can heavily scatter phonons[21]. For example, by using MD simulations and theory modeling, Li *et al.*[20] showed that a single defect (a vacancy, an antisite, or an interstitial) in a cell of 216 atoms, which corresponds to defect density of 0.5%, can reduce thermal conductivity by as large as an order of magnitude. Not only point defects can reduce thermal conductivity, defect clusters and dislocation loops

formed by the aggregation of point defects can also significantly change thermal conductivity of SiC. In a later theoretical model[19] that considered phonon scattering in SiC from point defects, clusters, and dislocation loops, it is shown that for weak defect scattering (e.g., from point defects and dislocation loops) thermal resistance (the reciprocal of thermal conductance) of defects is proportional to the defect concentration. In the case of strong defect scattering events (e.g., from voids), thermal resistance is predicted to scale with the square root of the defect concentration. The predictions of the model showed a very good agreement with experimental data for a number of ceramics (including SiC) reported in the same paper. This theoretical prediction was further supported by MD simulation[19] which reported a linear relationship between the thermal resistances on concentration of point defects in SiC.

Similarly to thermal conductivity, electrical conductivity of SiC is also found to change significantly due to the formation of lattice defects[56]. Change in electrical conductivity of SiC is a concern for its application as the 1st wall in fusion reactors where SiC is used as an insulating layer directly exposed to plasma. Besides, electrical conductivity is also of critical importance for applications of SiC in power electronic devices[57-58]. Since dopants such as Al or P diffuse at a slow rate in SiC, doping is usually done by ion implantation with ion energy at the range of tens to hundreds of keV[59]. Though this energy range is lower compared to the MeV range in nuclear reactors, these energetic ions can also displace atoms and produce defects such as Frenkel pairs. These defects are usually annihilated by annealing the ion implanted SiC wafer in thermal annealing to activate interstitial vacancy mutual recombination. As these point defects become diffusive in thermal annealing, they can also form clusters that are found to be heat-resistant up to 1700°C[60-62]. Lattice defects, especially carbon atom clusters, can also be introduced in the thermal oxidation of SiC to grow the insulating dielectric SiO_2 layer[63-64]. In this process, oxygen

atoms break Si-C-Si bonds to form Si-O-Si bonds to grow silica. Most C atoms can be removed by forming and releasing CO, while some C atoms stays in the lattice and diffuse to grow C interstitial clusters near the SiC/SiO_2 interface. The formation of these C interstitial clusters has been supported by DFT calculations and MD simulations of the oxidation process[65]. The point defects and defect clusters can behave as charge carriers' trap and harm the correct function of the devices. DFT calculations have shown most intrinsic point defects and defect clusters have defect energy states in the middle of the bandgap[46], which can be categorized into deep level defects. Deep level implies electron wave functions are largely localized at the defect site and thermal energy at room temperature is insufficient to release electrons (or holes) from these defects. For example, the energy states of C interstitial at neutral state in various configurations in 3C-SiC are in the range of 0.8-2.3 eV above the valence band[46]. Defect clusters identified by photoluminescence such as $Z_{1/2}$ and EH_5, which have been suspected to be C interstitial clusters, have defect level at 0.7 eV and 1.04 eV below the valence band[66], respectively. A high concentration of these deep level defects can reduce all of carrier density, mobility, and therefore degrade the performance or even cause malfunction of electronic devices.

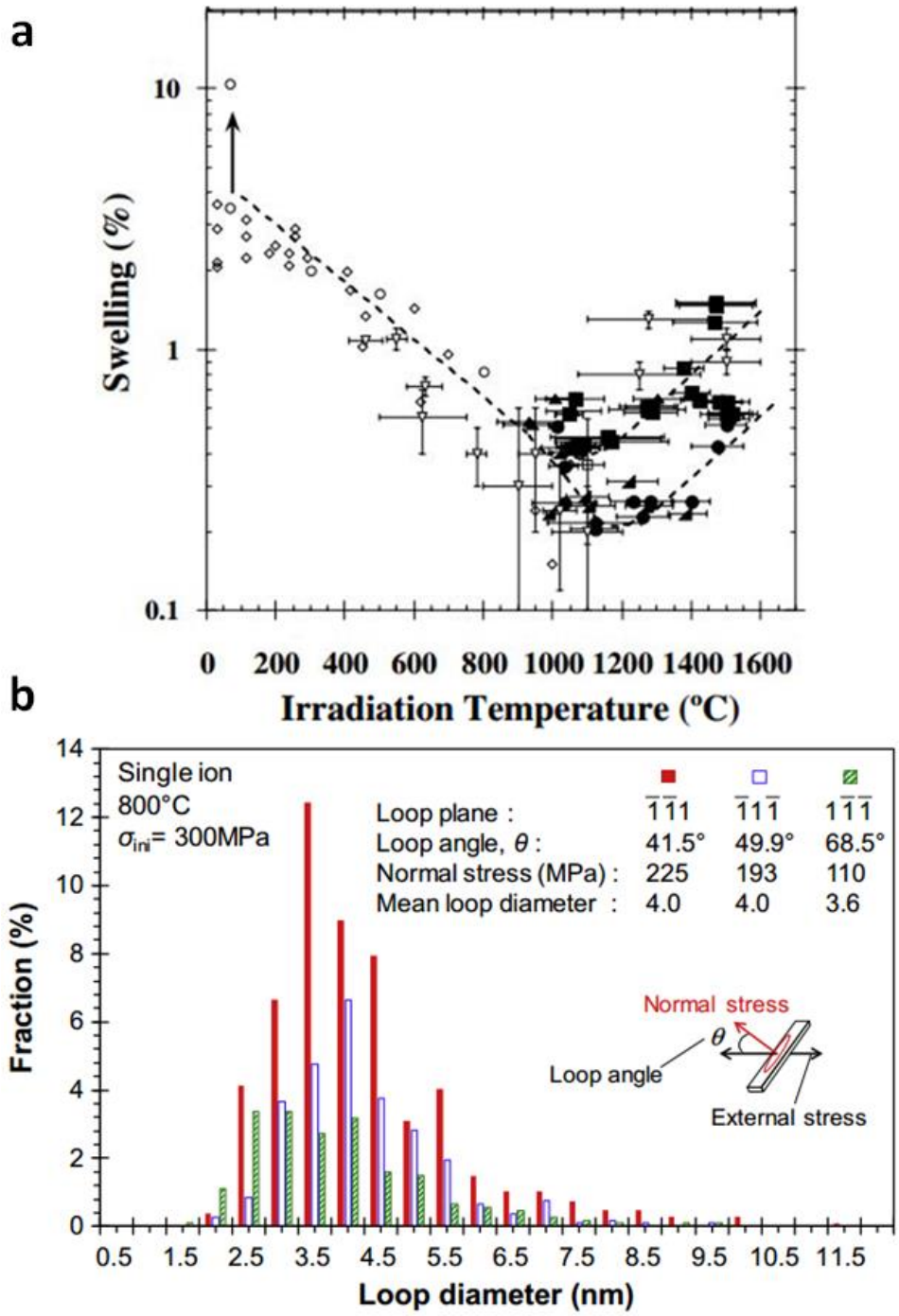

Figure 1-4 | Swelling and creep of SiC under irradiation. **a**, Swelling of irradiation SiC at different temperatures, adapted from Ref.[23]; **b**, Fractions of dislocation loops on different {111} planes in radiation induced creep of SiC, adapted from Ref. [24].

In addition to effects on thermal and charge transport properties, formation and accumulation of radiation induced defects can harm the mechanical strength and stability of SiC relevant for its applications as structural components in reactors. It is known that SiC undergoes a saturatable isotropic swelling at various temperatures after a certain dose of radiation due to the production and accumulation of lattice defects[4, 23-24]. The saturation dose is typically a few dpa. What is more important, the radiation induced saturation swelling level of SiC is found to be highly dependent on radiation temperature[23], as shown in Figure 1-4a. This is because temperature determines the kinetic of radiation induced defects, which affects the evolution of microstructure and hence the swelling. At temperature below the critical amorphization temperature (~150°C), many defects survive after the cascade due to a lack of thermal energy to perform mutual recombination, and only interstitials can diffuse at a slow rate. The accumulation of single interstitials, vacancies and small interstitial clusters distort the crystal and lattice and can finally make the materials amorphous when the defect concentration reaches a certain level. The swelling of neutron-amorphized SiC has been reported to be 10.8% for 70°C irradiation[67]. As temperature goes beyond the critical amorphization temperature and below 1000°C, this swelling regime is referred as point defect swelling of SiC. Point defect swelling is an isotropic volume expansion that is believed to occur by lattice relaxation due to accumulated isolated point defects and small point defect clusters during irradiation at temperatures where vacancies are not sufficiently mobile. As the temperature increases above the critical amorphization temperature the number of defects surviving the cascade are reduced and the mobility of both silicon and carbon interstitials becomes significant. That's why the saturation swelling level decreases with temperature in this regime. For temperature below and approaching 1000°C, microstructural studies have shown the presence of interstitial cluster and Frank loops, indicating the major

contribution to swelling from interstitial clustering. However, the contribution to swelling from observable interstitial loops (diameter in nm) is insufficient to fully account for the total swelling[68]. Recent studies have suggested that point defects and tiny interstitial clusters with diameters in sub-nm makes a lot of contributions to swelling[69]. In SiC underwent point defect swelling, a very good agreement of dimensional expansion with lattice spacing has been confirmed by X-ray diffractometry studies[70]. This supports the hypothesis that isotropic volume expansion is caused by lattice relaxation due to accumulated isolated point defects and small point defect clusters. The apparent increase in swelling in the 1000–1500°C range is likely to be induced by the formation of voids because voids are commonly seen in irradiated SiC within this temperature. The increased mobility of vacancies at high temperatures leads to vacancy clustering and growth into these voids. The saturation swelling level below 2% in SiC can lead to SiC based component swelling and stress buildup. For any component that requires dimensional stability below the swelling strain of pure SiC, design solutions will have to be sought for accommodating the swelling strain without imposing detrimental impacts on the core performances.

Radiation induced swelling and thermal swelling of SiC can lead to stress buildup inside the structural components. Besides isotropic swelling induced stress, the through-thickness temperature gradient in cladding or vessel walls can induce significant internal shear stress. While thermal creep is extremely limited in SiC even at 1000°C, radiation induced creep plays an important role to relieve the stress. Several studies have been conducted to investigate radiation induced creep in SiC[24, 45, 71]. For example, Price *et al.*[72] investigated the creep behavior of pyrolytic 3C-SiC irradiated with neutrons at 640 – 900°C using dynamic stress loading and of thin SiC strip irradiated with neutrons at 780, 950, and 1130°C using the four-point flexural

loading. While these data are valuable, but the differences in stress loading method and materials fabrication make the data less comparable. A recent systemic studies on radiation induced creep of 3C-SiC using bend stress method over a wide range of temperature between 280°C and 1200°C and a range of stress between 150 MPa and 300 MPa was conducted by Kondo *et al.*[24] This study shows that radiation induced creep can happen at temperature as low as 400°C. Starting from 400°C to 800°C, a linear relationship between irradiation creep and swelling was observed implying the common reason for creep and swelling within this point defect swelling temperature regime. TEM examination of the microstructures shows that the preferably formation of interstitial loops on certain crystal plain due to external stress is the main creep mechanism. As shown in Figure 1-4b, more dislocation loops are found in {111} planes whose normal vectors have a smaller angle (loop angle in Figure 1-4b) with the external stress direction than those planes whose normal vectors deviate from the stress direction at a larger angle. The preferentially nucleation/growth of interstitial loops implies that stress has a significant impacts on the initial nucleation process of interstitial cluster as well as the diffusion/attachment of individual interstitials to existing clusters.

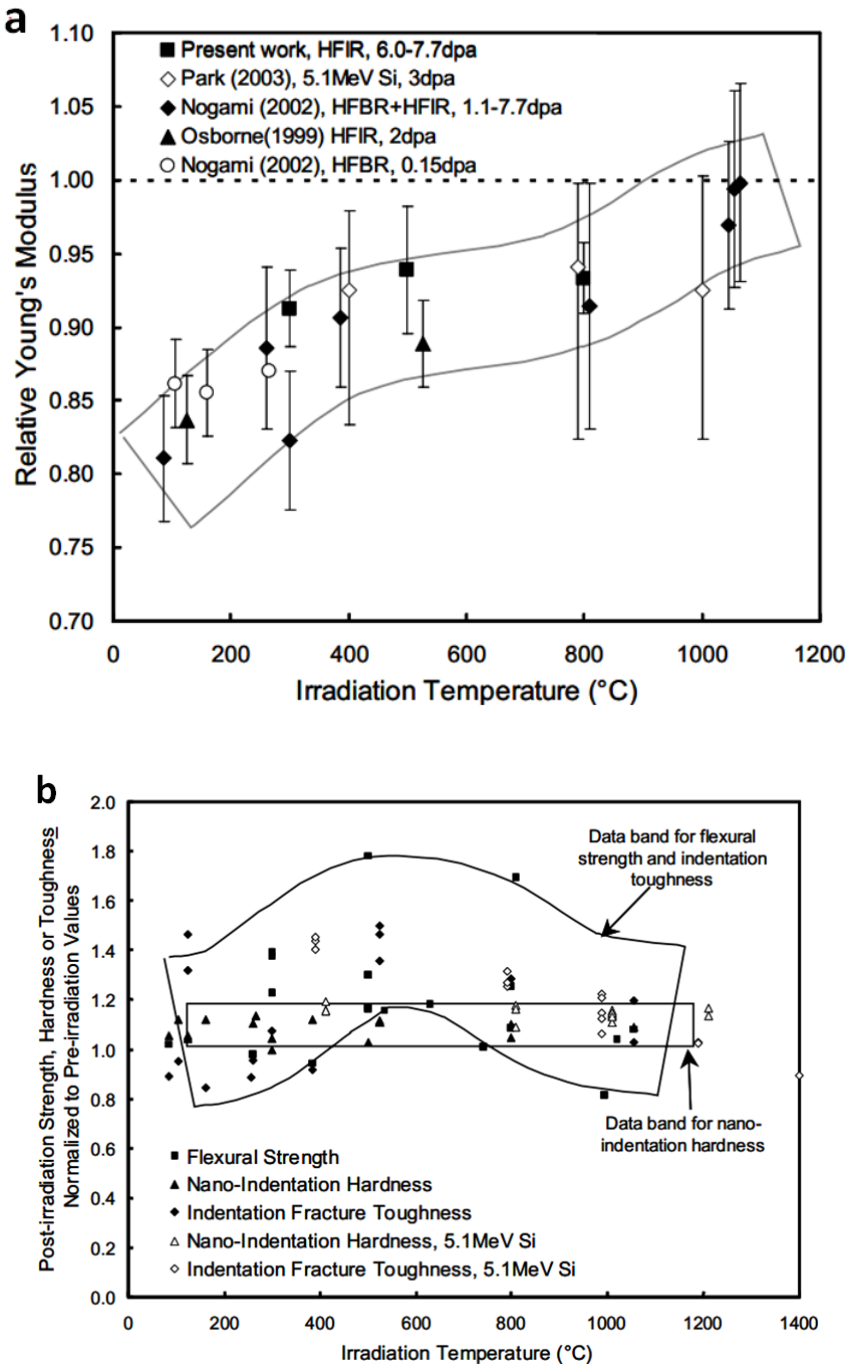

Figure 1-5 | Change in mechanical strength of irradiated SiC at different temperature. **a**, Young's modulus; **b**, Nano-indentation hardness, flexural strength and indentation toughness. Adapted from Ref.[70].

Radiation induced defects and the evolution of microstructure can make changes in mechanical properties of SiC[70]. Figure 1-5a summarizes available data on changes in Young's modulus, nano-indentation hardness, flexural strength and indentation toughness of 3C-SiC irradiated by neutron to 0.15-18.7 dpa at different temperatures. As shown in Figure 1-5a, irradiation generally reduces modulus, and the extent of reduction is more significant at a lower irradiation temperature. No obvious dependence of modulus on the fluence level was noted in this range. The modulus reduction becomes negligible when irradiation temperature reaches or exceeds ~1000°C. The strong correlation between Young's modulus and irradiation temperature below 1000°C, which is in the point defect swelling regime, implies this change is likely to be induced by formation and accumulation of isolated point defects and small defect clusters. In SiC underwent radiation induced swelling below 1000°C, a very good agreement of dimensional expansion with lattice spacing has been confirmed by X-ray diffractometry studies. Theoretical Young's modulus calculations using MD simulation with Tersoff potential show the modulus decreases with increasing interatomic distance. When the linear lattice swelling reaches 1% (corresponds to saturation swelling level at 600°C in Figure 1-5), Young's modulus is reduced by approximately 10% with respect to un-irradiation SiC. This shows good agreement with the reduction in Young's modulus at 600°C in Figure 3a. Therefore, it is likely the reduction in Young's modulus below 1000°C in irradiated SiC is because of the change in lattice constant, which is induced by the lattice relaxation to accommodate point defects and tiny defect clusters. Figure 1-5b shows the nano-indentation hardness exhibits relatively small irradiation effect that is insensitive to the irradiation temperature, and also the width of data band is small. Moreover, the individual data points within a data set exhibit a small scatter. This is contrasting to the fact that both the flexural strength and the indentation fracture toughness data indicate a broad peak

at 300-800°C with a large scatter. The peak at 300-800°C is probably due to the introduction of nano-sized defect clusters at extremely high densities. The defect cluster density decreases as the irradiation temperature exceeds ~800°C when vacancies become mobile. As irradiation temperature lowers within the point defect swelling regime, the increased lattice expansion and the resultant Young's modulus decrease should essentially reduce the fracture strength. It is speculated that the fracture strength/toughening peak at 300-800°C is thus formed.

Besides the properties reviewed above, radiation induced defects and long-term microstructural evolution may induce changes in other properties such as corrosion resistance[18], which is under investigation and unclear so far. Through this review, it is evident that the long term evolution of radiation induced defects, such as recombination, diffusion and interaction with existing microstructure are fundamental and important to understand property change. In Section 1.4, current knowledge on these radiation induced defects and their long term evolution is reviewed.

1.4 Long-term evolution of radiation induced defects

From Section 1.3.4, it is clear the changes in many properties (e.g., transport, swelling, creep, mechanical strength) in SiC under irradiation are caused by the formation of radiation induced defects and long-term microstructural evolution. Moreover, a strong correlation between the irradiation temperature and the magnitude of material property change was found. This highlights the importance of defect kinetics on the long-term microstructural evolution in SiC. As introduced in Section 1.3.3 atom displacement and shown in Figure 1-6a, lattice defects including point defects (e.g., C/Si interstitial, vacancy, and antisite) and tiny defect clusters (both interstitial and vacancy cluster) can be produced in displacement cascades. There are several fates for these radiation induced defects in the timescale beyond cascade. First of all, point defects can diffuse to react with other defects. These reactions include not only interstitial-vacancy recombination shown in Figure 1-6a, but also interstitial-antisite kick out reactions, which will be detailed in Section 1.4.1. The structure and diffusivity of point defects, as well as reaction kinetics of these processes are fundamental and important for understanding of the self-healing and microstructural evolution of irradiated SiC. In Section 1.4.1, a review on properties and reactions of point defects will be presented. Isolated point defects can diffuse and aggregate each other to grow defect clusters, as shown in Figure 1-6c. The formation of interstitial clusters have been seen in SiC irradiated over a wide range of temperature. Vacancy clusters (voids) are usually observed in irradiation over 1000°C. Current knowledge on defect cluster structure, stability, and diffusivity will be reviewed in Section 1.4.2. In addition to reacting with other radiation induced defects, these defects can also diffuse to interact with existing microstructural features in SiC, such as grain boundaries and surfaces, as shown in Figure 1-6c. These microstructural features are usually considered as sinks that can annihilate radiation induced

defects. In Section 1.4.3, a review on defect-grain boundary interaction will be presented with a focus on the evolving insights on grain boundaries as defect sinks in recent years.

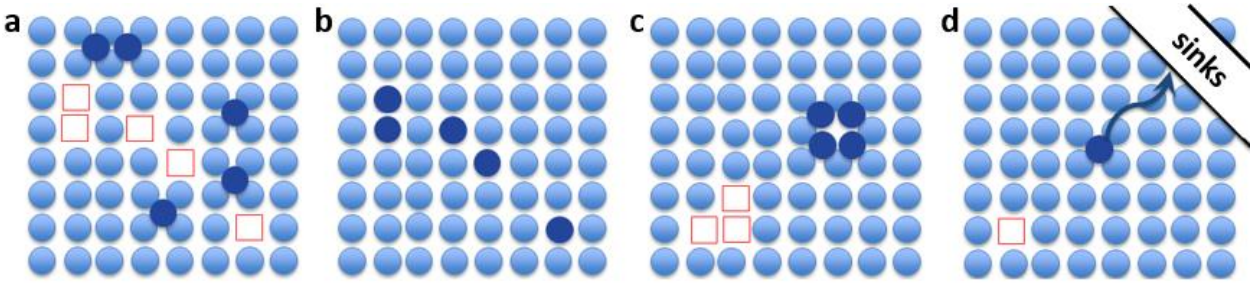

Figure 1-6 | Schematic drawing of defect evolution in SiC. **a**, defect survival from displacement cascades; **b**, interstitial-vacancy recombination; **c**, aggregation to form clusters; **d**, diffusion and annihilation at defect sinks.

1.4.1 Energy landscape of point defect diffusion and reaction

Point defects are the most fundamental type of defects in materials. In displacement cascade in SiC, a vast number of point defects including C interstitial, Si interstitial, C vacancy, Si vacancy, C antisite, and Si antisite can be produced. It is fundamentally important to know the structures, stability, motilities, and reactions of all point defects in order to understand the radiation response of SiC. Besides, these energy parameters are also important input parameters for defect evolution models such as rate theory or kinetic Monte Carolo (KMC), which are capable of simulating long-term evolution of defects in materials under irradiation.

With an interest to determine the defect levels of point defects in bandgap, several groups have performed DFT based calculations on vacancies and antisite in 4H- and 6H-SiC[73-74]. The first systematic investigation on the structure, charge state and diffusion barriers of point defects in 3C-SiC was conducted by Bockstedte *et al.*[46] In this study, the formation energies of point defects in different configurations and charge state were calculated by DFT calculations with

local-density approximation (LDA). The most stable configuration of C interstitial is C-C dumbbell along <100> ($C_{SP<100>}$), as shown in Figure 1-7a. This C-C dumbbell structure is stable over a wide range of Fermi energy, which is a function of the doping level of SiC. Another energy competitive structure of C interstitial is C-Si dumbbell along <100> direction ($C_{spSi<100>}$), which is approximately 0.4 eV higher in formation energy than that of $C_{SP<100>}$ over the entire range of Fermi energy. In fact, the minimum migration path for C interstitial diffusion is the alternative hop between neighboring $C_{SP<100>}$ and $C_{spSi<100>}$, as shown in Figure. 1-7a-c. The diffusion barrier is reported as 0.5 eV in this study. In a later study using DFT with generalized gradient approximation (GGA), this barrier is calculated as 0.67 eV[29].

The structure and diffusion path of Si interstitial is found to be sensitive to the doping level. In p-type doping conditions when the Fermi level is closer to valance band maximum, the most stable site for Si interstitial is to sit in the tetrahedral center of C sub-lattice (Si_{TC}), as shown in Figure 1-7d. The Si interstitial is literally in +4 charge state and its formation energy raises quickly as the Fermi level shifts to midgap or closer to conduction band minimum. In the n-type doping conditions, Si interstitial is more stable by forming a dumbbell with a lattice Si atom along <100> orientation ($Si_{sp<100>}$) shown in Figure 1-7d. Different migration paths were also found for Si interstitial at different doping level. In p-type doing conditions, all migration paths begin and end at the Si_{TC} sites. Two different types of migration mechanisms are found. One path is the kick-out mechanism that proceeds via the $Si_{sp<100>}$ as intermediate state, as shown in Figure 1-7d. The other path is the direct hop from one Si_{TC} sites to neighboring Si_{TSi} site and then hop to another Si_{TC} site shown in Figure 1-7e. The migration barrier for these paths is found to be 3.5 eV. For n-type doping conditions, the minimum barrier migration path is found to be a direct hop of one Si atom in the $Si_{sp<100>}$ dumbbell to a neighboring lattice Si site to form $Si_{sp<100>}$.

The migration barrier depends on the direction of the hop. If the hop is along the orientation of the dumbbell, as shown by the black arrow in Figure 1-7f, the barrier is reported as 1.40 eV with LDA and 1.48 eV with GGA[29]. If the hop is perpendicular to the orientation of the dumbbell shown by the red arrow in Figure 1-7f, the barrier is calculated as 0.83 eV with GGA. The diffusion of vacancies were also reported in this study.

Depending on the charge state, the migration barrier of C vacancy ranged between 3.5 eV and 5.2 eV[29, 46], and the barrier of Si vacancy ranged from 2.4 eV to 3.6 eV[29, 46]. It is clear that the migration barriers of interstitials are much lower compared to that of vacancies, implying active diffusion of interstitials while retard diffusion of vacancies at low temperature.

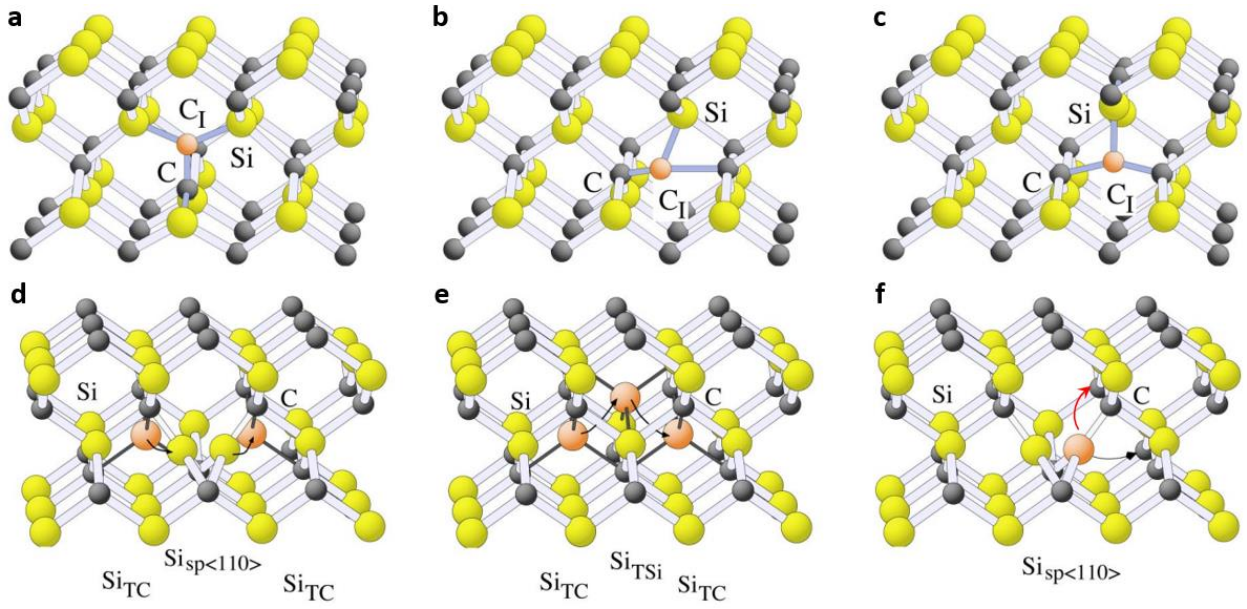

Figure 1-7 | Structures and diffusion path of interstitials in 3C-SiC. **a**, $C_{SP<100>}$; **b**, Transition state in migration; **c**, $C_{spSi<100>}$; **d**, Si_{TC} migration path 1; **e**, Si_{TC} migration path 2; and **f**, $Si_{sp<100>}$ migration path. Large yellow spheres are Si, small black spheres are C, and spheres in orange are interstitials. Adapted from Ref.[46].

Table 1-1 | Reaction barriers for 4 point defect reactions in the optimum charge state in 3C-SiC obtained from Ref.[75].

Reactions	Reaction barrier (eV)	Diffusion barrier (eV)	Limited by
$C_i+V_C \rightarrow C_C$	$E_r = 0.90$	0.67	Reaction
$Si_i+V_{Si} \rightarrow Si_{Si}$	$E_r = 0.03$	0.83	Diffusion
$C_i+Si_C \rightarrow C_C+Si_i$	$E_r = 1.34$, $E_{dis} = 1.67$	0.67	Reaction
$Si_i+C_{Si} \rightarrow Si_{Si}+C_i$	$E_r = 0.64$	0.83	Diffusion

Once isolated point defects are activated to diffuse at certain temperature, they can encounter and may react with each other. It is important to establish the energy landscape for point defect reactions in order to shed light on the self-healing process of defects in SiC under irradiation. If the energy barrier to react is lower than the barrier of diffusivity species involved, the reaction can be considered as limited by diffusion. If the reaction barrier is comparable or even higher than the diffusion barrier, its rate is controlled by the reaction rather than diffusion. A systematic study on four key point defect reactions listed in Table 1-1 was carried out by Zheng *et al.*[75] using DFT based MD and NEB calculations. The reaction barriers and the migration barrier of the diffusive species are shown in the Table 1-1. First of all, the recombination of carbon Frenkel pair is found to be limited by the reaction rather than diffusion of C interstitial. In contrast, the extremely low recombination barrier of Si Frenkel pair implies this process is controlled by the diffusion of Si interstitial. Interestingly, a trapping mode was found for the kick out reaction $C_i+Si_C \rightarrow C_C+Si_i$. Once a C_i and Si_C meet each other, they form a complex with a dissociation energy of 1.67 eV. This high dissociation barrier traps both defects while the reaction barrier of 1.34 eV is also high so the reaction can take a long time to happen. Therefore, the picture for this reaction is that C_i diffuse to encounter a Si_C and is trapped by the Si_C for a long time until the

kick out reaction can happen. For another kick out reaction $Si_i+C_{Si} \rightarrow Si_{Si}+C_i$, the reaction barrier is lower than the diffusion barrier of Si_i, and hence it is a diffusion controlled process.

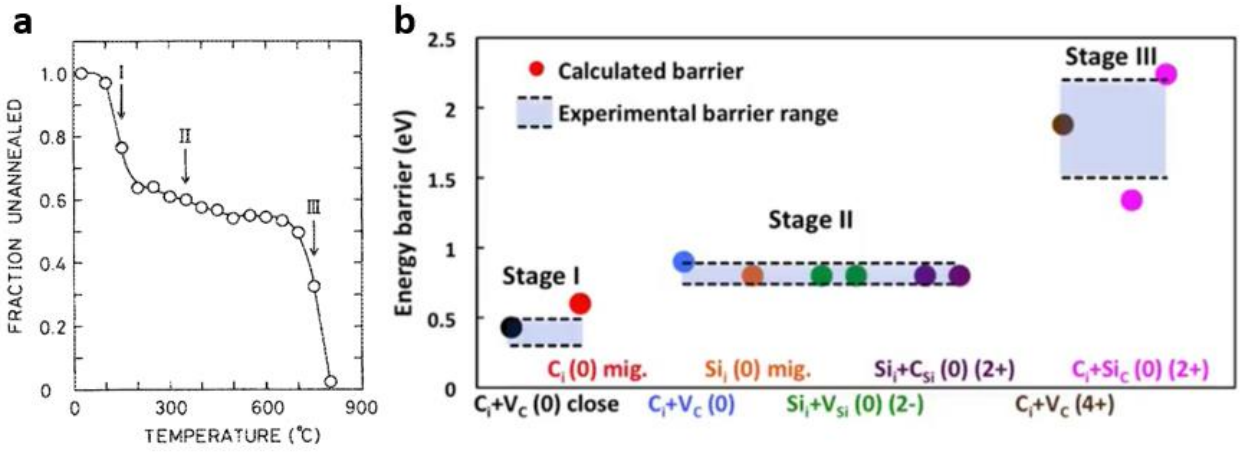

Figure 1-8 | Explanation of self-healing behavior of irradiated SiC in terms of point defect diffusion and reaction. **a**, Fractional reduction in defect density as a function of annealing temperature, adapted from Ref.[76]; **b**, Point defect diffusion and reactions activated in different annealing stages in panel **a**, adapted from Ref.[75].

The well-established studies on point defect diffusion and reactions, as reviewed above, can work together to explain the self-healing behavior of irradiated SiC at different temperatures. A thermal annealing profile of defect density in 1 MeV electron irradiated SiC is shown in Figure 1-8A. Electron irradiation usually produce Frenkel pairs due to the small amount of energy transferred to PKA[49]. Therefore, the annealing behavior of defects in this sample mainly comes from the diffusion and reaction of point defects. From Figure 1-8a, three evident annealing stages can be recognized at thermal annealing temperature of 150°C, 300-600°C, and 750°C[76]. With the knowledge of point defects diffusion and reaction barriers, these three annealing stages can be explained by defect diffusion and reactions activated at different temperatures, as shown in Figure 1-8b. For instance, at stage I, most self-healing of irradiated SiC comes from the

recombination of neutral C Frenkel pair at very close distance. At stage II, Si interstitial diffusion becomes active and enables reactions such as Si Frenkel pair recombination and Si interstitial kick out reaction with different charge states. Those high barrier reactions such as recombination of C Frenkel pair in +4 charge and C interstitial kick out reactions in neutral and +2 charged dominate the self-healing at stage III.

1.4.2 Structures and kinetics of defect clusters

Isolated point defects can diffuse to encounter and bind with each other to grow in larger size to form defect clusters. Small interstitial clusters in SiC are usually referred to black spot defects[69, 77] due to the nanoscale black spherical appearance in bright field TEM, as shown in Figure 1-9a. As tiny interstitial clusters grow in larger size by absorbing interstitials, they can form dislocation loops lying on {111} planes[24] shown in Figure 1-9b. Interstitial clusters and loops are the most common TEM observable microstructures in irradiated SiC below 1000°C because in this temperature regime interstitials are mobile but vacancies are immobile. Beyond 800-1000°C, voids start to form in irradiated SiC. Large voids[78] are tetrahedral bounded by {111} planes which appear triangular in projection on {111} plane, as shown in Figure 1-9c. Some voids are found to be in hexagonal shape in the same figure because these voids are truncated cross the corners so their projected shape is hexagonal.

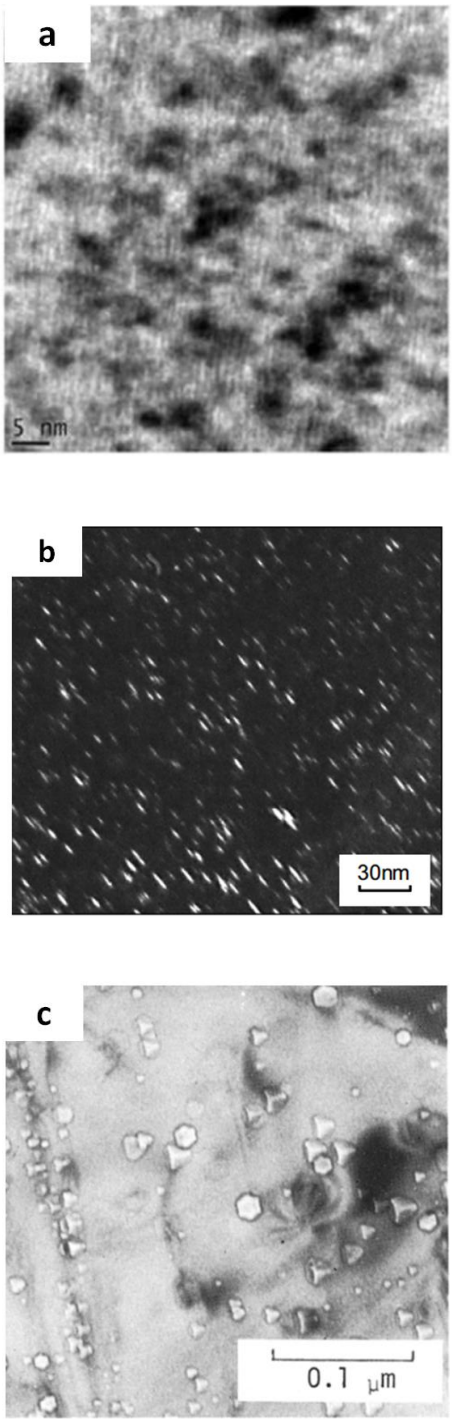

Figure 1-9 | TEM characterization of defect clusters in SiC. **a**, Black spot defect, adapted from Ref.[69]; **b**, Dislocation loops on {111} planes, adapted from Ref.[24]; **c**, Voids, adapted from REF. [78].

Defect clusters in SiC have been of great research interest in the past decades because these clusters can undermine many material properties and be resistant to common defect annealing techniques, such as thermal annealing. As introduced in Section 1.3.4, in the point defect swelling regime of SiC under irradiation, both isolated point defects and tiny interstitial clusters are believed to cause the lattice swelling of SiC. At temperatures higher than 1000°C, volume swelling is mainly caused by the formation of voids. These defect clusters can also undermine electrical properties due to their nature of deep level traps for charge carriers, as discussed in Section 1.3.4. In SiC based electronic devices, defect clusters are usually formed in the thermal annealing process after dopant implantation[60-62] and in the thermal oxidation process to grow dielectric SiO_2 on the top surface of SiC wafer[63-64]. However, it is found that some of these defect clusters are highly resistant to high temperature annealing. The photoluminescence (PL) center D_{II} is one such example[60-62]. The D_{II} center has been observed in both ion-implanted and electron-irradiated SiC samples and persists even after annealing at 1700°C. Its existence is independent of implanted species or SiC polytype, indicating that it is an intrinsic defect. Furthermore, D_{II} does not exist in irradiated SiC samples without thermal annealing, which implies it is not a direct product of displacement cascade. The annealing temperature required for the formation of the D_{II} center is around 1200°C implying that its formation is due to diffusion of defects to grow a defect complex. There are also other PL centers such as D_I, Z_1 and P-U centers[66] that have been detected in dopant implanted SiC or near SiC/SiO_2 interfaces, and are resistant to thermal annealing at different temperatures.

The existence of these deep level traps and heat resistant PL centers have stimulated active research to unveil their structures. For example, MD simulation and DFT calculations have proposed models for deep level traps near SiC/SiO_2 interface such as di-C-interstitial clusters, di-

C-antisite clusters, N_{Si} antisites and Si-C-O_x complexes[79-81]. Similar models have also been proposed for the PL centers detected in thermal annealed SiC samples[82-84]. While the information on these defect clusters are valuable, they are built to fit the signatures of traps and PL centers (energy levels and vibration spectrum) and only specific small cluster models are investigated. The lack of a systematic study on clusters as a function of size limited people's understanding of defect cluster evolution in irradiated SiC for nuclear applications where clusters can grow from small sizes to as large as loops in nm and μm scale.

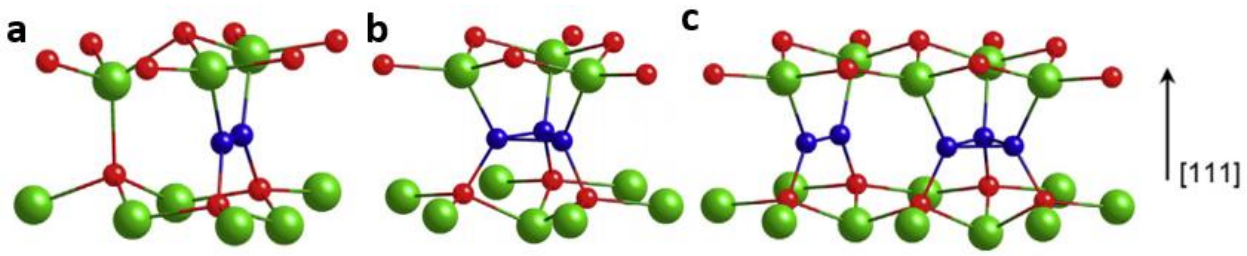

Figure 1-10 | Ground state structures of carbon interstitial clusters in SiC. **a**, di-interstitial cluster; **b**, tri-interstitial clusters; and **c**, penta-interstitial cluster. Large blue spheres are Si, small red spheres are C, and small blue spheres are interstitial atoms. Adapted from Ref.[52].

Only in recent years, due to the development of atomic simulation techniques to explore cluster configurations and advancement in fast DFT calculations, more and more studies on the structure of defect clusters with different sizes were carried out. A systematic investigation of defect cluster structure and stability as a function of cluster size was conducted by Jiang *et al.*[52] in 2014. In this study, Monte Carlo basin-hopping simulations with both empirical potential and DFT calculations were employed to search for ground state (GS) configurations of small carbon interstitials clusters with sizes up to 6 interstitials. Many previously unknown GS configurations and many energetically highly competitive metastable structures were identified. One surprising finding of this study is that the GS structures of larger carbon interstitials clusters (e.g., 5 or 6)

are disjointed and composed of di-interstitial clusters and tri-interstitial clusters lying in {111} planes shown in Figure 1-10a-c. This suggests a mechanism to grow extended {111} planar interstitial loops from tiny interstitial clusters in irradiated 3C-SiC. This study also investigated the structure of small carbon antisite based defects and found interstitial clusters can be trapped by carbon antisite to form very stable complexes.

Later on, Ko *et al.*[85] employed a genetic algorithm with both empirical potential and DFT calculations to explore the ground state of interstitial clusters with sizes up to 30 in 3C-SiC. The thermodynamic stability of clusters was investigated in terms of cluster composition (C-only, Si-only, and stoichiometric) and shape (spherical and planar) as a function of cluster size. Interestingly, they found clustering of Si interstitials is weak. In DFT calculation of Si-only clusters with size up to 4, the GS structures involves Si antisite bonded with Si interstitials. In empirical potential calculations of Si-only clusters with size up to 30, Si interstitials are found to sit in neighboring tetrahedral center sites with no direct bonds among them. The dissociation energy of Si-only cluster is also reported to be low compared to C-only or C-Si mixed clusters. According to the dissociation energy of clusters, this study suggests that clusters are predominantly C-only clusters with sizes smaller than 10 interstitials, and become stoichiometric as size increases. Furthermore, an evolution of the shape of the most stable clusters were demonstrated. Small clusters are stable in more spherical geometries while larger clusters are stable in more planar configurations. This study significantly advances our understanding of composition and geometry evolution of clusters in SiC under irradiation, especially in the nucleation stage with small cluster sizes,

Clusters with larger sizes up to ~300 have been investigated by Watanabe *et al*.[86] using MD with empirical potential. Clusters in such large sizes are actually interstitial loops. Three

different compositions including C-only, Si-only, and C-Si stoichiometric loops were explored. The formation energies of these loops were approximated as the energy of SF plus the energy of dislocations circling the SF. Energy signatures such as formation energy and dissociation energy of clusters investigated in these three studies are very helpful for models such as cluster dynamics to investigate cluster growth in SiC.

Up to this point, the mobility and dynamics of defect clusters in SiC have not been investigated. Quantification of cluster dynamics is, however, important for understanding of processes that control high-temperature annealing of defects introduced during ion implantation and thermal oxidation, and for predicting radiation response of SiC (e.g., swelling and thermal conductivity) under given temperature and irradiation conditions. For example, if small defect clusters can diffuse over a wide range temperature, one need to include processes such as cluster coalescence or cluster diffusion to sinks in models to correctly predict cluster size and density under irradiation. In addition to migration of the clusters, cluster rotation is also of potential interest. Recent studies of irradiation creep of SiC suggested that anisotropic distribution of small dislocation loops on {111} planes under applied stress is responsible for the experimentally observed irradiation creep. These loops were hypothesized to be formed by self-interstitial clusters, and their formation and rotation behavior under stress is responsible for the anisotropic distribution. A major challenge in predicting dynamics of defect clusters in SiC lies in the high defect migration barriers in this material and in short simulation time scales of standard molecular dynamics (MD) simulations. To address this, one have to use accelerated atomic simulation techniques, such as hyperdynamics, parallel replica dynamics or adaptive KMC models, which will be detailed in the Chapter 2.

Besides thermal diffusion, radiation induced diffusion of point defects and defect clusters have been reported in literature. Radiation induced diffusion is the diffusion process when the motion of objects is driven by the radiation species, such as ions, neutrons, or electrons. The phenomenon of radiation induced diffusion of point defects has been reported in lead as early as 1970s[87]. The Lead samples were irradiated at temperature as low as 50K when no vacancy diffusion and hence no void formation is expected. However, when the sample was exposed to electron beams in electron microscopy, voids were observed. The formation of voids was explained by vacancy diffusion driven by elastic collision between atoms around vacancies and incident electrons in electron microscopy. As the advancement of electron microscopy, direct observations of point defect diffusion driven by electron beam were reported in mono-layer graphene in recent years[88-90]. Besides point defects, small catalyze clusters (e.g., platinum cluster[91]) was found to diffuse on the surface of substrates under the influence of electron beams. So far, radiation induced diffusion of intrinsic defect clusters in bulk have not been observed. Given the radiation environment in nuclear reactors, it is of great interest to explore whether radiation induced diffusion can happen for clusters within SiC. If radiation induced diffusivity of clusters in SiC is high enough to drive cluster coalescence or diffusion to sinks, this can significantly advance understanding of long-term evolution of radiation induced defects and microstructures of SiC under irradiation.

1.4.3 Grain boundaries as defect sinks

It is known that interfaces, such as grain boundaries (GBs), can act as sinks to annihilate radiation-induced defects inside solids. Defect denude zone[92] near GBs have been reported in both alloys and polycrystalline SiC. One such example is shown in Figure 1-11. CVD-SiC with grain size 5-10 μm was irradiated by neutrons to a fluence ranged from 1.4×10^{25} to 1.9×10^{25}

n/nm^2 at temperature over 1000°C. TEM characterization shows clear dislocation loop denude zone near GBs in these irradiated samples. Furthermore, the width of denude zone increases as the radiation temperature increases, which implies the enhanced sink strength of GBS due to accelerated defect diffusion at higher temperatures. In addition to direct experimental observation, theoretical works have also shown a strong thermodynamic driving force for defects to be absorbed by GBs[93]. Besides that, a recent study implies the strain field near GBs can drive biased diffusion of defects toward GBs[94]. GBs have also been found to heal nearby radiation induced defects by releasing pre-absorbed defects[95]. This is shown by an accelerated MD simulation of displacement cascade in Cu when interstitials are preferentially absorbed by GBs while vacancies are left in nearby lattice. In the post-cascade simulations, the pre-absorbed interstitials are released from GBs to recombine with nearby vacancies by a series displacement of atoms in a chain.

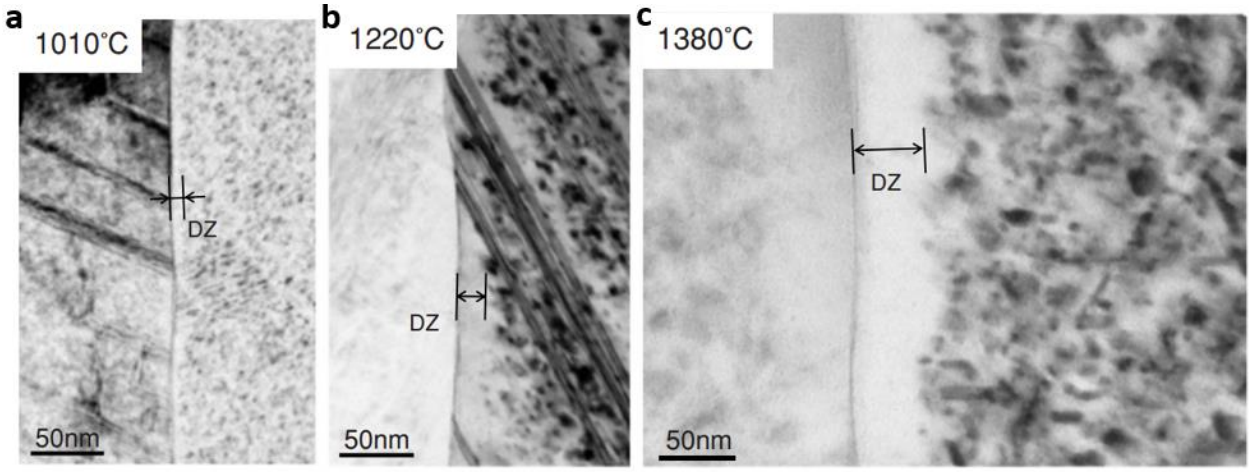

Figure 1-11 | Defect denuded zone near GBs in SiC irradiated by neutrons at different temperatures. **a**, 1010°C; **b**, 1220°C; and **c**, 1380°C. Adapted from Ref.[92].

The ability of GBs to absorb and annihilate defects have stimulated active studies on increasing GB density in materials to retard defect accumulation induced by radiation. Increasing

GB density can be done by reducing the grain size of polycrystalline materials or introducing layered structures in composite. A number of studies in both metals and ceramics have already shown the expected reduction in defect accumulation upon increased grain boundary density. For example, Shen *et al*.[96] showed a substantial enhancement in irradiation induced amorphization resistance for single-phased nanocrystalline (nc) versus large-grained polycrystalline $MgGa_2O_4$. By synthesizing bulk nano-layered CuNb composites containing interfaces, Han *et al*.[97] designed the material which shows nearly void free after irradiation while pure Cu samples irradiated at the same condition have obvious large voids. The success of increasing GB density to retard defect accumulation under irradiation suggests this approach a potential path for improving the radiation resistance of SiC. Many studies have been done to investigate the radiation response of nc-SiC versus μc-SiC or single crystal (sc) SiC[98-102]. In these studies, the radiation response of SiC is characterized by the dose to amorphization at different temperatures. However, the published trends have not been consistent throughout all these studies and they include reports of deterioration, improvement, and no change in radiation resistance of SiC to amorphization with grain refinement, as shown in Figure 12. These experiments differ in factors such as the type of irradiation species, the microstructure of SiC samples, and the method of observation (in situ versus ex situ), and all these factors could potentially contribute to the contradictory results. Regardless of these factors, these studies do suggest that the role of GBs as defect sinks may be limited in some cases.

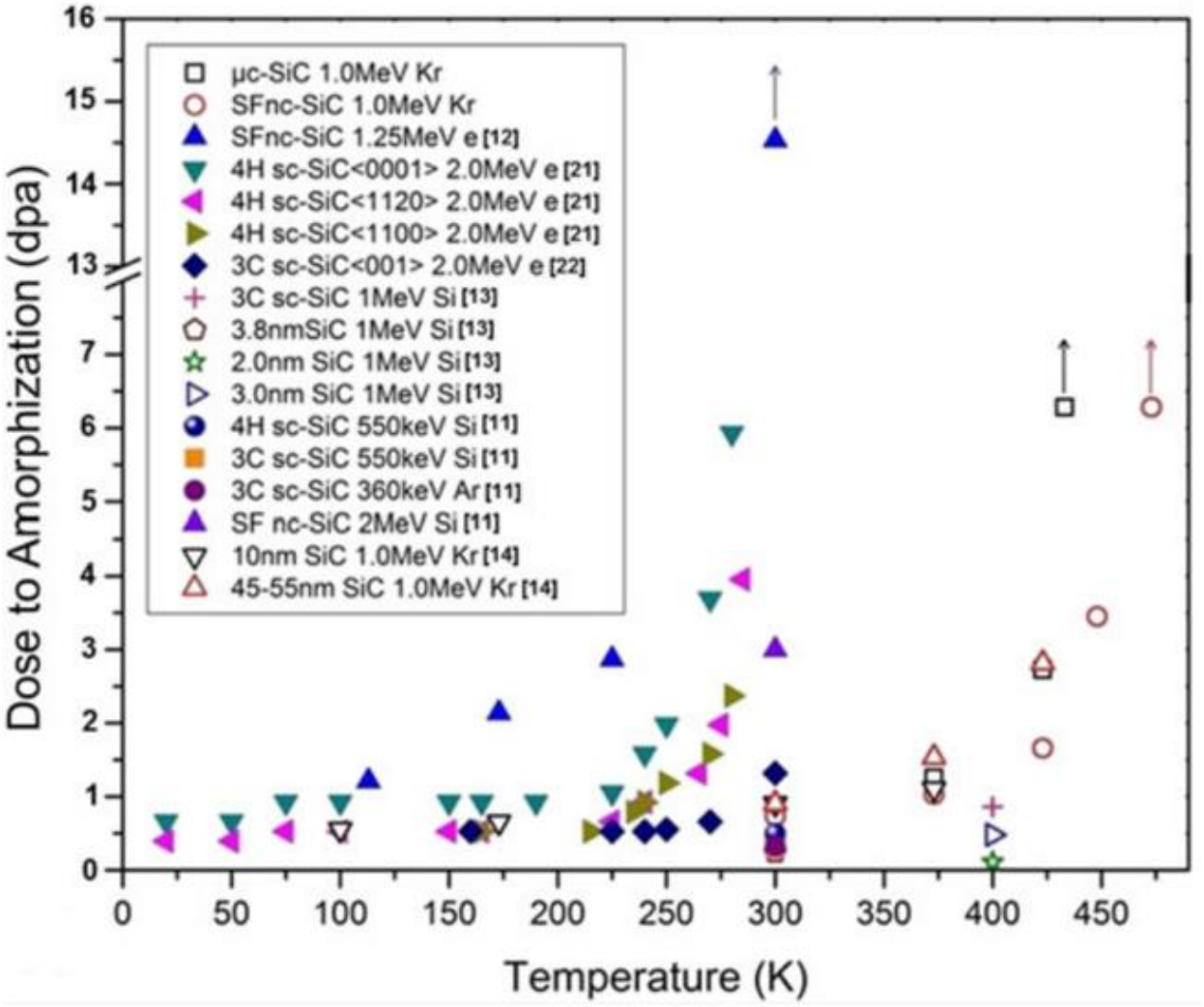

Figure 1-12 | Radiation dose to amorphization of nc-, μc-, and sc-SiC at different temperatures. Filled data points mean improvement in resistance to amorphization by reducing grain size and open points mean decrease in resistance to amorphization by reducing grain size. Adapted from Ref.[100].

One hypothesis to explain the lowered dose to amorphization in nc-SiC is interstitial starvation near GBs. Interstitial starvation can occur when interstitials are more mobile than vacancies, as is the case in SiC. Interstitials are able to move more readily to the GBs, or other sinks within the material, and are eliminated from the system in greater numbers than vacancies.

This creates an interstitial-denuded zone near GBs. The slow diffusion of vacancies and the lack of interstitial in this region to recombine with vacancies result in vacancy accumulation in this region. The accumulation of vacancies can eventually lead to amorphization initiating at GBs. Interstitial starvation was first predicted by an *ab initio* based rate theory study on polycrystalline SiC under irradiation[54]. The rate theory model predicts a significant high concentration of vacancies accumulated near GBs that can potentially drive amorphization. Later on, experimental evidence of interstitial starvation was reported by using STEM to characterize disorder magnitude near GBs in SiC[103]. In this study, CVD 3C-SiC samples with grain sizes ranging from 1 μm to 5 μm were irradiated by 1 MeV Kr ions at 100°C. Several irradiation doses were selected to obtain partially and fully amorphous SiC after irradiation. STEM analysis on the partially amorphous sample demonstrates that GBs always have a higher amorphization fraction than those regions within the grain interiors. This implies that GBs increase the rate of amorphization in their vicinity, which agrees with the hypothesis of interstitial starvation. The model prediction and experimental observation of interstitial starvation suggests that GBs do not always have positive effects on the stability of SiC lattice under irradiation.

Nowadays, it has also been established that GBs cannot always behave as perfect sinks which can absorb infinite amount of defects. The ability of GBs to absorb defects (sink strength) depends on many factors, including radiation environments (dose rate, temperature, etc.), GB characteristics (tilt, twist, mixed), and on-the-fly evolution of GB structure. Dependence of GB sink strength on the intact GB structures has been a hot topic in recent years. Lots of static properties (e.g., formation energy) and dynamic properties (e.g., migration barrier) of defects in intact GB structures have been studied[104-111]. For examples, Tschopp *et al.*[104] investigated the distribution of defect binding energy in 170 tilt and twist GBs in Fe and concluded that both

local structure of GBs and distance to GBs have a significant influence on the magnitude of binding energies. Uberuage *et al*.[105] investigated the mobility of both point defects and defect clusters in a few tilt, twist and mixed GBs in Cu. Based on the kinetics of defects in intact GBs, a rate model was developed to determine the sink strength of these GBs. These studies are very helpful to understand the interaction between different types of intact GBs and defects. However, because GB structures can change as defects accumulate at the interface, the energy landscape may change correspondingly. In this scenery, knowledge on interaction between intact GB and defect alone is not enough to predict long-term evolution of GBs under harsh environments. Therefore it becomes of critical importance to understand how GB structure can evolve under defect accumulation.

Recently, some efforts have been done to shed light on this question and most of these studies focus on tilt GBs[112-117]. It is known that tilt GBs, especially small angle tilt GBs, are composed of sets of edge dislocations in the interface, and point defects can be absorbed to edge dislocations by dislocation climb. For example, by load interstitials to tilt GBs in Mo, Novoselov *et al*.[112] showed tilt GBs accommodate defects by edge dislocation climb and GB energy evolves in a repeatable pattern as a function of the number of interstitials loaded onto GBs. Similar repeatable pattern in GB energy and free volume were also reported in continuous loading vacancies onto tilt GBs in Cu. Besides dislocation climb, Frolov *et al*.[115] recently found that edge dislocation core in tilt GBs in Cu can reconstruct in response to different atom density at the interface. They proposed this could be one possible mechanism that tilt GBs can accommodate a certain amount of interstitials and vacancies under irradiation environments.

These studies are very helpful. However, they only focus on one aspect of the defect-GB interaction, either defect properties at GB, or GB structure evolution under defect accumulation.

In real conditions, defect diffusion along GBs to other sinks and defect accumulation at GBs to drive structural change can happen simultaneously. It is of great importance to consider both processes in one model to simulate the real-time evolution of GBs under irradiation conditions. However, this ambition has been challenged by the timescale of different kinetic process. For investigation of defect properties and GB structural evolution, atomic simulations such as MD and DFT are the most appropriate techniques. While the timescale for defect segregation to GBs and defect diffusion along GBs is usually beyond that of typical atomic simulation timescale. In this case, kMC or rate theory based modeling are necessary. Therefore, it is necessary to develop multiscale simulations to shed light on this complicated question.

While interactions between defects and tilt GBs as well as the long-term structural evolution of tilt GBs are relatively well understood, the question of how twist GBs evolve to accommodate defects has been rarely touched. Compared to edge dislocations in tilt GBs, screw dislocation network in twist GBs is far more complicated and it is still unclear how exactly screw dislocations can annihilate point defects. So far, only few studies[118-119] tentatively try to answer this question. In early 2012, Matínze *et al.*[118] investigated the segregation of vacancies to {001} twist GBs in Cu by a kMC model. The {001} twist GBs feature square grid of screw dislocations. They found under low vacancy loading rate, vacancies can diffuse to dislocation networks and form voids. While under high vacancy loading rate, vacancies aggregate and form voids at both dislocation core and in non-dislocation region in the GB plane. Later that year, this group investigated the segregation of vacancies in {110} twist GBs in bcc Fe and {111} twist GBs in fcc Cu using an advanced kMC model[119]. The Fe {110} twist GBs feature hexagonal screw dislocation network, and the Cu {111} twist GBs feature alternating stacking fault (SF) and unfaulted region in triangular shape separated by partial dislocations. A strong preference for

vacancy to segregate to dislocation intersections was reported in both cases. What's more interesting, they found vacancies aggregation at dislocation intersections in Cu {111} twist GBs can lead to the shrink of SF area. From these studies, it is obvious twist GB structure undergoes noticeable structural change as defect accumulated at the interface. However, the number of vacancies loaded at GBs in these studies is too few (correspond to 10^{-4} dpa) to conclude long term evolution of twist GBs under irradiation.

A good understanding of how twist GBs evolve to accommodate defects is very important. On the one hand, twist GB is one major category of GBs (tilt, twist, mixed) and its radiation response are relevant for applications of poly-crystalline materials for components in reactors. On the other hand, a good understanding of twist GB's response to defect accumulation also provides insight on how general GBs (a combination of both tilt and twist feature) behave under irradiation, which is of broader interest to GB-defect interaction but still unclear up-to-date. Another interesting aspect of this question is how screw dislocation absorbs defects. Unlike edge dislocations climb to absorb point defects in tilt GBs, screw dislocations in twist GBs cannot climb. Previous studies found screw dislocation can absorb point defects or frank loops by forming mixed dislocation in the shape of helical turns. These mixed dislocations can climb to absorb defects due to its edge component. However, it is unclear whether screw dislocations at GBs with constrain from neighboring lattice can still accommodate defects in a similar way.

1.5 Thesis outline

In chapter 2, simulation and modeling techniques employed in this study including density functional theory, molecular dynamics, kinetic Monte Carlo, and rate theory modeling are introduced. Chapter 3 and Chapter 4 focus on my works on understanding the diffusion of defect

clusters in SiC. Both thermal diffusion and radiation induced diffusion of clusters in SiC are included in these chapters. In Chapter 5 and Chapter 6, my recent investigations on response of grain boundaries to fluxes of radiation induced defects in SiC are presented. It includes studies on the multiple roles of tilt GBs in annihilating interstitials and the structural evolution of twist GBs to absorb interstitial. In the last chapter 7, these works detailed in Chapters 3-6 are summarized, and possible future research directions are proposed.

Chapter 2 Methods

2.1 Density functional theory

2.1.1 Principles of Density functional theory

The governing equation of the time evolution of a quantum system is the Schrödinger equation

$$i\hbar\frac{\partial}{\partial t}\Psi(\vec{r},t) = \hat{H}\Psi(\vec{r},t) \tag{2-1}$$

where i is the imaginary unit, $\hbar$ is the Planck constant divided by 2π, t is time, $\vec{r}$ is the spatial vector that represents the positions of all the particles in the system (i.e., [x_i, y_i, z_i]), Ψ is the wave function of the quantum system, $\hat{H}$ is the Hamiltonian operator which characterizes the total energy of any given wave function of the system. The stationary quantum states of the system can be solved by the time-independent Schrödinger equation

$$\hat{H}\Psi_i(\vec{r}) = E_i\Psi_i(\vec{r}) \tag{2-2}$$

where E_i is the energy level of the stationary state Ψ_i, the non-relativistic Hamiltonian operator $\hat{H}$ can be written as:

$$\hat{H} = \frac{-\hbar^2}{2m}\nabla^2 + \hat{V}(\vec{r}) \tag{2-3}$$

where the first term is the kinetic energy, m is the particle mass, and ∇^2 is the Laplacian, $\hat{V}(\vec{r})$ is the operator representing the potential energy. For an arbitrary quantum system, if we can solve Equation (2-2) and find the eigenstates and the corresponding eigenvalues (i.e, the energy levels), we are able to know all the thermodynamic information of the system. However, analytical solutions to the stationary Schrödinger equation exist for only a very limited number of systems,

such as the problem of a single particle in a square potential well. For most of the quantum systems in the solid-state physics, the analytic solutions to the stationary Schrödinger equation do not exist. This is because the increased complexity in the $\widehat{H}$ for many-body system that includes electrons kinetic energy, electron-nuclei interaction, electron-electron interaction, nuclei kinetic energy, and nuclei-nuclei interaction.

One step to simplify $\widehat{H}$ is to ignore the operators for the nuclei kinetic energy. This is because the mass of the nuclei are typically thousands of times larger than the electron mass and the electrons move much faster than the nuclei. We can approximate the nuclei to be fixed at certain positions when the electrons move around the nuclei in the systems. This assumption is known as the Born-Oppenheimer or adiabatic approximation. With this approximation, the Hamiltonian can be simplified to be an operator only for the electrons. However, if we have *N* electrons in the system, the simplified Schrödinger equation still has 3*N* degree of freedom and is almost impossible to obtain the complete solutions of Equation (2-2).

Density functional Theory (DFT) is a method to numerically calculate the ground state of the many-body quantum system. The basic idea of DFT is that the density of electrons in the system $n(r)$

$$n(r) = \sum_{i=1}^{N} |\Psi_i(\vec{r})|^2 \tag{2-4}$$

can be considered as a basic variable and all the properties of the quantum system can be expressed as unique functional of $n(r)$ in the ground state. With this idea, a universal functional of the energy $E(n(r))$ can be defined in terms of the density $n(r)$. Ground state energy can be obtained by optimizing $n(r)$ to minimize the functional $E(n(r))$. The great achievement of the DFT is that the previous complicated 3*N* degrees of freedom problem is now transferred to a

problem of minimizing an energy functional $E(n(r))$ where $n(r)$ only has three dimensions (x, y, z) in space.

To develop the energy functional $E(n(r))$ and to perform $E(n(r))$ minimization, we rely on the Kohn-Sham approach. The key idea of Kohn-Sham approach is that the exact ground state density $n(r)$ can be represented by the ground state density $n(r)$ of an auxiliary system of non-interacting particles. The Hamiltonian of the auxiliary independent-particle system can be written in the same format in Equation (2-3) with $\hat{V}(\vec{r})$ representing the operator on the effective potential energy of the auxiliary independent-particle system. In this approach, $E(n(r))$ can be written as

$$E\big(n(r)\big) = T_{\mathrm{s}}(n(r)) + \int \mathrm{d}r V_{\mathrm{ext}}(r) n(r) + E_{\mathrm{Hartree}}\big(n(r)\big) + E_{\mathrm{ex}}\big(n(r)\big) + E_{\mathrm{II}} \qquad (2\text{-}5)$$

where T_{s} is the kinetic energy as a functional of density $n(r)$, $V_{\mathrm{ext}}(r)$ is the potential representing interactions between electrons and nuclei, as well as any external potential such as electric field. E_{Hartree} is the classical Coulomb interaction energy of the electron density interacting with itself. E_{II} is the interaction between nuclei, and it can be treated as a constant under the Born-Oppenheimer approximation. $E_{\mathrm{xc}}(n)$ is the exchange-correlation energy functional which represents the differences between the many-body quantum system and the independent-particle system. Details of the exchange-correlation functional can be found in details in[120].

Now we have developed the energy functional $E(n(r))$, and the next step is to do $E(n(r))$ minimization with respect to $n(r)$. Here we will skip the mathematical details and directly show the answer. The variation of $E(n(r))$ with respect to $n(r)$ gives the Kohn-Sham equation:

$$\hat{H}\Psi_i(r) = \varepsilon_i \Psi_i(r) \qquad (2\text{-}6)$$

where ε_i are the eigenvalues, and the Kohn-Sham effective Hamiltonian $\hat{H}$ can be expressed as

$$\hat{H} = \frac{-\hbar^2}{2m}\nabla^2 + V_{ext}(r) + V_{Hartree}(r) + V_{xc}(r) \quad (2\text{-}7)$$

the definitions of the terms V_{ext}, $V_{Hartree}$ and V_{xc} follow the description of the Equation (2-5). By starting with an arbitrary $n(r)$, we can calculate $\hat{H}$ using Equation (2-7). With $\hat{H}$ ready, the single particle Equation (2-6) can be solved to obtain the N eigenstates $\Psi_i(r)$ with the lowest eigenvalues ε_i. Then by using Equation (2-4) we will get the new density $n(r)$. It naturally leads to the self-consistent approach to optimize $n(r)$ and minimize $E(n(r))$, as shown in Figure 2-1. For the outputs of the DFT calculations, many properties of the ground state can be obtained, such as the ground state energy of the system, the force on each nucleus (can be used to relax the atomistic structure), the charge density of the system, the electronic density of states and the electronic band structure of the material and so on.

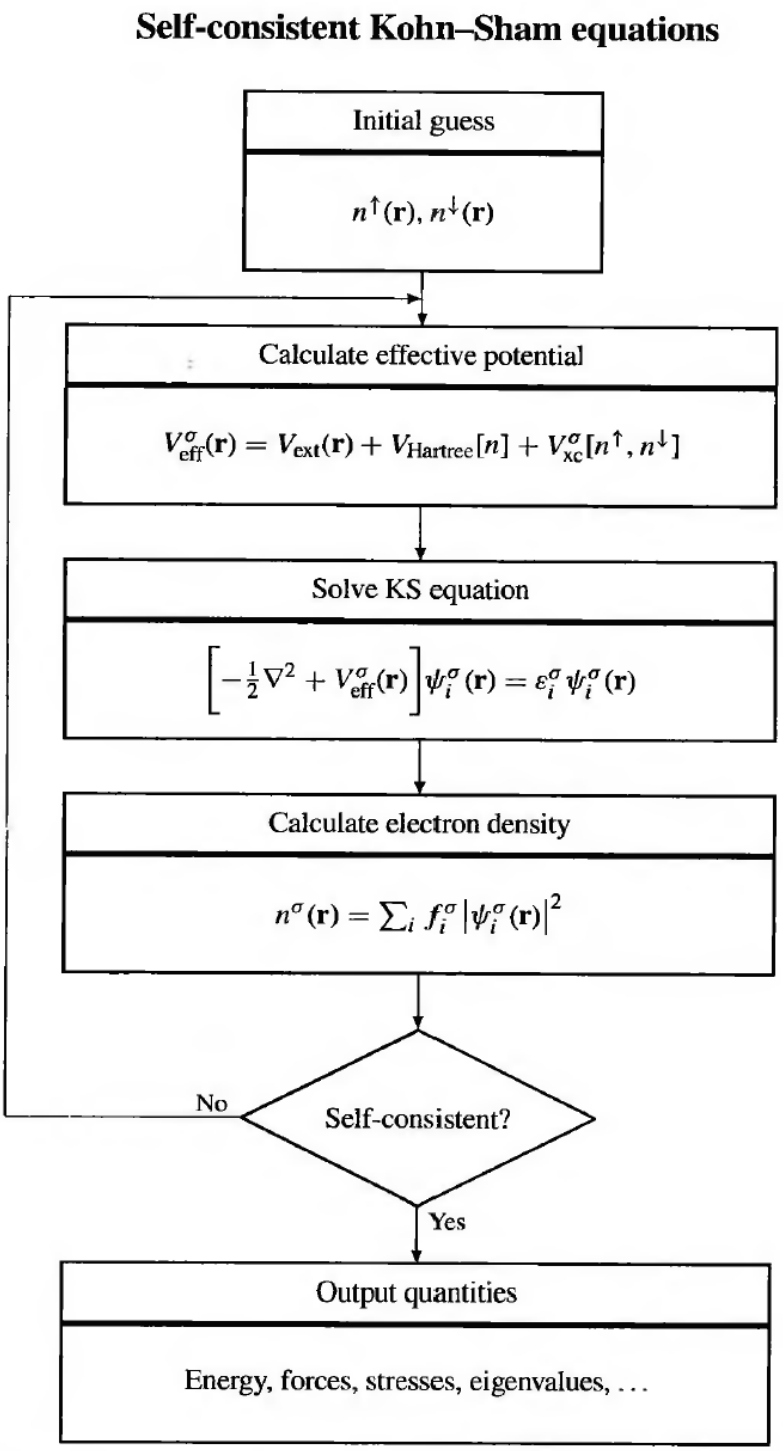

Figure 2-1 | Schematic presentation of the self-consistent loop for solving Kohn-Sham equations. Adapted from Ref.[120].

2.2.2 Implementation of DFT calculations for SiC

There are a few parameter and concepts that need to be introduced to show the implementation of DFT calculation for SiC. First of all, we need to develop a mathematical formula for the electron wave functions $\Psi_i(\vec{r})$. For crystalline materials, the most commonly used choice is the plane-wave function basis because of the periodic structure of the crystalline materials. The mathematical expression is:

$$\Psi_k(\vec{r}) = \sum_{\vec{G}} c \cdot \mathrm{e}^{\mathrm{i}(\vec{k}+\vec{G})\cdot\vec{r}} \tag{2-8}$$

where the exponential term is a plane wave, $(\vec{k}+\vec{G})$ is the wave vector. The pre-exponential term is the linear combination coefficient of each plane wave. In practice, we cannot include infinite number of plane-wave functions to express a certain electron eigenstate. So a cut-off energy E_{cut} is usually introduced to truncate the summation in Equation (2-8) within a relatively large wave vector. Convergence test on E_{cut} shows that an E_{cut} of 500 eV is enough for our DFT works on SiC the Vienna Ab-initio Simulation Package (VASP). The cut off energy can be different in a different DFT code.

Another important concept is that of pseudopotentials. Because the strongest interactions between the nuclei and the electrons usually happen near the nuclei, it leads to rapidly varying electron wave functions near the nuclei. This requires a very large E_{cut} to capture the wave functions. However, the wave functions near the nuclei do not significantly affect the chemical bonding, mechanical stability and electronic properties. Therefore, we can replace the strong Coulomb potential near each nucleus with a modified, weaker potential. This modification is called “pseudopotential”. The pseudopotentials used in DFT calculations include the core electrons as well. The nuclei and the core electrons are considered altogether as ions in the

system. The formulation of the pseudopotentials helps us improve the efficiency of the DFT calculations by reducing E_{cut} and consider atoms' valence electrons. Two of the most widely used versions of the pseudopotentials are the projector augmented wave (PAW) pseudopotential and the ultrasoft pseudopotential[121]. The PAW pseudopotential with valence electron configuration of $2s^2$, $2p^2$ for C and $3s^2$, $3p^2$ for Si is used for all DFT works on SiC in this thesis.

For the exchange-correlation functionals, LDA, GGA and hybrid functionals have been widely used in literatures. In the category of GGA functionals, two widely-used versions are the PW91 functional and the PBE functional. It is known that LDA shows over-binding for chemical reactions and this effect is largely corrected by GGA. Therefore, we use GGA-PBE for our calculations on SiC. In recent decades, LDA+U and GGA+U have been developed to solve the challenges that LDA and GGA often underestimate the bandgap, especially for transition metals. Given our main focus is defect structural and kinetic properties in SiC rather than electronic state, the +U technique is not employed in our calculations.

The last important concept is the *k*-point sampling in the reciprocal space. The details of applying Fourier transformation to obtain reciprocal space and Brillouin zone from periodic crystalline is shown in Ref.[120]. The advantage of using the reciprocal as the electron state representative originates is that a plane-wave function in the real space corresponds to a delta function (or literately a point) in the reciprocal space. Therefore, one electron state corresponds to one *k* point in the reciprocal space. This representation picture is much more convenient in contrast to describing the electron state in the real space where the electron wave function is non-local. In order to construct the density $n(r)$, we need to integrate over the reciprocal space. That being said, we need to make sure that enough k-points have been sampled in the BZ to get accurate results. In our DFT calculations, we use supercells containing 3×3×3 or 4×4×4 unit cells.

Energy convergence test shows a k-point mesh of 2×2×2 is sufficient to maintain accurate integration over the reciprocal space.

In this thesis, we use the Vienna Ab-initio Simulation Package (VASP) for all the DFT calculations. VASP is a plane-wave based DFT code written in the Fortran programming language. It runs in a UNIX operating environment. VASP calculations are typically run in parallel across multiple computing nodes and processors. The speed of the computing-time-expensive quantum mechanical simulation can be greatly enhanced by the parallel algorithm.

2.1.3 Structural relaxation and defect formation energy

Because DFT can solve multi-body system quantum mechanically, it provides the most accurate description about energy and forces within the system. The forces on atoms can be used to relax the structure of defects introduced into the supercell by adding or deleting atoms. Therefore, the stable configurations of defects in crystalline materials can be studied. In our calculations, structural relaxation is performed by using the conjugate gradient method in fixed supercell shape and volume. The stopping criterion of relaxation is that all forces on atoms are smaller than 0.02 eV/Å.

Furthermore, one can calculate the formation energy from the energy of the supercell with relaxed defect structure. More specifically for SiC, the formation energy of one defect can be calculated as:

$$E_f = E_{defect} - E_{lattice} - \sum_i \Delta n_i (E_i + \gamma_i) + q(\varepsilon_{VBM} + \varepsilon_F + \Delta V) \quad (2\text{-}9)$$

where E_{defect} is the energy of the supercell containing one defect, $E_{lattice}$ is the energy of the supercell without any defect, N_i is the number of atomic species i in the undefected cell minus the number of the same species in the defected cell, E_i is the energy of atomic species i in its

reference state, γ_i is the difference in energy of atomic species i between in SiC and in its reference state, q is the charge state of defect, ε_{VBM} is the energy of valance band maximum (VBM), ε_F is the Fermi level measured from VBM, and ΔV is the change of VBM induced by the defect. The reference states for Si and C are cubic Si and graphene, respectively. The chemical potential μ_i of species i equals to the summation of E_i and γ_i. Given the two elements in SiC, the formation energy of one defect can be calculated in either Si-rich condition or C-rich condition. In Si-rich condition, $\gamma_{si} = 0$, $\mu_{Si} = E_{Si}$, and $\mu_C = E_{SiC} - E_{Si}$ where E_{SiC} is the energy of a pair of C and Si atoms in SiC. In C-rich condition, $\gamma_C = 0$, $\mu_C = E_C$, and $\mu_{Si} = E_{SiC} - E_C$. The Si- and C-rich cases provide the bounds on the formation energy of defects with respect to the Si and C reservoir chemical potential ranges. The values of μ_{Si} and μ_C used to calculate defect formation energies are shown in Table 2-1. It is known that over a wide range of Fermi level, point defects in SiC are in the neutral states. Therefore, we only consider neutral defects in our calculation and the long term in Equation (2-9) is ignored.

Table 2-1 | Chemical potentials of Si and C used to calculate formation energy in SiC from Ref.[29].

Case	μ_{Si} (eV)	μ_C (eV)	γ_{Si} (eV)	γ_C (eV)
Si-rich	E_{Si} = -5.44	$E_{SiC} - E_{Si}$ = -9.65	0	-0.44
C-rich	$E_{SiC} - E_C$ = -5.89	E_C = -9.20	-0.44	0

2.1.4 Nudged elastic band and transition barrier

The Nudged Elastic Band (NEB) method[122] is used to find reaction pathways when both the initial and final states are known. Using this method, the Minimum Energy Path (MEP) for any given chemical process may be calculated, however, both the initial and final states must be known. NEB works by linearly interpolating a set of images between the known initial and final states, and then minimizes the energy of this string of images. Each image corresponds to a specific geometry of the atoms on their way from the initial to the final state, a snapshot along the reaction path. Thus, once the energy of this string of images has been minimized, the MEP is revealed. The transition barrier of this reaction is the energy difference between the lowest energy and the highest energy of images along the MEP. This transition barrier can be used to estimate the rate of this reaction, which is extremely helpful. For example, the transition barrier of one defect hop from one site to a neighboring site is often called migration barrier E_m. With known E_m, diffusion coefficient D at a fixed temperature T can be approximated as

$$D = \frac{1}{2d} a^2 \Gamma e^{-\frac{E_m}{k_B T}} \tag{2-10}$$

where d is the dimension of the diffusion, a is the travel distance in one hop, Γ is the hop frequency of atoms, and k_B is the Boltzmann constant.

In NEB, each interpolated image finds the lowest energy possible while maintaining equal spacing to neighboring images. This constrained optimization is done by adding spring forces along the band between images and by projecting out the component of the force due to the potential perpendicular to the band. The accuracy of the transition barrier in NEB is usually limited by many factors such as the number of images and the spring constant connecting neighboring images. For instance, if the number of image is too few, no image is interpolated near the saddle point and there is no chance of capturing the saddle point energy. Recently, a new scheme called climbing image NEB (cNEB)[123] has been developed to overcome these challenges. In cNEB, after a few standard NEB relaxation steps, the image with the highest energy is identified. The spring force on this image is removed and the true force at the image due to the potential along the elastic band is reversed. In this process, the force at the image due to the potential perpendicular to the band is unchanged. The image tries to maximize its energy along the elastic band, and minimize its energy in all other directions. The other images in the elastic band serve the purpose of defining the one degree of freedom for which a maximization of the energy is carried out. When the climbing image converges, it will be at the exact saddle point and gives accurate transition barrier.

In our calculations on transition barriers of reactions in SiC, the cNEB method is used. Either 3 or 5 images, depending on the displacement of atoms in the reactions, are used. The default spring constant of 5eV/Å is used, which does not affect the accuracy of cNEB result. The force convergence threshold for CI-NEB calculations is set at 0.05 eV/Å.

2.2 Molecular dynamics

2.2.1 Principles of molecular dynamics

Molecular dynamics (MD) is a technique for computer simulation of complex systems, modelled at the atomic level. In MD simulations, the time evolution of a system of atoms is followed via the solution of Newton's equations of motion

$$F_i = m_i \frac{\mathrm{d}^2 r_i(t)}{\mathrm{d}t^2} \tag{2-11}$$

where $r_i(t) = (x_i(t), y_i(t), z_i(t))$ is the position vector of ith particle and F_i is the force acting upon ith particle at time t, and m_i is the mass of the particle. 'Particles' usually correspond to atoms, although they may represent any distinct entities (e.g., specific chemical groups) that can be conveniently described in terms of a certain interaction law. To integrate the above second order differential equations, the instantaneous forces acting on the particles need to be specified. The interatomic force can be obtained by the gradient of interatomic potential $U(r_1, \ldots, r_N)$

$$F_i = -\nabla_{r_i} U(r_1, \ldots, r_N) = -\left(\frac{\partial U}{\partial x_i}, \frac{\partial U}{\partial y_i}, \frac{\partial U}{\partial z_i}\right) \tag{2-12}$$

where $U(r_1, \ldots, r_N)$ represents the potential energy of N interacting atoms as a function of their positions $r_i = (x_i, y_i, z_i)$.

Due to the many-body nature of the problem, the equations of motion are discretized and solved numerically. The MD trajectories are defined by both position $(r_1, \ldots, r_N)$ and velocity vectors $(v_1, \ldots, v_N)$ at different simulation time t. Accordingly, the positions and velocities are propagated with a finite time interval using numerical integrators, for example the Verlet algorithm. The aim of the numerical integration of Newton's equations of motion is to find an expression that defines positions $r_i(t+\Delta t)$ at time $t+\Delta t$ in terms of the already known positions at

time *t*. Because of its simplicity and stability, the Verlet algorithm is commonly used in MD simulations. The basic formula for this algorithm can be derived from the Taylor expansions for the positions $r_i(t)$; it reads as

$$r_i(t + \Delta t) = 2r_i(t) - r_i(t - \Delta t) + \frac{F_i(t)}{m_i}\Delta t^2 \quad (2\text{-}13)$$

Ideally, small Δt is desirable to obtain exact trajectories. However, a too small Δt can limit the overall simulation timescale one can reach. In practice, Δt is determined by the fastest motions in the system. Bonds involving light atoms (e.g., the O–H bond) vibrate with periods of several femtoseconds, implying that Δt should be on a femtosecond scale to ensure stability and accuracy of the integration.

The changing in position of each particle in space with time is defined by $r_i(t)$, whereas the velocities $v_i(t)$ determine the kinetic energy and temperature in the system. As the particles move, their trajectories may be displayed and analyzed, providing averaged properties. The dynamic events that may influence the functional properties of the system can be directly traced at the atomic level, making MD especially valuable in investigating microstructural evolution. MD simulation can be performed in different ensembles including micro-canonical ensemble (NVE), canonical ensemble (NVT) and grand-canonical ensemble (NPT), etc. A thermostat (e.g., Nosé-Hoover thermostat) or a barostat is used for constant temperature or pressure simulations, respectively. In a mathematical formulism, independent variables that describe interactions between system and external thermostat or barostat are introduced into the Equation (2-11) and (2-12). Details of mathematical expression and implementation of constant temperature and constant pressure MD simulation can be found in Ref.[124].

2.2.2 Empirical potentials for SiC

Many potentials have been developed for SiC, including Stillinger-Weber (SW)[125], Tersoff[126], Erhart and Albe[127], Environment-dependent interatomic potential (EDIP)[128], Vashishta[129], Gao and Weber (GW)[130]. Among them, the Vashishta and GW potential was developed to fit properties of point defects in SiC, while other potentials were developed for Si, C, and SiC to fit various bulk properties as well as defect properties. In the past decade, Tersoff, EDIP, and GW have been widely used in literatures to investigate radiation-induced lattice defects in SiC. Here a review of these three potentials is shown.

Table 2-2 | Bulk proprieties and point defect properties in SiC from experimental measurement, DFT and empirical potential calculation.

	Exp.[131-132]	**DFT**[30, 124, 126]	**Tersoff**[126]	**EDIP**[128]	**GW**[130].
Bulk properties					
a (Å)	4.360	4.344	4.321	4.364	4.360
E_c (eV)	-6.34	-7.545	-6.165	-6.338	-6.412
C_{11} (GPa)	390	390	437	394	254
C_{12} (GPa)	142	134	118	142	225
C_{44} (GPa)	256	253	311	168	66
Point defect formation energy (eV)					
V_C		4.41	3.88	1.45	2.76
V_{Si}		7.41	3.29	4.18	3.30
C_{Si}		3.59	2.20	2.40	1.69
Si_C		4.01	4.5	2.74	7.79
C_i		C-C<100>	C-TSi	C-Si<110>	C-C<100>
		6.73	4.4	4.67	3.04
Si_i		Si-TC	Si-Si<110>	Si-C<110>	Si-TC
		8.97	12.11	7.78	3.97
Point defect migration barrier (eV)					
C_i	0.89±0.02	0.67	NA	1.50	0.74±0.05
Si_i	1.50±0.30	0.83	*	*	1.53±0.02

From Table 2-2, we can see Tersoff potential[126] provides a reasonable fit for a wide range properties compared to experimental measurement and DFT calculations. Lattice constant, cohesive energy, and elastic modulus predicted by Tersoff potential are reasonable. Furthermore, it gives formation energies of vacancies and antisites in the best agreement with DFT calculations among these three potentials. Given these point defects are massively produced in radiation cascade, this is one reason why this potential has been widely used in literatures to investigate cascade in SiC. However, Tersoff potential provides a poor description of interstitial properties in SiC. For example, Tersoff potential incorrectly predicts both the most stable configuration and formation energy scale of C and Si interstitials. Furthermore, because the formation energy of Si interstitial is so high, it is favorable for the below reaction

$$\mathrm{Si_i} + \mathrm{C_C} \rightarrow \mathrm{Si_C} + \mathrm{C_i} \tag{2-14}$$

This implies Si interstitials are naturally unstable with Tersoff potential. Once they diffuse or obtain certain energy, Si interstitials will be consumed by this reaction to generate Si antisites and C interstitials. Besides these, it is also reported the migration barrier for C interstitial with Tersoff potential is rather high. All these factors have limited the application of Tersoff potential to investigate process involves interstitials and long range diffusion of defects, such as clustering and defect segregation to GBs.

EDIP[128] was developed in recent years and it provides improved bulk properties as compared to Tersoff potentials. Besides, the most stable C interstitial configuration is described by this potential in good agreement with DFT calculations. The formation energy of C interstitial is also slightly improved compared to Tersoff potential. This makes EDIP a good fit for investigation of C interstitial related static properties, such as structure of C interstitial clusters. This is the reason why we have chosen EDIP to screen low-energy Carbon interstitial clusters in previous studies.

However, EDIP also favors the reaction shown in Equation (2-14). In addition, the diffusion barrier for C interstitial is high compared to DFT calculations. This also limits its application in investigation kinetic process involves defect diffusion in SiC.

GW potential[130] was developed by Gao and Weber with a goal to provide a reasonable description of point defect properties in SiC. This sacrifices its accuracy in describing some properties such as elastic modulus shown in Table 2-2, which is terribly off from experimental values. Therefore, one should avoid investigating stress and deformation of SiC using GW potential. However, its advantage in describing interstitial kinetics in SiC is incomparable. First, it correctly predicts the most stable configuration of both C and Si interstitials. Second, reaction shown in Equation (2-14) is energy unfavorable in GW potential so Si interstitial is stable. Last and most important, the diffusion barriers of C and Si interstitials in GW potential agree well with experimental measurement and DFT calculations. These factors make GW potential a good fit for investigation of defect diffusion in SiC. This is the reason why we have chosen this potential to investigate defect kinetics at GBs in SiC.

2.2.3 Structural analysis

Due to the fast calculations using empirical potentials, MD simulations can usually handle up to billions of atoms. In a large supercell containing many atoms, identify defects by visualization is often limited and one have to use structural analysis algorithm to distinguish perfect lattice regions and defected regions. Common neighbor analysis (CNA)[133] is a widely-used algorithm to identify which atoms are associated with which crystalline phases (FCC, BCC, HCP, etc.), and which atoms are associated with defects. This is done by computing a fingerprint for pairs of atoms, which is designed to characterize the local structural environment. Usually, two atoms are said to be neighbors or bonded, if they are within a specified cutoff distance r_{cut} of each other.

For densely packed structures (FCC and HCP), the cutoff distance is set to be halfway between the first and second neighbor shell. For the BCC lattice, two neighbor shells need to be taken into account, and atoms are considered to be bonded with their first- and second-nearest neighbors. To assign a local crystal structure to an atom, three characteristic numbers are computed for each of the *N* neighbor bonds of the central atom:

1. the number of neighbor atoms the central atom and its bonded neighbor have in common, n_{cn};
2. the total number of bonds between these common neighbors, n_b;
3. the number of bonds in the longest chain of bonds connecting the common neighbors, n_{lcb}.

This yields *N* triplets (n_{cn}, n_b, n_{lcb}), which are compared to a set of reference signatures to assign a structural type to the central atom. For example, the fingerprint of FCC atoms is 12×(421) which means: I. each atom has 12 bonded atoms; II. the number of common bonded atoms shared by each pair of bonded atoms (e.g., *i-j* atom pair in Figure 2-2a) is 4 (*k* atoms in Figure 2-2a); III. the total number of bonds between the common bonded atoms (*k* atoms in Figure 2-2a) is 2; IV. the number of bonds in the longest chain of bonds connecting the common neighbors (*k* atoms in Figure 2-2a) is 1. This is the only structural signature of FCC lattice. For HCP lattice, the signature is 6×(421) + 6×(422). For BCC lattice, the signature is 8×(666) + 6×(444).

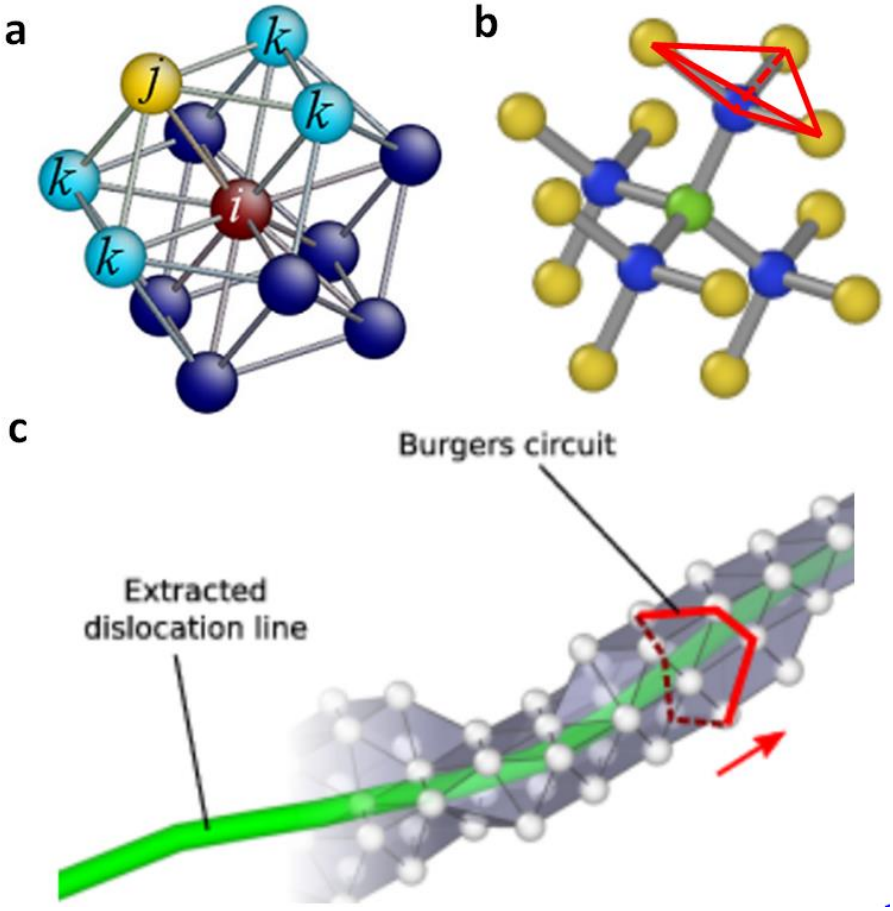

Figure 2-2 | Illustration of structural analysis. **a**, the (421) structure in FCC lattice; **b**, cubic diamond lattice; c, schematic drawing of dislocation analysis. Adapted from Ref.[133-134].

However, in either cubic or hexagonal SiC, the sub-lattice of C or Si is FCC lattice while the overall structure is diamond. This makes the conventional CNA algorithm not suitable for SiC. This is because the nearest neighbor atoms in diamond structure (blue atoms in Figure 2-2b) don not have common neighbors. In order to identify diamond structure, the CNA algorithm is modified as follows: First, the nearest neighbors of an atom are identified (the 4 blue atoms in Figure 2-2b). Then, for each of these four neighbors, their respective nearest neighbors are identified (the 12 yellow atoms in Figure 2-2b). This yields the list of second nearest neighbors of the central atom. Finally, the CNA fingerprint is computed for these 12 second nearest

neighbors and the central atom. If the CNA finger print agrees with that of a FCC lattice, then the central atom is classified as cubic diamond. If it agrees with that of a HCP lattice, then the central atom is marked as a hexagonal diamond atom.

In systems that contain dislocations, it is necessary to automatically identify dislocations and calculate the Burgers vector of each dislocation segment. This is performed by the dislocation analysis (DXA)[134] as implemented in Ovito. One fundamental concept in DXA is Delaunay tessellation which connects neighboring atoms to enclose the space inside triangular facets, as shown by the red lines in Figure 2-2b. Atom-to-atom vector along each edge (edge vector) of Delaunay tessellation is tentatively tried to be mapped to a corresponding vector in a perfect crystal lattice. If the edge vector can be mapped to any interatomic vectors in a perfect crystal lattice, the edge is considered as a good edge. The strain field induced by dislocations can stretch or shorten interatomic distance in neighboring lattice. This can deviate the vector of an edge vector from interatomic vectors in a perfect crystal, and thus identify the strained lattice region as defect region. To fix this, the CNA is performed to identify crystal regions before constructing Delaunay tessellation. To compensate for the strain effect, edges vectors of Delaunay tessellation in lattice regions identified by CNA are compared to interatomic vectors in a perfect lattice within a certain range. If the edge vector cannot be mapped to any interatomic vectors in a perfect crystal lattice, it is considered as a bad edge, which corresponds to regions in the dislocation core. Interfaces between dislocation core and perfect lattice can be constructed by the triangular facets (e.g., the facets in Figure 2-2c) with bad edges on one side but good edges on the other side. With this concept illustrated, the workflow of DXA is presented as follows. First of all, CNA is performed to identify dislocation core and their surrounding perfect lattice regions. Second, Delaunay tessellation is constructed, and good/bad edges are labeled. Third, interface

between dislocation core and perfect lattice regions are constructed by connecting facets with good edges on the perfect crystal side but bad edges on the dislocation core side. Last, a Burgers circuit is drawn by connecting edges of the interface facets (red circuit in Figure 2-2c) and the same circuit is mapped in a perfect crystal to calculate the Burgers vector.

2.2.4 Trajectory analysis

MD trajectories of point defects can be used to calculate point defect diffusion coefficient. The diffusion coefficients of single point defects can be derived from the displacements of all atoms in the system, without actually locating and following the defect itself during the run. For instance, the diffusion of a silicon vacancy occurs through short, nearest-neighbor displacements of atoms as they move into neighboring vacant sites. Without defects, none of the atoms in the supercell is displaced to a neighboring site during the simulation time of these simulations. All such displacements are a direct result of the motion of the defect. The point defect diffusion coefficients can therefore be calculated from the summation of the squared displacements over all atoms,

$$D = \sum_{i=1}^{N} (r_i(t) - r_i(0))^2 / 2dt \tag{2-15}$$

where N is the number of all atoms in the supercell, t is simulation time, and d is the dimension of the diffusion. Equation (2-15) is accurate in the limit of large simulation time t when a good linear relationship can be drawn between the square displacement and time t. In order to improve accuracy, average of D calculated from multiple simulations at the same temperature is often desirable. With defect diffusion coefficients obtained at different temperatures, the activation energy for defect migration E_m can be estimated from the Arrhenius relation

$$D = D_0 e^{-\frac{E_m}{k_B T}} \tag{2-16}$$

where D_0 is the pre-exponential factor and k_B is the Boltzmann constant.

2.2.5 Accelerated molecular dynamics techniques

One limitation of typical MD is its simulation timescale. This is because a small timestep in the timescale of sub-fs to fs must be used to maintain the correct integration of trajectory over time. This limits MD simulations to the timescale of μs (10^9 steps for a timestep of 1 fs). However, this timescale is usually not enough to observe reactions with high transition barriers. For instance, the rate of a reaction with a barrier of 2 eV at 1000 K is approximately 1/ms. That implies on average it takes approximately 1 ms to observe the occurrence of this reaction once, which is far beyond the timescale of MD simulations. Multiple acceleration techniques have been developed to extend MD simulation time scale, such as parallel replica dynamics[135] and hyperdynamics[136]. Here a brief review of these accelerated techniques is presented.

Parallel replica dynamics[135] is one straightforward way to accelerate a MD simulation. Many initially the same but independent replicas run on different processors, to increase the chance of exploration of the energy surface. The overall simulation clock is advanced by the sum of all the simulation times in replicas. The implementation of this technique is described below. First, the current configuration of the system is replicated on M processors, and a followed momentum randomization is performed on each replica to eliminate correlations with other replicas. Then each replica performs independent MD simulation and is monitored for transitions. A transition is said to occur if the summation of displacement of all atoms from the initial configuration is larger than a threshold. Once a transition is detected in any replica, for example, the ith replica, all replicas are stopped and the simulation clock is advanced by the sum of the time integration over all replicas. The configuration after the transition in ith replica becomes the new configuration of the system and is replicated on all processors. Parallel replica dynamics is easy

to implement and shows promising acceleration in certain simulations, e.g., the diffusion of vacancy in Cu (100) surface. However, when investigating high barrier transitions at low temperatures, because the rate itself is so slow, it still takes a long time to observe such a transition in any replica. Besides, even by using thousands of computers for replica simulation, the timescale is only advanced from μs to ms.

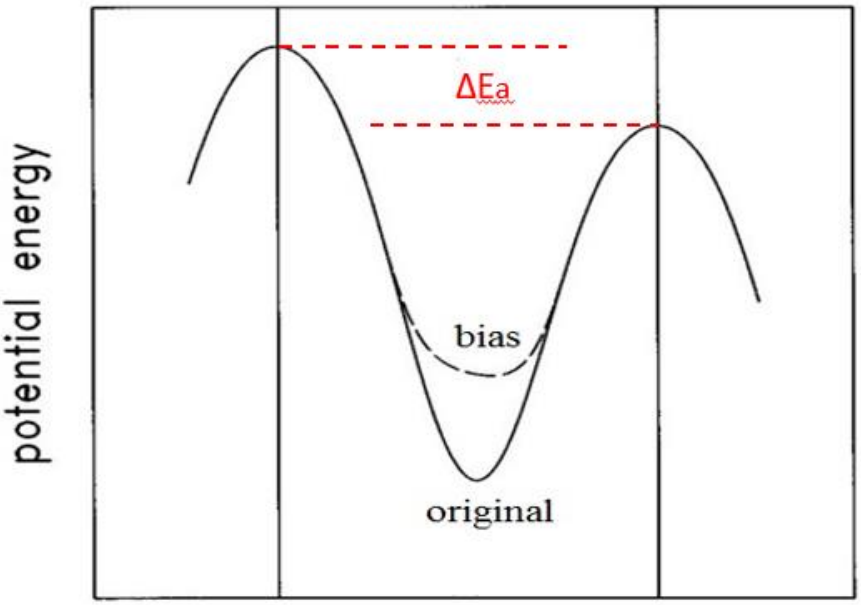

Figure 2-3 | The bias (dashed curve line) and original potential (solid) energy surface in hyperdynamics. Adapted from Ref.[136].

In hyperdynamics[136], in order to increase the rate of escaping from an energy basin, the potential is augmented by a bias potential, as shown in **Figure 2-3a**, to reduce the energy barrier of escaping transitions. As the barrier is reduced, these transitions can happen within MD timescale. The key of this technique is to maintain state to state evolution on the biased potential energy surface in the proper sequence as it should be at the original energy surface. Under transition state theory assumption, the ratio of the rate of any two transitions is determined by the activation energy difference ΔE_a:

$$\frac{r_A}{r_B} = \frac{\exp(-E_\alpha^A \cdot \beta)}{\exp(-E_\alpha^B \cdot \beta)} = \exp(-\Delta E_a \cdot \beta) \quad (2\text{-}17)$$

where ν is the attempt frequency, E_a is the activation energy, and $\beta=1/k_BT$, k_B is the Boltzmann constant. This implies that as long as the energy difference among saddle points ΔE_a remains unchanged, the correct kinetics starting from the initial state can be maintained. Therefore, one requirement of the bias potential is that it should not add any bias on the original potential at saddle points, as shown in Figure 2-3. In such a way, the bias potential can make sure the system evolves from state to state in a sequence representative of the exact dynamics, but at an accelerated pace. The time clock on the bias potential energy surface and on the original potential energy surface follows

$$\Delta t_b = \Delta t_{MD} \exp(\Delta V \cdot \beta) \quad (2\text{-}18)$$

where Δt_b is the time step on the bias potential energy surface, Δt_{MD} is the time step on the original potential energy surface, and ΔV is the energy difference between the bias and original potential at the current position of the trajectory. The challenge of this technique is to design the bias potential that meets the requirement of no bias at saddle point, smooth connection with original bias, and computationally efficient. This is very difficult since no priori information about neither neighboring states nor saddle points between them is available. So far this method has found its applications in low-dimensional system while its application in complicated systems is still in active research.

2.3 On-the-fly Kinetic Monte Carlo

2.3.1 Principles of Kinetic Monte Carlo

Kinetic Monte Carlo (KMC) attempts to overcome the timescale limitation of MD by exploiting the fact that the long-time dynamics of system typically consists of diffusive jumps from state to state. Rather than following the trajectory through every vibrational period as in MD, these state-to-state transitions are treated directly in KMC. The result is that KMC can reach vastly longer time scales, typically seconds and often well beyond.

First, we need to illustrate the concept of a state in KMC. Starting from any arbitrary atomic structure in a system, we bring the system to a local minimum by using steepest descent or conjugate gradient method. This defines a particular state *i* of the system. The geometry and potential energy of the state are the geometry and energy at the local minima, $\vec{r}_i$ and E_i, respectively. By giving each atom some momentum in MD, the system vibrates around this local minimum in the potential basin. We will say the system is still in state *i* because if we stop MD and minimize the energy, the system will fall back to the exact same geometry as the local minima $\vec{r}_i$. Adjacent to state $\vec{r}_i$, there are other potential basins, each separated from state $\vec{r}_i$ by an energy barrier. The lowest barrier connecting these states are the minimum barrier paths that go through the saddle points on the energy surface, as discussed in Section 2.1.4.

Because the system usually vibrates in the state for a long time, it forgets how it got there. This implies that the probabilities of different transitions to escape state *i*, have nothing to do with the history prior to entering state *i*. This characteristic is the defining property of a Markov chain. The state-to-state dynamics in this type of system correspond to a Markov walk. Because the transition out of state *i* depends only on the rate constants to other states $\{k_{ij}\}$, we can design

a stochastic procedure to propagate the system correctly from state to state. If we know these rate constants $\{k_{ij}\}$ exactly for every state we enter, this state-to-state trajectory will be indistinguishable from a (much more expensive) trajectory generated from a full molecular dynamics simulation.

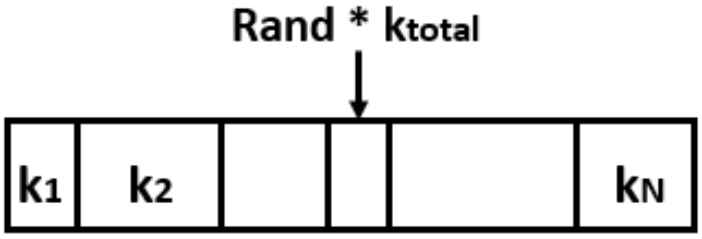

Figure 2-4 | Schematic illustration of the procedure for picking one transition among all transitions.

Assuming we know about the possible transition pathways, we can use transition state theory to compute the rate constant for each transition. The rate constant of system escaping from state *i* to state *j* is

$$k_{ij} = \Gamma e^{-\frac{E_a}{k_B T}} \tag{2-19}$$

where E_a is the energy barrier along the minimum barrier path, and Γ is atom vibration frequency. The stochastic procedure to move system from current state *i* to an adjacent state is explained blow and shown in Figure 2-4. We imagine that for each of all possible escape pathways we have an object with a length equal to the rate constant k_{ij} for that pathway. We put these objects end to end, giving a total length k_{tot}. We then choose a single random position along the length of this stack of objects by multiplying k_{tot} with a random number in (0,1]. This random position will "touch" one of the objects, and this is the pathway that we choose for the system to follow. This

procedure gives a probability of choosing a particular pathway that is proportional to the rate constant for that pathway, as it should.

As the stochastic path selection criterion has been demonstrated, the next step is to correctly advance the simulation time clock to account for the period that the system was trapped in state *i* before making a transition. Given the total escape rate k_{tot}, the probability the system has escaped from the current state is given by

$$P(t) = 1 - e^{-k_{tot} \times t} \tag{2-20}$$

Thus, the probability distribution function $p(t)$ for the system to escape at time t is the derivative of $P(t)$ with respect to t:

$$p(t) = k_{tot} e^{-k_{tot} \times t} \tag{2-21}$$

The probability distribution function $p(t)$ means the probability that the system has not escaped at time t but will escape within an infinitely small time window δt starting from time t. Therefore, the average time τ for the system to escape from the current state is

$$\tau = \int_0^\infty t p(t)\, \mathrm{d}t = \frac{1}{k_{tot}} \tag{2-22}$$

In theory, one can always update simulation time clock by using the average escape time τ in Equation (2-22) for each state. However, given the stochastic nature of the escaping process, an exponentially distributed random number is usually employed. In this case, the simulation clock is advanced in each KMC step by

$$\Delta t = -\frac{\ln(r)}{k_{tot}} \tag{2-23}$$

where r is a random number uniformly distributed in (0,1]. In long timescale simulation, this will give the exactly same simulation time as obtained by using the average escape time τ.

By ignoring local vibrations and only focusing on state-to-state transitions, KMC significantly advances the simulation timescale as compared to MD. To run a KMC simulation, all state-to-state transitions and the associated barriers should be known beforehand so the rate constants and total rates can be calculated. This is straightforward to simple kinetic process such as diffusion of vacancies. The vacancy can only jump to neighboring lattice sites and the transition barrier can be calculated by NEB. However, for complicated objects, such as defect clusters, and non-crystalline system, it is very challenging to obtain a full list of transitions. Take defect cluster diffusion as an example, one step in the diffusion (system move from one state to another) usually involves coordinated movements of many atoms. We usually find ourselves in situations where we have no idea about the atom movements that will lead to adjacent states and therefore cannot calculate transition barriers for a KMC simulation. This challenge can be addressed by on-the-fly KMC, which is discussed in details in Section 2.3.2.

2.3.2 Kinetic Activation Relaxation Technique

On-the-fly KMC does not require a pre-defined transition list. Instead, it automatically search transitions and generate the transition list that can be used to perform KMC modeling. There are several methods to perform on-the-fly KMC, such as the temperature-accelerated dynamics[137], the dimer method[138], and the Kinetic Activation Relaxation Technique[139]. In this section, the details of Kinetic Activation Relation Technique (K-ART) are reviewed. In k-ART, the Activation Relaxation Technique (ART)[139] algorithm, an open-ended saddle point searching algorithm, is combined with the kMC scheme. ART samples nearby transitions of a local minimum to generate transition lists with corresponding rates and the KMC algorithm executes a transition according to these rates. Figure 2-5 shows the flow chart of k-ART simulations. The only difference between k-ART and standard KMC simulations is the step in red square where

ART sample transitions and generates transition list. In standard KMC simulations, this step is replaced by reading from the pre-define transition list.

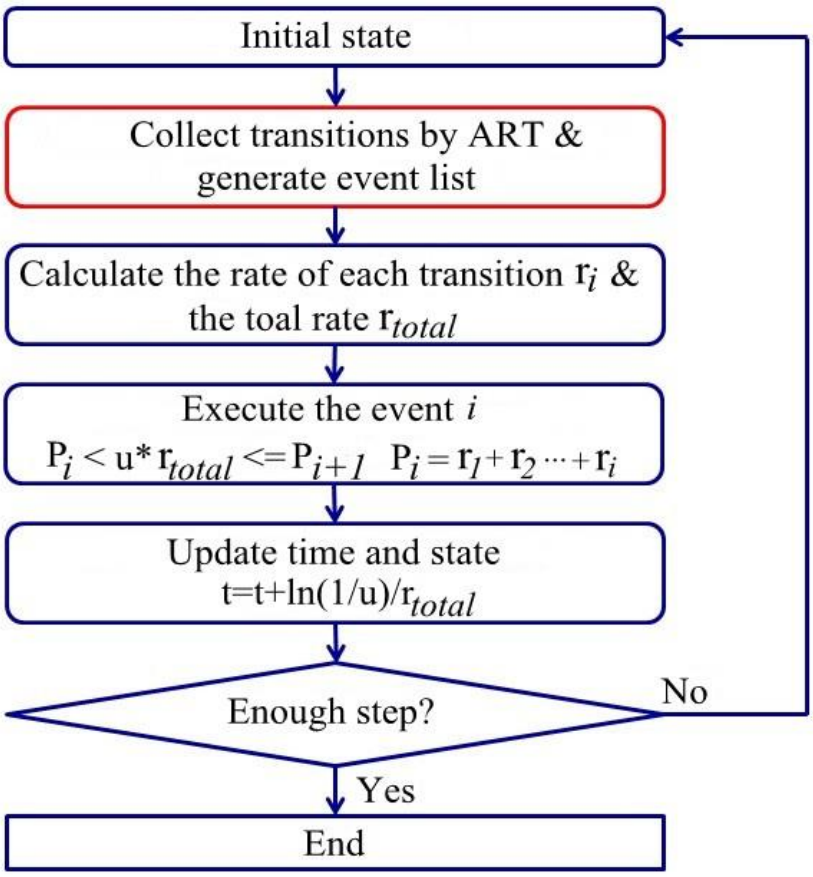

Figure 2-5 | The flow chart of k-ART.

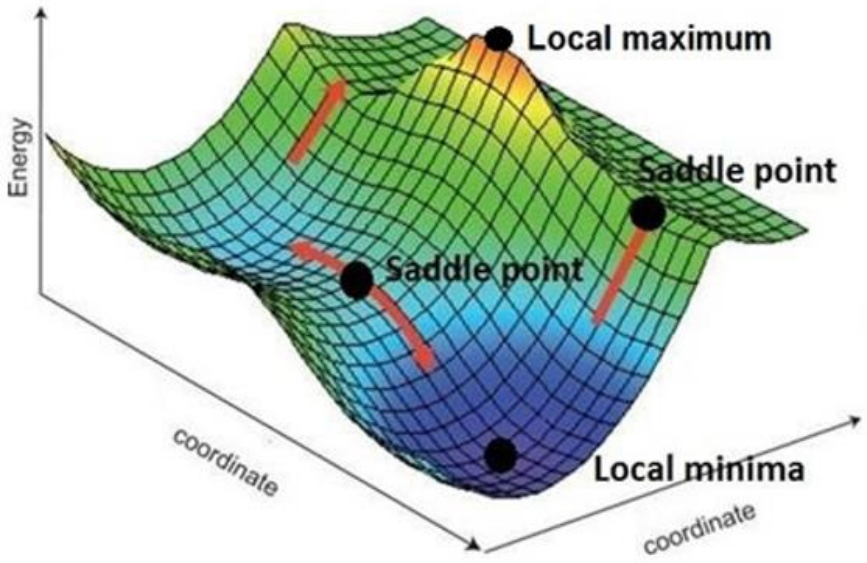

Figure 2-6 | Schematic drawing of an energy surface.

Before diving into details of implementation, it is necessary to introduce some background on energy landscape of many-atom system. In a many-atom system, the potential energy E is a function of the coordinates of all atoms $\vec{r}$ and $\vec{r} = (x_i, y_i, z_i)$, i = 1,…, N. Therefore, one specific $\vec{r}$ together with the potential energy $E(\vec{r})$ associated with it makes one point ($\vec{r}$, $E(\vec{r})$) in the 3N+1-dimensional space. The surface composed of numerous ($\vec{r}$, $E(\vec{r})$) is the energy surface which demonstrates the change of potential energy $E(\vec{r})$ with contiguous changes in coordinates $\vec{r}$. A schematic drawing of energy landscape with respect to only two variants is in shown in Figure 2-6. There are special points such as local minima, local maxima, and saddle points on the energy landscape. These points are all critical points with the 1st derivative of $E(\vec{r})$ with respect to any dimension being zero. However, to further identify a critical point being a local minima, maxima, or saddle point, one have to rely the 2nd derivative of $E(\vec{r})$ to $\vec{r}$, namely the curvature of the energy surface. Take the energy surface shown in Figure 2-6 as an example, given the 1st derivative of energy being zero, a local minimum is the point where curvature along any

direction is positive, and a local maximum is the point where curvature along any direction is negative, and a saddle point is the point where curvature is positive along some directions while negative along others. The matrix form of the 2nd derivatives of $E(\vec{r})$ to $\vec{r}$ is called Hessian matrix, as shown below.

$$Hessian\_Matrix = \begin{pmatrix} \frac{\partial^2 E}{\partial x_1^2}, \frac{\partial^2 E}{\partial x_1 \partial y_1}, \frac{\partial^2 E}{\partial x_1 \partial z_1} \cdots \frac{\partial^2 E}{\partial x_1 \partial x_N}, \frac{\partial^2 E}{\partial x_1 \partial y_N}, \frac{\partial^2 E}{\partial x_1 \partial z_N} \\ \frac{\partial^2 E}{\partial y_1 \partial x_1}, \frac{\partial^2 E}{\partial y_1^2}, \frac{\partial^2 E}{\partial y_1 \partial z_1} \cdots \frac{\partial^2 E}{\partial y_1 \partial x_N}, \frac{\partial^2 E}{\partial y_1 \partial y_N}, \frac{\partial^2 E}{\partial y_1 \partial z_N} \\ \vdots \\ \frac{\partial^2 E}{\partial z_N \partial x_1}, \frac{\partial^2 E}{\partial z_N \partial y_1}, \frac{\partial^2 E}{\partial z_N \partial z_1} \cdots \frac{\partial^2 E}{\partial z_N \partial x_N}, \frac{\partial^2 E}{\partial z_N \partial y_N}, \frac{\partial^2 E}{\partial z_N^2} \end{pmatrix} \quad (2\text{-}24)$$

The eigenvalues of the Hessian matrix are very helpful to examine the curvature of energy surface at a specific $\vec{r}$. If all the eigenvalues of the Hessian matrix are positive (negative), the curvature of energy surface at a specific $\vec{r}$ along any direction is positive (negative). If the Hessian matrix has both positive and negative eigenvalues, the curvature is positive along some directions while negative along the others. Recall that critical points with these features can be defined as local minima, or maxima, or saddle point. This implies we can identify these features on energy surface by two straightforward criterions. The first one is the 1st derivative of $E(\vec{r})$ to $\vec{r}$ at the specific $\vec{r}$, which is forces on atoms, to be zero. The second one is the eigenvalues of the Hessian matrix at the specific $\vec{r}$ to be all positive, or negative, or have both positive and negative to identify itself being local minima, or maxima, or saddle point.

Having the introduced background, we can now discuss the details of how ART can find the minimum energy path which connects two local minima through a saddle point. ART works in

three regimes: I leaving the local minima; II converging to a saddle point; and III Relaxation into a new minima. In step I, ART takes the following actions to leave the initial local minima:

1. A number of atoms are selected. These atoms can all atoms in the system, or can be limited to atoms in defects or other regions of interest;

2. These atoms are displaced by a small step Δr along random directions. This step introduces changes in $\vec{r}$;

3. After each displacement of this group of atoms, the coordinates of other atoms are slightly optimized to avoid unphysical stress build up;

4. The eigenvalues of Hessian matrix at current $\vec{r}$ are calculated by using a Lanczos procedure.

If the lowest eigenvalue is positive, this implies the system is still in regions near the initial local minimum. Step 1 to 4 are repeated until the lowest eigenvalue of the Hessian matrix becomes negative, which implies the system has left the local minimum and is now adjacent to a saddle point because the coexistence of both negative and positive eigenvalues.

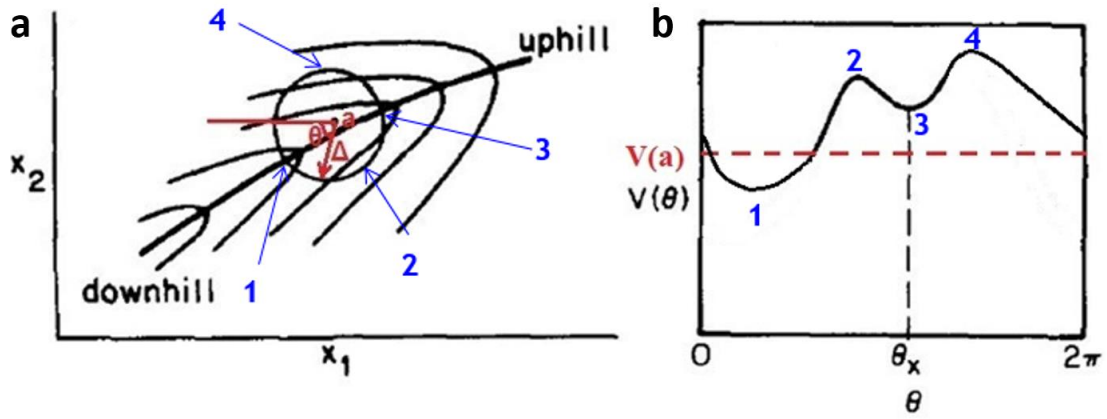

Figure 2-7 | **a**, An energy surface as a function of coordinates; **b**, The energy of the system as a function of θ, and θx denotes the steepest ascent path.

In regime II, the question now becomes how we can make displacement on atoms to move to the specific $\vec{r}$ that corresponds to the nearby saddle point. Again, here we use the energy surface with respect to two dimensions x_1 and x_2 as an example, as shown in Figure 2-7a. Assume we are at position a, and going to make a small step of Δ, how could we know the direction θ leading to the nearby saddle point (walking uphill on energy surface following the thick black line, downhill-to-uphill). Taylor expansion of the potential energy $V(\Delta, \theta)$ w.r.t. $V(a)$ can be expressed as

$$V(\Delta,\theta) = V(a) + \Delta(D_1\cos\theta + D_2\sin\theta) + \frac{\Delta^2}{2}(K_{11}\cos^2\theta + K_{22}\sin^2\theta + 2K_{12}\sin\theta\cos\theta) \quad (2\text{-}25)$$

where D_i and K_{ij} are the 1st and 2nd derivative of Hessian matrix along the ith and jth dimension. The path to walk uphill with minimum energy increment is path leading to point 3 in Figure 2-7a. It has been proved in math that this direction agrees with the direction of eigenvector of the lowest eigenvalue of the Hessian matrix. Then it is relatively straightforward to bring the system closer to the saddle point by pushing it along that direction with a small step Δ. After each step, the instantaneous eigenvector of the lowest eigenvalue of the Hessian matrix is calculated and the system is displaced along that direction again. In the meantime, the instantaneous forces on atoms are calculated to exam whether the system has reached to saddle point or not. To ensure a smooth convergence to the saddle point, the displacement Δ is decreased gradually as the steps increase. Once the system reached the saddle point, both atomic configuration and potential energy are calculated and stored.

In regime III, now it is necessary to nudge the system slightly over to force it to enter a region near a new local minimum. It is necessary to nudge the system because saddle point is a stable configuration where the 1st derivative of $E(\vec{r})$ to $\vec{r}$, or the forces on atoms, equal zero. To

nudge the system off the saddle point, the displacements of atoms $\Delta\vec{r}$ from the initial local minimum $\vec{r}_{initial}$ to the saddle point $\vec{r}_{saddle}$ are calculated. Then 20% of $\Delta\vec{r}$ are added onto the coordinates of atoms in the saddle point $\vec{r}_{saddle}$. By doing this, the system is now literally pushed over the saddle point away from the initial local minimum. Finally an energy relaxation by the conjugate gradient method is applied to relax the system into the new local minimum. The atomic configuration and potential energy are calculated and stored.

By working through these three regimes in sequence, ART can find a transition starting from the initial local minimum to a nearby local minimum, and also give the saddle point energy connecting them. The transition barrier can be calculated as the difference in energy between the initial local minima and saddle point, which will be used to calculate rate for KMC modeling. Ideally, one should run ART starting from one initial local minimum for many times to achieve exhaustively sampling all possible transitions. This can ensure the correct estimation of the total rate escaping this minima and the correct dwelling time system spent in this minima. However, running ART for many times is computationally expansive and better sampling method should be developed to boost efficient. Given the atomic structure of simulation target (point defect, clusters, or amorphous materials) and hence the corresponding energy surface vary from case to case, we do not provide a general solution to this problem. Instead, in Section 3.1.1, we will show details of our implementation of ART, solution to exhaustive sampling, as well as parallelization of ART to boost transition search efficiency, for a carbon tri-interstitial cluster in SiC.

In summary, k-ART is a combination of an open-ended saddle point searching algorithm ART and the typical kMC model. Such a combination enables the system to hop on the energy surface without knowing transition paths and barriers beforehand. This feature is extremely

useful to simulation the evolution of rate events in a complicated system, such as clusters diffusion or structural evolution of amorphous materials.

2.4 Rate theory model

The rate theory framework for modeling radiation effects describes the spatial and temporal evolution of concentrations (C_i) of various defects (i) produced during irradiation. The master equations of rate theory are:

$$\frac{\mathrm{d}C_i}{\mathrm{d}t} = D_i \nabla^2 C_i(\vec{r}, t) + K_0 - K_{ij} C_i C_j \tag{2-26}$$

where D_i is the diffusion coefficient of ith defect at a certain temperature, $\vec{r}$ is the coordination in the simulation space which can be only x for one-dimension, or (x, y, z) for three-dimension, or (r, θ, φ) for radical coordinates in three-dimension. K_0 is the defect production rate, K_{ij} is the reaction rate coefficient of defect reaction between ith and jth defects, C_i and C_j are the concentration of ith and jth defects. The first term on the right-hand side of Equation (2-26) describe the special diffusion of defects due to concentration gradient, as determined by the Fick's diffusion law. The second term is defect production rate caused by radiation cascade, and the last term is the defect consumption rate due to reactions between defects, such as interstitial-vacancy recombination.

The total number of non-linear differential equations to solve in a rate-theory model is determined by what defects are of importance and of interest to the problem. The basic form would be solving two coupled equations for interstitial and vacancy in single-element materials. For comprehensive prediction of point defect concentrations in SiC, six coupled equations should be solved to take into account C/Si interstitial, C/Si vacancy, and C/Si antisite. Initial and boundary conditions are needed to solve these coupled differential equations. The initial

condition is straightforward as it assumes the initial concentration of defects equals to the concentration equilibrium of each species:

$$C_i(t = 0) = C_i^{eq} \tag{2-27}$$

The boundary condition depends on the specific geometry and types of defect sinks considered. For a spherical geometry to represent grains, grain boundaries at $r = R_0$ where R_0 is grain radius, can be considered as sinks to defects. In this case, defect concentrations near sinks are assumed to be equal to equilibrium concentrations, and the boundary conditions can be written as

$$C_i(r = R_0) = C_i^{eq} \tag{2-28}$$

It is very challenging to obtain analytical solution of these sets of non-linear differential equations, and numerical solution is usually used for analysis.

With the framework explained, now let us dive into details of each term in Equation (2-26). The concentration-induced diffusion term is self-explanatory. The radiation-induced defect production rate K_0 can be calculated as

$$K_0 = \Gamma \eta \alpha_i \tag{2-29}$$

where Γ is the dose rate (dpa/s), η is the cascade efficiency, and α_i is the generation fraction of ith defect. Cascade efficiency η is the ratio of the number of generated defects to the number of displacements in a cascade. Details on calculation of η can be found in Ref.[49]. Generation fraction α_i is usually obtained by statistical analysis of various defects generated in MD simulations of cascade. The defect reaction rate K_{ij} can be categorized into two groups depends on the reaction energy landscape:

$$K_{ij} = 4\pi r_{ij}(D_i + D_j) \text{ if } E_m >> E_r \tag{2-30}$$

$$K_{ij} = 4\pi r_{ij}(D_i + D_j)e^{(E_m^{fast} - E_r/k_B T)} \text{ if } E_m \approx E_r \text{ or } E_m < E_r \quad (2\text{-}31)$$

In Equation (2-30) and (2-31), E_m is the diffusion barrier of specifies, E_r is the defect reaction barrier, E_m^{fast} is the diffusion barrier of the faster diffusion species, and r_{ij} is the interaction radius for the reaction. In the first case when $E_m >> E_r$, the reaction is diffusion controlled process. In the second case when if $E_m \approx E_r$ or $E_m < E_r$, the reaction is a reaction controlled process. The reaction rate is calculated differently in these two cases.

A previously developed rate theory model for SiC[54] will be employed in this thesis and details of this model is reviewed below. In order to obtain comprehensive prediction of point defect concentrations in SiC, six coupled differential equations are developed to take into account C and Si interstitials, C and Si vacancies, and C and Si antisites. A spherical geometry is used and the radius of the sphere equals to the grain size of SiC. Defect concentrations at GBs ($r = R_0$) are fixed to be equilibrium concentrations. The initial condition is defect concentrations equal to equilibrium concentrations. This model takes defect diffusion and reaction parameters, such as formation energy, migration barrier, and reaction barrier, from accurate *ab initio* based calculations to unsure the correct description of defect kinetics. Defect reactions including interstitial-vacancy recombination and interstitial-antisite kick off reaction. The interstitial-vacancy recombination includes not only the recombination between interstitial and vacancy in the same species, but also that in different species (e.g., a C interstitial recombines with a Si vacancy to form a C_{Si} antisite). The interstitial-antisite kick off reaction is the process that when one interstitial of one species (e.g., Si interstitial) encounters an antisite of the other species (e.g., C antisite), the interstitial replace the antisite. In the process, local stoichiometry is restored and an interstitial of the other species (e.g., C interstitial) is produced. This rate theory mode and the

corresponding code as explained in more details in Ref.[54] are employed in this study to determine point defect concentration profile in SiC under irradiation.

Chapter 3 Defect Clusters in SiC: Thermal Diffusion*

Up to this point, the mobility and dynamics of defect clusters in SiC have not been investigated. Quantification of cluster dynamics is, however, important for understanding of processes that control high-temperature annealing of defects introduced during ion implantation or thermal oxidation, and for predicting radiation response of SiC (e.g., swelling and thermal conductivity) under given temperature and irradiation conditions. For example, if small defect clusters can diffuse over a wide range temperature, one need to consider processes such as cluster coalescence or cluster diffusion to sinks in models to correctly predict cluster size and density under irradiation. In addition to migration of the clusters, cluster rotation is also of potential interest. Recent studies of irradiation creep of SiC suggested that anisotropic distribution of small dislocation loops on {111} planes under applied stress is responsible for the experimentally observed irradiation creep. These loops were hypothesized to be formed by self-interstitial clusters and their formation and rotation behavior under stress is responsible for the anisotropic distribution.

A major challenge in predicting dynamics of defect clusters in SiC lies in the high defect migration barriers in this material and in short simulation time scales of standard molecular dynamics (MD, see details in Section 2.2.1) simulations. Multiple accelerated techniques have been developed in the community to extend MD time scale limitations, such as hyperdynamics, parallel replica dynamics and temperature-accelerated dynamics developed by Voter *et al.*[135-137] (see details in Section 2.2.5). Another widely used technique for long-time scale simulation is kinetic Monte Carlo (KMC, see details in Section 2.3.1). In this technique, the system hops from one energy minimum to another based on the known transition probabilities. The time is advanced in each hop based on the transition state theory. However, KMC requires a predefined

event lists for transitions out of each minimum, which is very challenging to achieve for cluster migration due to the unknown transitions and numerous intermediate states involved in cluster dynamics. To address this problem, several open-ended saddle point search algorithms have been proposed, including the activation-relaxation technique (ART)[139-143], the dimer method[138], and the autonomous basin climbing method[144]. When the KMC is combined with one of these algorithms, an on-the-fly KMC scheme can be developed and it can work on systems with complicated energy surface for a long-time scale simulation. In this section, we employ the kinetic activation-relaxation (k-ART, see details in Section 2.3.2), which is an on-the-fly KMC technique, to investigate dynamics of C interstitial clusters in SiC.

3.1 Implementation of k-ART

We focus on migration and rotation of a carbon tri-interstitial cluster $(C_{BC})_3$, which has been proposed to be one of the most stable small interstitial clusters in irradiated SiC[145]. This cluster is composed of three carbon interstitials occupying 3 neighboring C-Si bond center sites in the {111} plane and it is a common building block of other small carbon interstitial clusters[52]. For example, the GS of carbon penta-interstitial cluster is composed of a $(C_{BC})_3$ cluster with a neighboring $(C_{BC})_2$ complex, and the GS of carbon hexa-interstitial cluster is composed of two neighboring $(C_{BC})_3$ clusters. The kinetic activation-relaxation technique (k-ART) based simulation protocol developed here for studies of the $(C_{BC})_3$ cluster can be later employed to study other defects in this material.

The rotation and migration paths of the $(C_{BC})_3$ cluster are investigated using ART, a single-ended eigenvector-following method developed by Mousseau et al.[140] and modified later by several groups[146]. In the activation phase, the system is pushed out of equilibrium by displacing

selected atoms in steps of length 0.1 Å in random directions of the configuration space and a limited energy minimization is applied in the orthogonal hyperplane after each step. Selected atoms can be picked up randomly in the system or limited to, for example, the surface of a slab or a region containing defects. In our case, in order to focus on the movement of the interstitial cluster, selected atoms are chosen to be the interstitials in the cluster and their nearest neighbor lattice atoms. The system is moved step by step until a configuration is found where the Hessian matrix has a negative eigenvalue. In the convergence phase, the system is moved along the eigenvector of the negative eigenvalue of the Hessian matrix with an adaptive step length until either a saddle point is found or the system falls back into the original local minimum. In the former case, the system is subsequently pushed over the saddle point and relaxed into a local minimum. In the latter case, a new random search is started from the initial configuration. Although ART can work with ab initio software, e.g., with SIESTA and BigDFT, the large number of force evaluations required to converge to a saddle point makes such calculations very time consuming. In our simulations, we combine ART with the environment-dependent interatomic potential (EDIP)[128]. The EDIP potential is chosen since it provides a good description of energetics of point and extended defects[52, 145], which is particularly important to our study. The key EDIP predictions are then further assessed with first-principles methods. The ART algorithm is combined with the KMC scheme in such a way that ART samples nearby saddle points of a local minimum to generate event lists with corresponding rates and the KMC algorithm executes an event according to these rates. This approach is referred as the k-ART and has been described in detail in Ref.[139]. It is worth pointing out that the original k-ART version proposed by Mousseau *et al.*[139] includes an additional topology analysis, which provides an additional speed up for calculations. This topology analysis is most beneficial when studying

multiple defects or considering an amorphous material with multiple different local environments. We did not implement this topology analysis because we are investigating one cluster defect at a time and the underlying lattice is crystalline. However, in order to boost the efficiency of ART in sampling nearby saddle points, we parallelize the code with the message passing interface (MPI) so that several processors work on each selected atom for a certain time and then report all generated events to a master processor to obtain the complete event list.

We performed a few k-ART simulations on the $(C_{BC})_3$ cluster at 1500 K and no migration is observed even after hundreds of thousand KMC steps (corresponding to 0.1 μs). This result implies that the migration barrier of the cluster is high. To activate the migration of the cluster on the timescale of the KMC simulations, we raise the simulation temperature to 5000 K. It is important to mention that this high temperature only affects the rate of events associated with cluster dynamics and, for example, it does not cause melting of SiC. The limited impact of the high temperature is because the crystal is relaxed to a local minimum in each KMC step, which effectively corresponds to modeling the crystal at 0 K. One problem with the high simulation temperature is that the cluster can dissociate as well as migrate in the KMC simulations. Since we want to isolate the migration from the dissociation of the cluster, in the KMC algorithm we apply a constraint so that dissociation effects are excluded. Dissociation events are identified as those where the largest distance between selected carbon atoms in the cluster and its nearest neighbor atoms is larger than one and a half lattice constants. We also apply a stopping criterion to stop the simulation when the system completes a migration or a rotation, which are identified as the system is in a state with energy difference from GS smaller than 0.25eV and with a displacement from the initial configuration larger than a specified threshold value. The displacement threshold can be set to be small (~4 Å) to find rotation pathways or to be large

(~6.5 Å) to force the cluster to migrate. With these modifications, k-ART can identify migration or rotation paths within few hundreds of KMC steps. Dissociation is considered separately later in Section 3.1.2.

The energy surface of paths predicted by k-ART is refined by density functional theory (DFT) calculations with the climbing image nudged elastic band (cNEB) method[123], as implemented in the Vienna Ab initio Simulation Package (VASP)[147]. The electron-ion interactions are described by the projector-augmented wave (PAW) method. We use PAW pseudopotentials with the valence electron configurations of 2s2, 2p2 for C and 3s2, 3p2 for Si. The cutoff energy for plane-wave basis sets is set at 500 eV. For Brillouin zone sampling, a 2×2×2 Monkhorst-Pack k-point mesh is used. We have tested the supercell size convergence on a cluster rotation barrier. We find that the error of the transition barrier within a 4×4×4 supercell (512 atoms) is converged to approximately 50 meV when compared with the barrier extrapolated at infinite size, while the error of the same transition barrier within a 3×3×3 supercell (216 atoms) is only converged to 0.12 eV. Therefore, a 4×4×4 supercell should be used when refining barriers predicted from EDIP. Considering the efficiency of DFT calculations, we first calculate the energy surface of each path with a 3×3×3 supercell, and then refine the transition step with the highest barrier in a 4×4×4 supercell. Jiang *et al.*[145] have shown that the $(C_{BC})_3$ structure is neutral for most values of the Fermi level, so we consider only neutral interstitials in all of our DFT calculations. By computing the quantum mechanical Hellmann-Feynman forces, all internal atomic positions are fully optimized using quasi-Newton method for CI-NEB images and conjugate gradient method for end points until forces are less than 0.02 eV/Å.

3.2 Low barrier paths to diffusion, rotation, and dissociation

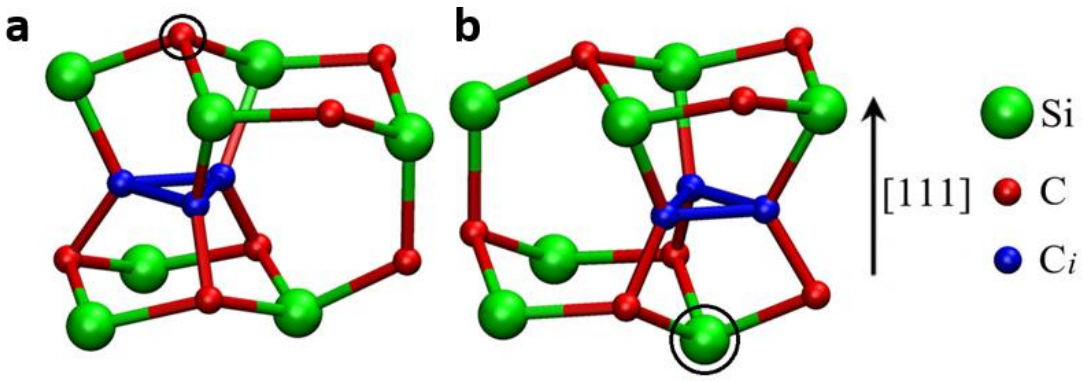

Figure 3-1 | Two possible cells in which the $(C_{BC})_3$ cluster can reside in cubic SiC. **a**, C-centered cell; **b**, Si–centered cell. The black circles label the centered C and Si atoms, respectively.

The two most stable configurations of the $(C_{BC})_3$ cluster in the cubic SiC are shown in Figure 3-1 and one can see that these clusters lie within the {111} planes. A C-centered (or Si-centered) cell refers to the cell where the lattice atom right above the center of the $(C_{BC})_3$ cluster is C (or Si). The C- and Si- centered cells are shown in Figure 3-1a and 3-1b, respectively. Jiang *et al*. 12 showed that the $(C_{BC})_3$ cluster within a C-centered cell is the GS of carbon tri-interstitial clusters in cubic SiC, and the energy of that within a Si-centered cell is 0.47 eV higher than GS in DFT, and 0.25 eV higher in EDIP. Thus, a stopping criterion of 0.25 eV within EDIP is sufficient to include both the C-centered and Si-centered structure. All of our k-ART simulations start from the C-centered structure. We define the rotation of the cluster as the movement from one {111} plane to another {111} plane but within the same C-centered cell, and migration as the movement from one C-centered cell to another C-centered cell either directly or through a Si-centered cell.

An example of energies calculated in a successful k-ART simulation as a function of the KMC step is shown in Figure 3-2a. The displacement from the initial configuration is calculated as

$$r = (\sum_{i=1}^{N} \Delta r_i^2)^{1/2} \quad (3\text{-}1)$$

where Δr_i is the displacement of atom i and N is the total number of atoms in the entire simulation box. The high simulation temperature drives the system to explore the potential energy surface aggressively by overcoming saddle points with energies up to 3 eV, which are unlikely to occur at low temperature simulations. We introduce a displacement threshold of 4.0 Å, which means that when the system is in a state with displacement from the initial C-centered structure larger than this threshold and with energy difference from GS less than 0.25eV, a migration of rotation path is completed and the simulations is stopped. The value of the displacement threshold has been varied during the sampling between 4.0 Å and 6.5 Å in order to force the cluster to move to different sites. For each successful simulation, we visualize the configurations along the identified path. In some cases, the system does not find the GS after thousands of KMC steps, and such simulations are labeled as failed since it yields neither a migration nor a rotation path. These failed simulations usually run into states with the relative energy higher than 8 eV because of the high simulation temperature. As shown in Figure 3-2b, we obtain 68 successful simulations out of the total of 131 simulations, and the 68 successful simulations yield 12 distinct migration paths and 4 distinct rotation paths. The number of distinct path starts at 7 because we have identified 7 paths when running tests on the codes. After finding no new paths for the last 45 successful simulations, the search is considered exhaustive. Subsequently all of the identified migration and rotation paths are refined by cNEB method based on DFT calculations.

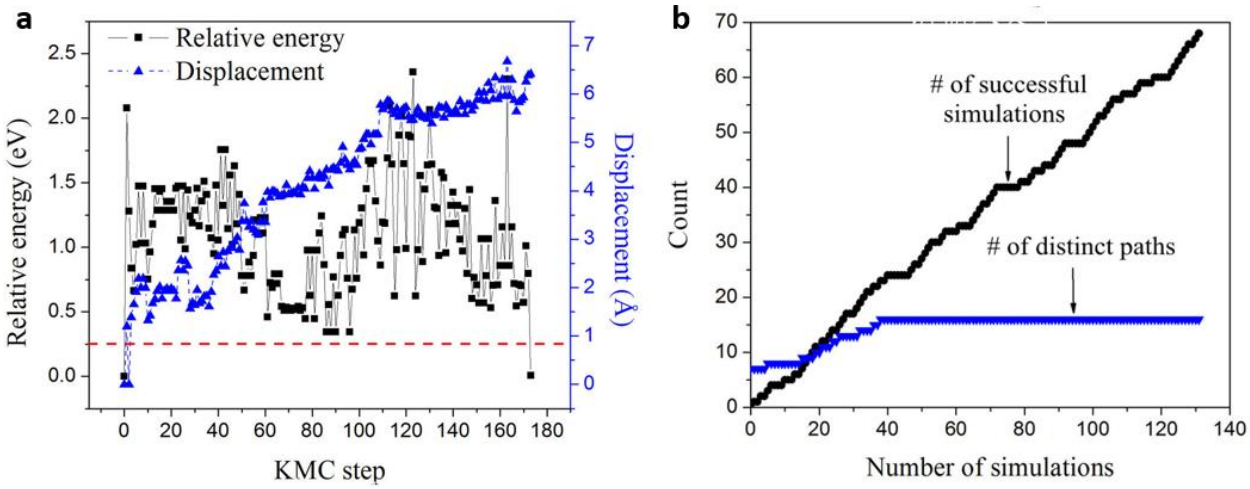

Figure 3-2 | **a**, Evolution of the energy and displacement from the initial C-centered configuration as a function of KMC steps in one successful k-ART simulation. The energy is calculated relatively to the initial configuration. The displacement is defined in Equation (3-1) in text. The horizontal dashed line (red online) represents the stopping criterion of 0.25 eV. **b**, The number of successful simulations and distinct paths identified from these successful simulations.

Table 3-1 | Energy barriers calculated with EDIP and DFT for the 12 migration paths identified with EDIP

Path ID	Energy barrier (eV)	
	EDIP	DFT
M1	4.12	4.29
M2A	3.09	5.26
M2B	4.53	5.26
M2C	5.42	5.24
M3A	3.03	5.40
M3B	3.47	5.40
M4A	3.22	4.77
M4B	4.13	7.51
M4C	3.04	5.31
M5	4.32	4.99
M6	2.84	4.37
M7	3.21	M4C

In Table 3-1, we show the energy barriers of the 12 distinct migration paths calculated within EDIP and DFT. A detailed description of the energy surface and intermediate configurations along each path shown in Table 3-1 can be found in Appendix A1 Figure S1-S9. The ID for each path is assigned according to their similarity in migration mechanism. For example, all paths with ID starting as M2 represent a process of rotation of the cluster in the original (111) plane. Path M7 turned out to be the same as path M4C after refining it with DFT calculations, so its barrier within DFT is labeled as M4C. Most of the barriers predicted by EDIP lie between 3.0 eV

and 4.5 eV, while the DFT refined barriers are in the range between 4.0 eV and 5.5 eV. Here we focus on the lowest barrier paths predicted by EDIP and refined by DFT.

As can be seen in Table 3-1, the path with the lowest migration barrier as determined from DFT is path M1 with the barrier of 4.29 eV in DFT and the barrier of 4.12 eV in EDIP. The energy surface along this path and intermediate configurations are shown in Figure 3-3. In this path, one interstitial first rotates around its nearest neighbor Si atom to form a dumbbell with the C lattice atom that used to occupy the position immediately above the $(C_{BC})_3$ cluster in its GS configuration (configuration α in Figure 3-3b). In the next step, the same C atom moves between the other two interstitials (configuration β) and enters the neighboring Si-centered cell (configuration γ). Finally, that C atom rotates around its nearest neighbor C lattice atom to recover the $(C_{BC})_3$ structure within a neighboring Si-centered cell in the original (111) plane. Along this path, the cluster moves from one C-centered cell to its neighboring Si-centered cell, and it can move to any neighboring C-centered cell from this Si-centered cell by inversing this path.

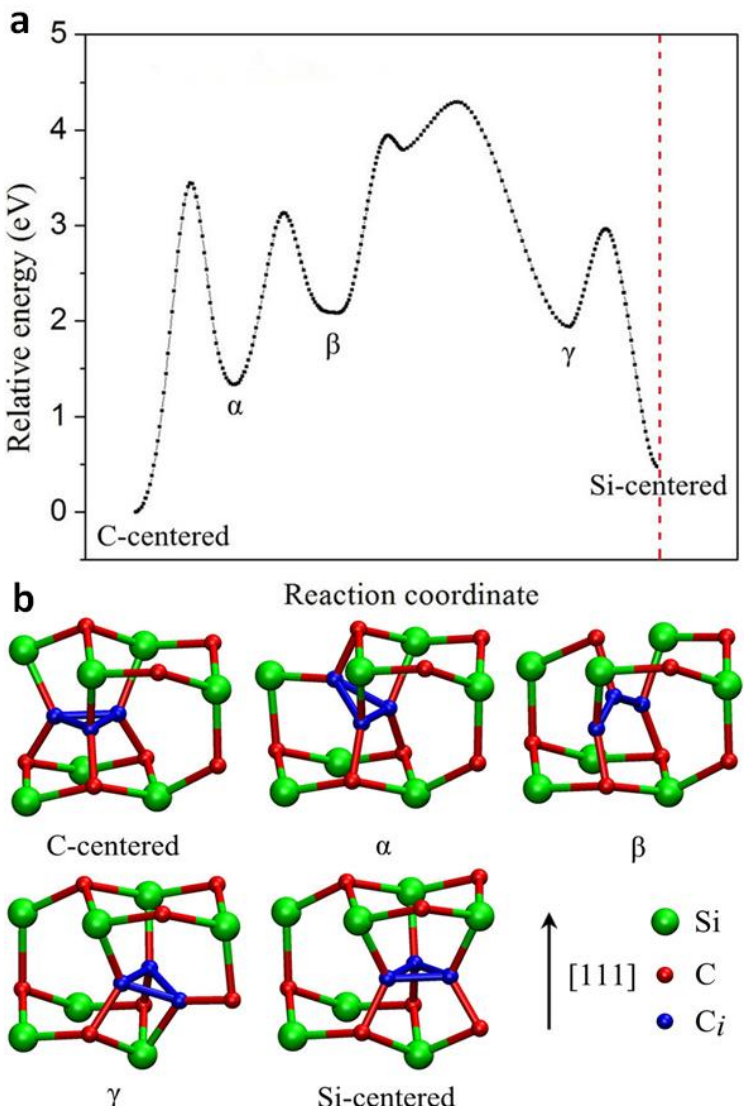

Figure 3-3 | **a**, Schematic view of the energy surface and of the intermediate states along path M1. The energy surface is symmetric with respect to the vertical dashed line (red online). **b**, Initial state, intermediate states α, β, γ and final state in this pathway.

It is instructive to discuss the M6 migration path, which was found to have the lowest migration barrier (2.84 eV) in EDIP. The corresponding barrier in DFT is 4.37 eV. The energy surface and intermediate configurations for this path are shown in Figure 3-4. In this path, one of the interstitial first rotates around its nearest neighbor Si lattice atom to form a C-C dumbbell with the C atom that used to occupy the center position above the cluster in its GS configuration

(configuration α in Figure 3-4b). In the next step (β), another interstitial rotates around its nearest neighbor C lattice atom, leaving the initially occupied C-Si bond center site vacant. This vacant C-Si bond center site is being simultaneously filled by the first C interstitial that moves towards it (γ). As a result, a tri-angular bonded structure composed of 3 C atoms at a C lattice site formed. In the next step (δ), one of the interstitials moves into a neighboring C-centered cell and thereby a chain of six C atoms is formed. The chain has C-C dumbbells at both ends and these dumbbells can rotate leading to a symmetry equivalent configuration (δ'). After that, the tri-angular bonded structure (γ') is formed again, this time in a new C-centered cell as the interstitial near the end of the chain moves from the original C-centered cell to the new cell. Since γ' and C-centered' are symmetry equivalent to γ and C-centered GS, respectively, the cluster can transform from γ' to C-centered' by reversing the pathway from C-centered to γ, as described above. Following this path, a C lattice atom is pushed to the bond center site while the vacant lattice site is now filled by an initial C interstitial.

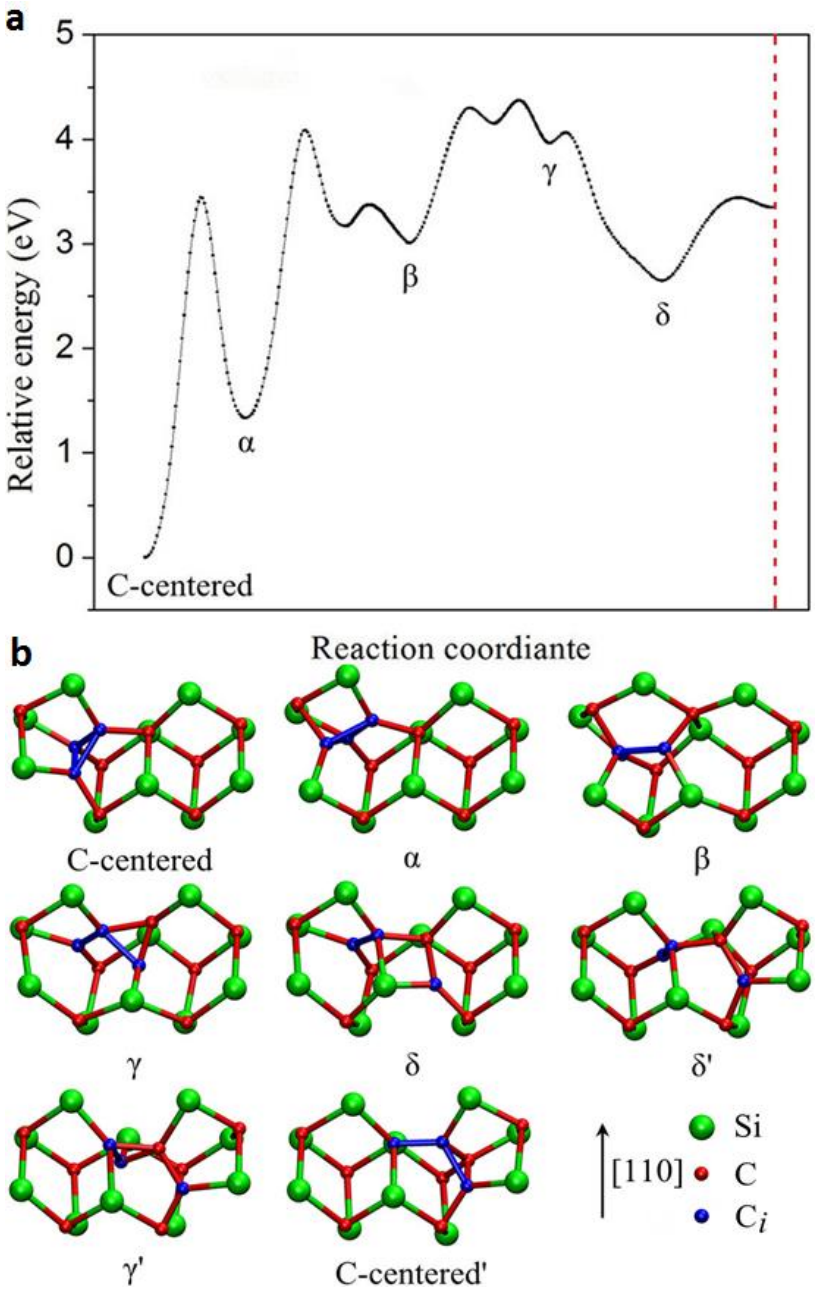

Figure 3-4 | a, Schematic view of the energy surface and of the intermediate states along path M6. The energy surface is symmetric with respect to the vertical dashed line (red online). **b**, Initial state, intermediate states α, β, γ, δ, and final state in this pathway. γ', δ' and C-centered' are symmetry equivalent configurations of γ, δ and C-centered GS, respectively, in another C-centered cell. Only the three initial C interstitials are labeled as blue sphere.

We define dissociation as the process during which the $(C_{BC})_3$ cluster breaks into two non-interacting defects: a single C interstitial and a C di-interstitial defect. The final configuration of the single C interstitial is chosen to be the C split interstitial in the tilted <100> configuration (Csp<100>). The final state of the C di-interstitial defect is $(C_{BC})_2$, where two C interstitials occupy neighboring C-Si bond center sites in (111) plane. These two final structures are chosen because they are the most stable configurations for the respective defects in cubic SiC[52]. In fact, $(C_{BC})_3$ and $(C_{BC})_2$ share the same bond center bonding structure with the only difference that $(C_{BC})_3$ is composed of 3 bond centers bonding to each other while $(C_{BC})_2$ composed of only 2 bond centers. This implies that the dissociation is a process that one C interstitial in $(C_{BC})_3$ breaks bonds with the other two and migrates away until there is no interaction between it and the $(C_{BC})_2$ left behind. The energy of the final dissociate state can be calculated by summing up formation energies of the non-interacting constituents and it is equal to 4.36 eV. The high symmetry of $(C_{BC})_3$ limits the number of possible dissociation pathways to a few, and after calculating them with DFT, we determined the lowest dissociation barrier as 4.83 eV, as shown in Figure 3-5. Along this pathway, one of the interstitial in $(C_{BC})_3$ first breaks bonds with the other two and then migrates away from the $(C_{BC})_2$ by C-C/C-Si dumbbell transition mechanism, as suggested in Ref. 32. Note that along this pathway, the relative energy visits the 4.36 eV state twice, however, we take the higher barrier (4.83 eV) which leads to the second 4.36 eV state as dissociation barrier. This barrier relative to the dissociation state is 0.47 eV, which agrees with the 0.5 eV migration barrier of a single Csp<100>, and this implies there is no interaction between Csp<100> and$(C_{BC})_3$. This is not true for the first 4.36 eV state where the migration barrier of the Csp<100> is lowered due to the interaction between the two defects.

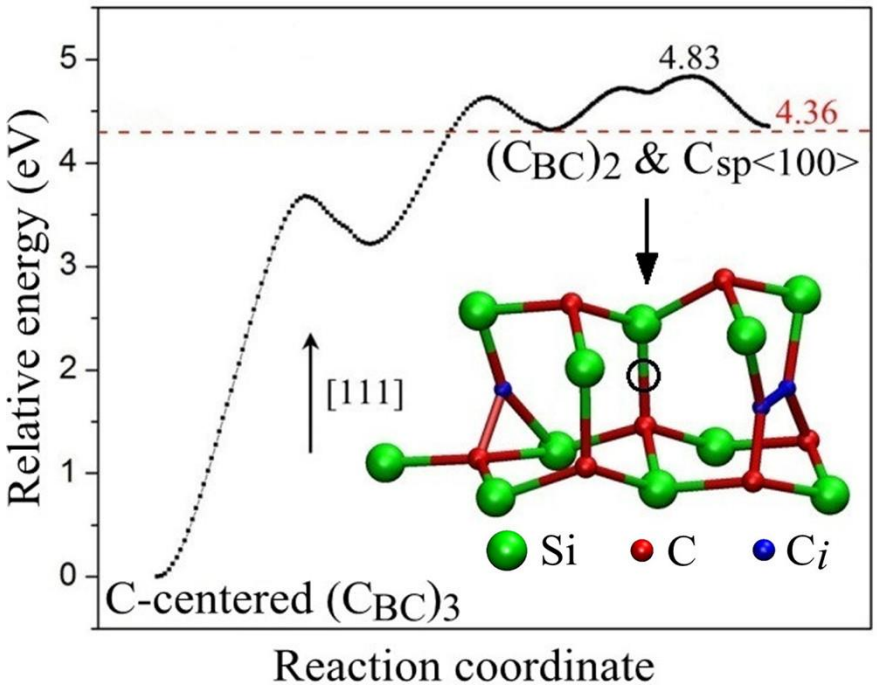

Figure 3-5 | The energy surface for the dissociation of the $(C_{BC})_3$ cluster. The dashed horizontal line (red online) at 4.36 eV represents the relative energy of not-interacting $(C_{BC})_2$ defect and $C_{sp<100>}$. The embedded structure represents the final configuration, where the solid circle represents the initial bond center site occupied by the $C_{sp<100>}$.

As can be seen in Table 3-2, the discrepancy in energy barriers for rotation paths between EDIP and DFT is also non-negligible. However, the actual rotation path corresponding to the lowest energy barrier predicted by EDIP (with the energy barrier of 1.84 eV) agrees with the lowest path predicted after DFT refinement (with the energy barrier of 4.14 eV). The energy surface and intermediate states of the lowest barrier path are shown in Figure 3-6a. In this pathway, one C interstitial first rotates around its nearest neighbor Si lattice atom to form a C-C dumbbell with the C lattice atom (configuration α in Figure 3-6b), which used to occupy the center position right above the $(C_{BC})_3$ cluster in its GS. Next, another C interstitial rotates around its nearest neighbor C lattice atom and moves to the (111) plane that is already occupied by the

first interstitial (configuration β). Finally, the last C interstitial moves to the same (111) plane by rotating around its nearest neighbor C lattice atom and the GS $(C_{BC})_3$ structure is recovered.

With a transition barrier of 4.14 eV, the rotation of the $(C_{BC})_3$ cluster between (111) planes can barely happen at temperatures below 1100 K (less than 1 hop rate per month). This implies that once the $(C_{BC})_3$ cluster is formed on a certain (111) plane, it can grow into larger clusters on the same (111) plane, consistently with the idea that this cluster is an aggregation center for interstitials. Rotation of the cluster can be activated at elevated temperatures with a rate comparable to that of migration (the lowest barrier to migration is 4.29 eV).

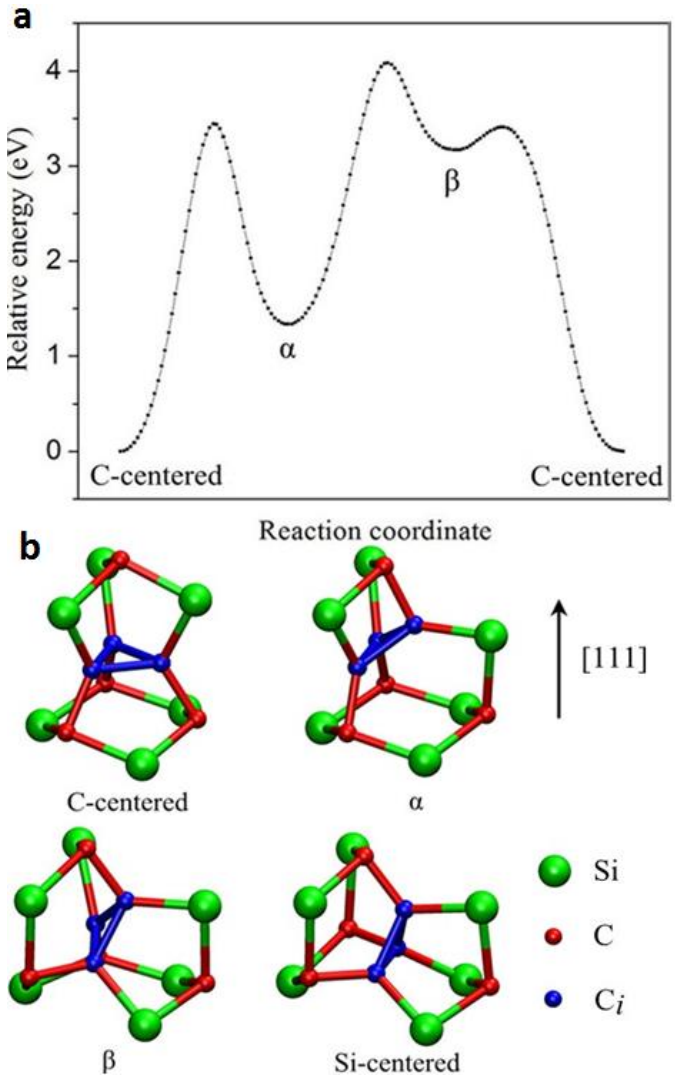

Figure 3-6 | Schematic view of the energy surface and of the intermediate states of the rotation path R1. α and β are intermediate local minima along the pathway.

Table 3-2 | Energy barriers of the 4 rotation paths found in EDIP and calculated within EDIP and DFT.

Path ID	Energy barrier (eV)	
	EDIP	DFT
R1	1.84	4.14
R2	4.13	6.82
R3	3.52	R1
R4	3.72	5.70

3.1 Diffusivity of interstitial clusters in SiC

Given the above migration and dissociation barriers, the $(C_{BC})_3$ cluster can be viewed as immobile and stable at temperatures below 1100 K, where neither migration nor dissociation can take place on long-time scale (hop rate < 1 month-1). The hop rate is calculated by using the following equation,

$$\Gamma = \nu e^{(-E_a/kT)} \tag{3-2}$$

where Γ is the hop rate, ν is the attempt frequency approximated as 5×10^{12} s^{-1}, E_a is either the migration or dissociation barrier, k is the Boltzmann constant, and T is the absolute temperature. Therefore, in the low temperature regime (T < 1100 K) this defect is likely to serve as aggregation center for interstitials that then grow into larger clusters or planar defects as proposed by Jiang *et al.*[52]. It is also interesting to consider the long term evolution of the $(C_{BC})_3$ defect at higher temperatures in typical annealing experiments (over 1300 K). We define a critical temperature of dissociation as the temperature at which dissociation can take place once within the time of typical annealing experiment (~1 hr[59]). To estimate this temperature, we use

Equation (3-2) and set Γ, the dissociation rate, to be once per the experimental time of 1hr. The critical temperature of dissociation is then calculated as 1500 K based on the barrier of E_a = 4.83 eV. This analysis implies that, at temperatures below 1500 K, annealing of $(C_{BC})_3$ defects will be dominated by their migration whereas dissociation begins to be dominate at temperatures higher than 1500 K. It is useful to quantify the mobility of the $(C_{BC})_3$ cluster in the regime where mobility dominates the annealing. To do that, we calculate the mean diffusion distance x for the experimental time scale τ = 1 hr at a given temperature T = 1500 K using the following equation

$$D = \frac{x^2}{2d\tau} = a^2 ve^{(-E_m/kT)} \tag{3-3}$$

where D is the diffusion coefficient, d is the dimensionality of the system, a is the hop distance, E_m is the migration barrier. The dimensionality d is taken as 3 because the rotation of the cluster among different (111) planes (discussed later in this section) can be activated at 1500 K. The hop distance a is taken as the displacement of the center of mass of the $(C_{BC})_3$ defect in a migration between two neighboring C-centered cells following path M1, and is calculated as 3.1 Å. Migration barrier E_m is taken as 4.29 eV, the lowest barrier of migration path (M1). This analysis predicts the mean diffusion distance x ≈ 6.3 nm, which is much smaller than the grain size of typical experimental SiC samples. Therefore, the mobility of the $(C_{BC})_3$ cluster is very low even at 1500 K, and cannot be easily annealed out by diffusion to sinks alone.

Table 3-3 | Binding energies and approximated dissociation barriers of the GS of small carbon interstitial clusters with size up to 6. Binding energy is taken from Ref.[52]. $(C_{BC})_{3,C}$ represents a $(C_{BC})_3$ structure in the C-centered cell, and $(C_{BC})_{3,Si}$ represents a $(C_{BC})_3$ structure in the Si-centered cell.

Size	Structure	E_b(eV)	$E_{dissociation}$(eV)
2	$(C_{BC})_2$	5.16	5.66
3	$(C_{BC})_{3,C}$	9.52	4.86
4	$(C_{sp})_4$	12.37	3.35
5	$(C_{BC})_{3,C}+(C_{BC})_2$	16.12	4.25
6	$(C_{BC})_{3,C}+(C_{BC})_{3,Si}$	19.46	3.84

Because the $(C_{BC})_3$ structure is a common build block of small carbon interstitial clusters in cubic SiC[52], based on the knowledge of its mobility and stability, a reasonable guess on the kinetics of small carbon interstitial clusters can be made. First, we assume the migration barrier of small carbon interstitial clusters is comparable to the migration energy barrier of 4.29 eV found for the $(C_{BC})_3$ cluster. Secondly, we approximate the dissociation barrier with the following equation

$$E_{dissociation}(\mathrm{n}) = E_b(n) - E_b(n-1) + E_{M,Ci} \tag{3-4}$$

where $E_b(n)$ is the binding energy of carbon n-interstitial cluster, defined as the energy difference between a carbon n-interstitial cluster and n non-interacting $C_{sp<100>}$, and $E_{M,Ci}$ is the migration barrier of a single C interstitial taken as 0.5 eV, based on Ref.[46, 75]. In Table 3-3, we show the binding energies of small carbon interstitial clusters with a size of up to 6 and their approximated

dissociation barriers. For clusters with size over 3, the dissociation barrier is around 4 eV, which is comparable to or even lower than the cluster migration barriers. Therefore, in high temperature annealing, small carbon interstitial clusters will likely dissociate into smaller clusters by emitting interstitials one by one with limited or no diffusion of the clusters themselves. It would be safe to assume that small carbon interstitial clusters with sizes equal to or larger than 3 in cubic SiC are immobile in long-time scale modeling of defect evolution, such as cluster dynamics model. However, one exception is the $(C_{BC})_2$ defect, the dissociation barrier of which is approximated as 5.66 eV. Since the migration barrier of this defect is not higher than 4.29 eV, it is diffusive at temperatures below the critical dissociation temperature and therefore the dynamics of $(C_{BC})_2$ defect should be carefully treated in long-time scale simulations.

Based on the good agreement between calculated and experimental LVMs, Jiang *et al.*[145] proposed that the $(C_{BC})_3$ cluster as a candidate for the DII center in SiC, which has been found in photoluminescence experiments[60, 62, 148-149]. Up to this point, the $(C_{BC})_3$ cluster was found to be the only candidate that produces 5 LVMs in the cubic SiC and 10 LVMs in the hexagonal SiC, in agreement with experiments, and one that provides the best (although not excellent) quantitative agreement with the LVMs. These findings support the idea that the $(C_{BC})_2$ cluster is responsible for the experimentally observed DII center. We are now in the position to ask if the thermodynamic stability of $(C_{BC})_3$ is consistent with some experimental studies[60-62] that found that the defect responsible for the DII center can persist even after annealing at 1973 K. Our calculated migration and dissociation energies of $(C_{BC})_3$ are inconsistent with this proposal. This inconsistence may arise from multiple factors. First of all, there are limited details on experiments reported in literature, which makes the comparison somewhat qualitative. So far, only one paper from year 1973[60] reported the persistence of DII center up to 1973 K in cubic SiC

and this paper gives very little details on the doping conditions, temperature fluctuation and annealing time. Other papers[61-62] that reported the persistence of DII center up to 1973 K were based on experiments conducted with hexagonal (4H) SiC samples, which may possibly change the dissociation barrier. To make comparison to experiments conducted with 4H-SiC samples, we calculate the dissociation energy of the $(C_{BC})_3$ cluster in 4H-SiC and approximate the dissociation barrier by adding the migration barrier (0.5 eV) to the dissociation energy. The approximated dissociation barrier is 5.0 eV, which is still not high enough for the defect to survive during 1973 K annealing (hop rate is ~1 s-1). Another possibility to explain the lack of stability of $(C_{BC})_3$ at 1973 K is that this cluster is stabilized against annealing by binding to another defect, such as an antisite or Si interstitial. It is also possible that the defects responsible for the DII center form other configurations that are derived from the three-bond center structure as in the $(C_{BC})_3$ cluster, for example by forming larger clusters that grew by incorporating Si interstitials. Such structure might share similar LVMs and stability with the $(C_{BC})_3$ but have a high barrier to dissociation. Finally, it is possible that the $(C_{BC})_3$ cluster is reassembled in the experimental samples when they are quenched from high temperature to 0 K, at which the photoluminescence tests were conducted. The high mobility of C interstitial increases the probability that point defects find each other and are stabilized as $(C_{BC})_3$ during quenching below the dissociation temperature.

In summary, by using a combination of k-ART sampling with EDIP and ab initio based CI-NEB calculations, we have determined the migration and dissociation energies of the $(C_{BC})_3$ cluster in cubic SiC, which is the most stable small C interstitial clusters in SiC among the known clusters in SiC. The fastest migration path has the energy barrier of 4.29 eV and the second fastest path has a comparable barrier of 4.37 eV. The dissociation barrier of the $(C_{BC})_3$

cluster into a non-interacting $(C_{BC})_2$ defect and Csp<100> is 4.83 eV and the rotation barrier of the cluster moving between different (111) planes is found to be 4.14 eV. The mobility of the $(C_{BC})_3$ cluster is limited up to temperatures of ~1500 K, and thus this cluster can be treated approximately as immobile. The $(C_{BC})_3$ cluster was found to dissociate as temperature above 1500 K and it is predicted that this is the pathway by which it can be annealed out from the crystal, rather than through diffusion to a sink. Since the $(C_{BC})_3$ structure is a common building block of small carbon interstitial clusters, it is reasonable to assume their lack of mobility in long-time scale modeling such as cluster dynamics. An interesting direction for the future study will be the effects of applied stress on the rotation of small clusters and large dislocation loops in SiC, since it had been proposed that rotation of such defects and the resulting anisotropic distribution of dislocation loops with respect to the stress axis are responsible for irradiation swelling and creep in SiC[45, 68].

Chapter 4 Defect Clusters in SiC: Radiation Induced Diffusion*

By implementing the on-the-fly KMC model, we showed that the barrier to migration of clusters as small as just three C interstitials is ~4.3 eV, which means that these clusters are immobile on typical experimental annealing time scales (i.e., 1 hour whereas the cluster performs less than 1 hop/day), or at light water reactor operation temperatures. As discussed in Section 1.4.2, in addition to thermal diffusion, it is found that defects can diffuse athermally under the influence of radiation environments. It is of great interest to explore whether energetic radiation species can drive cluster diffusion in SiC. If radiation induced diffusivity of clusters in SiC is high enough to drive cluster coalescence or diffusion to sinks, this can significantly advance understanding of long-term evolution of defects and microstructures of SiC under irradiation. In this section, I report a direct observation of interstitial clusters diffusion in bulk SiC under the influence of electron radiation at room temperature. Dr. Li He conducted all the electron transmission microscopy works, and I was responsible for experimental data analysis, modeling, and writing up the paper.

4.1 Electron microscopy observation of cluster diffusion

In our experiments, 4H-SiC sample was first irradiated by 1 MeV Kr at 600°C at a flux of 2.5×10^{12} atoms/(cm^2s) to a dose of 3×10^{14} Kr atoms/cm^2, 4° off the [0001] direction, producing a peak damage of 0.4 displacement per atom (dpa) at 0.3 μm depth, as estimated using the Stopping and Range of Ions in Matter software[150]. STEM samples were prepared by wedge polishing and argon ion milling with beam energy of 3.5 keV first, then 2 keV, and finally 0.5

keV. Subsequently electron irradiation was conducted at the depth corresponding to 0.26 dpa at room temperature under 200 kV with a FEI Titan S-Twin, and under 60 kV with a FEI Titan G2 60-300, both of aberration corrected STEM. The electron flux for 200 keV irradiation is in the range of 2.58×10^5 – 4.05×10^6 $e^-/(nm^2s)$, and for 60 keV irradiation is 2.22×10^5 – 1.99×10^7 $e^-/(nm^2s)$. For a pixel size r much smaller than the probe size, the electron dose per frame is $d = ct / r^2$ for pixel dwell time t, where c is the beam current in e^-/s. We adjusted the flux primarily by changing the STEM pixel size and the probe current. Low angle annular dark field (LAADF) image series, were taken with 200 keV beam of semi-convergence angle 17.5 mrad, collection angle 23.0 - 115 mrad, or 60 keV beam of semi-convergence angle 25.1 mrad, collection angle 29.0 - 145 mrad, in 0.95 s per frame for 128 frames. Sample drift and instrumental instabilities were removed from the image series using non-rigid registration[151]. The majority of results reported here correspond to 200 keV, but 60 keV experiments were also conducted to test our hypotheses regarding the mechanisms underlying radiation-induced diffusion.

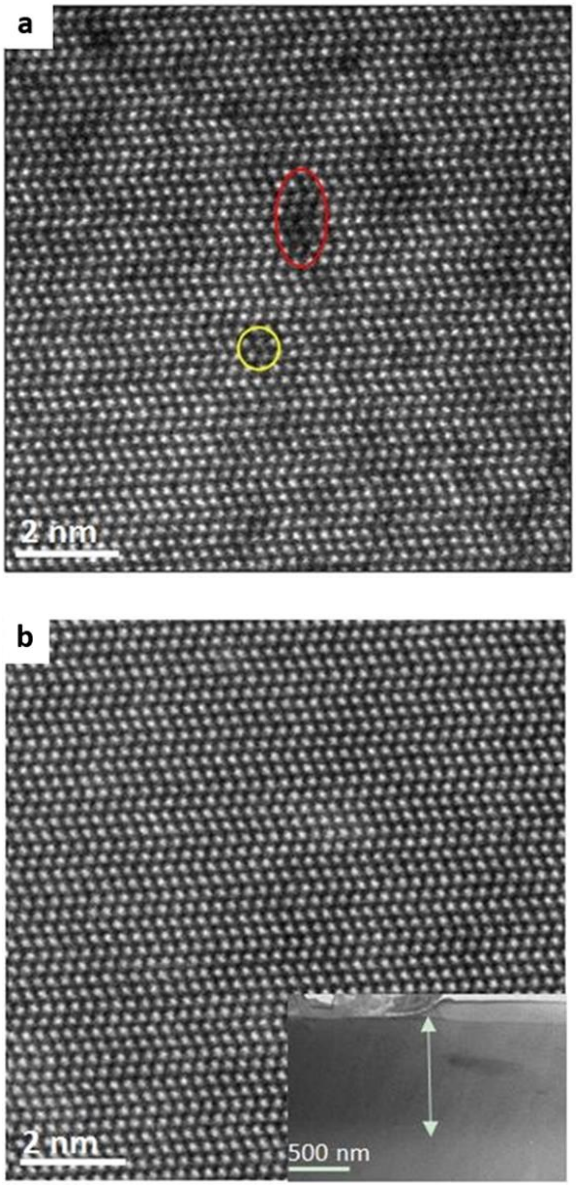

Figure 4-1 | **a**, LAADF STEM image from the ion damaged region acquired with semi-convergence angle 17.5 mrad and collection angle 17.5 - 34 mrad shows defects induced strain contrast. Two example clusters have been circled; **b** HAADF STEM image of the same area as in (a) acquired with a beam semi-convergence angle 24.5 mrad and collection angle 54 - 270 mrad. The inset is a TEM bright field image with the viewing direction along $<11\bar{2}0>$. The arrow shows the ion damaged surface region. Both high-resolution images have been convolved with a 0.5 Å standard deviation Gaussian filter to reduce noise.

Figure 4-1 shows a low-angle annular dark-field (LAADF) (detector covering 17.5 to 34 mrad) STEM image of Kr-irradiated 4H-SiC. The irregular dark blobs, each of which covers a few atomic columns, are irradiation-induced defect clusters, visible due to their strain fields, which are emphasized in LAADF imaging[152]. Figure 4-1b is a high-angle ADF (HAADF) (detector covering 54 to 270 mrad) image of the same region of the same sample. The lack of contrast confirms that the contrast ascribed to defect clusters does not arise from other sources such as surface roughness, oxidation, or hydrocarbon contamination. The average cluster diameter was found to be 0.85 ± 0.01 nm (corresponding to no more than 15 point defects shown in Appendix A2) and the cluster density was found to be $(9.3 \pm 0.8) \times 10^{23}$ m^{-3}. These clusters are believed to be of interstitial-type because of the lack of vacancy mobility in this temperature regime [71].

In the experiments performed under 200 keV electron irradiation, many of the defect clusters are found to be mobile. One example is illustrated in Figure 4-2, where a defect cluster is shown to move over a series of LAADF STEM images (see also video S1 in Appendix A2). The images in the series were aligned using our recently developed non-rigid registration technique[151], which separates instrumental effects (drift and instability) from the actual motion of defects. Averaging of similarly aligned series has demonstrated sub-pm precision in locating atomic positions[151]. Here, it renders the underlying crystal lattice motionless, making the motion of the defect clusters visible to the human eye and amenable to quantitative analysis. Three more examples of aligned STEM image series are available in videos S2-S4 in Appendix A2.

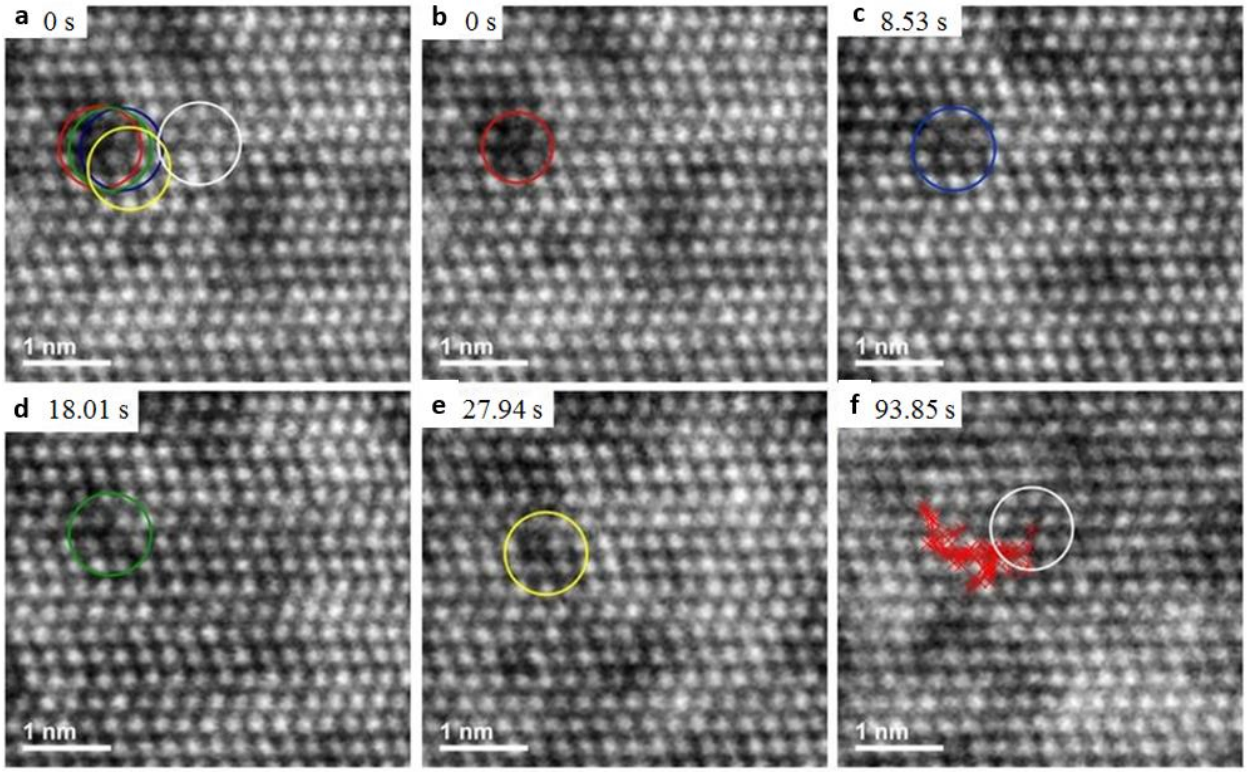

Figure 4-2 | Defect trajectory in an aligned STEM image series under 4.05×10^6 e^-/nm^2s 200 keV electron radiation. **a**, The first image in the trajectory with the defect positions in the later images superimposed; **b-e**, Snapshots of the defect position as a function of time; **f**, The defect position at the end of the trajectory (white circle) and the entire trajectory (red symbols). Squared displacements were calculated from trajectories like **f**. The entire trajectory is available as video S1 in Appendix A2. Images were convolved with a 0.5 Å standard deviation Gaussian filter to reduce noise.

In Figure 4-2a, the cluster has moved from the position marked with a red circle to one marked by a white circle within the time of 94 s. For these mobile defect clusters, we track the position of the center of the clusters in non-rigid registration aligned STEM images frame by frame (details of tracking procedure are described in Appendix A2), and the trajectory of the cluster in Figure 4-2a is shown in Figs. 3-8b to 3-8f. We then calculate the squared displacement

Δr^2 of each cluster from its starting position as a function of tracking time t. Δr^2 is subsequently used to determine the diffusion coefficient D

$$D = \frac{\Delta r(t)^2}{2dt}, \tag{4-1}$$

where d is the dimensionality of the motion (here d = 3). Figure 4-3a shows Δr^2 vs t of the mobile defects illustrated in Figure 4-2; in Figure 4-3a the slope of the fitted line is $2d \times D$. In Figure 4-2bb, we report averages of diffusion coefficients determined for different fluxes of 200 keV electrons from the trajectories of multiple defects. In general, diffusivity increases with increasing electron flux. Detailed information on trajectories and diffusion coefficients for each mobile defect under 200 keV is reported in Table S1 in Appendix A2. In contrast to the 200 keV experiments, within the experimental time scale (~10^2 s), we did not observe significant displacements of clusters under 60 keV electron radiation even at a high flux of 1.99×10^7 $e^-/(nm^2s)$. This does not imply the diffusion coefficient of clusters under 60 keV radiations is necessarily zero, instead, it suggests the diffusion coefficient is too small to identify observable displacements within the experimentally accessible time scale. By assuming the un-observable displacement is less than the radius of the average cluster size (~0.42 nm), the un-observable diffusion coefficient range within the experimental time scale is calculated as $(0–3)\times10^{-4}$ nm^2/s by using Equation (4-1). This range is significantly lower than diffusion coefficients of clusters induced by 200 keV electron irradiation.

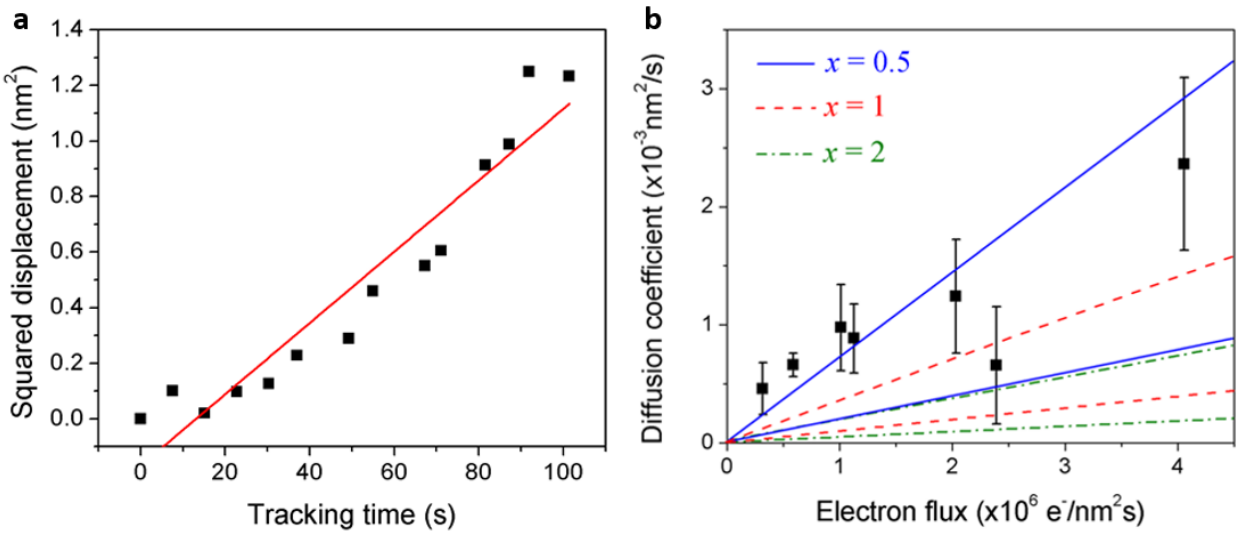

Figure 4-3 | **a**, Mean square displacement (symbols) of the defect circled in Figure 3-8 and a linear fit to the data; **b** Diffusion coefficients of mobile defect clusters measured at different fluxes under 200 keV electron beam. Each point represents the average over 3-5 mobile defects and the error bar is calculated as a standard deviation. Solid (blue), dashed (red), and dashed-dotted (green) lines indicate the upper and lower limits of diffusion coefficient predicted by the model using different values of x, where $x = N_{step}/N_{atom}$ as explained in text.

4.2 Verification of the diffusion mechanism

What is the mechanism responsible for the radiation-induced diffusion of clusters in SiC? One possibility, which has been often invoked to explain effects of radiation on accelerating point defect diffusion in ceramics, is that ionization of defects can lower their migration barriers. This phenomenon has been reported for instance in $MgAl_2O_4$[153] and Al_2O_3[153-154]. Ionization was also invoked to explain local bond-switching and recovery of a damaged zone (without diffusion and mass transport) in SiC[47, 155]. However, ionization cannot explain our results: the ionization cross section for 60 keV electrons is higher than for 200 keV electrons[156], but the diffusivity is substantially lower. Here, we propose that radiation-induced diffusion of otherwise immobile

interstitial clusters in SiC is a result of ballistic collision of incoming electrons with cluster atoms. During such collision, kinetic energy is transferred from the high-energy electron beam to interstitial atoms, assisting them in overcoming the energy barrier to migration athermally. A similar mechanism had been previously proposed for radiation effects on vacancy diffusion in lead[87] and more recently also for defect transformation and migration on surfaces[91] and in mono-layer graphene[88-90, 157]. However, until now radiation-induced diffusion of defect clusters in bulk had not been demonstrated. This mechanism is consistent with our observation that decreasing the energy of the electron beam lowers the mobility of clusters because the electron-beam-induced atomic displacement cross section decreases as electron energy decreases[158]. In order to further demonstrate that ballistic collision can explain trends observed in our experimental data, we build a model of radiation-induced diffusion, which model relies on elastic electron-nucleus collision of the radiation beam with cluster atoms.

As shown in Ref.[159] and Figure S13 in Appendix A2, a ground-state to ground-state migration of a cluster involves multiple steps. The multi-step nature of the migration process is further confirmed by our *ab initio* MD simulations of diffusion of a carbon tri-interstitial cluster (Appendix A2). In our radiation-induced diffusion model, we assume the cluster can perform a single step when it receives from energetic electrons an energy E_T higher than a threshold energy E_{th}. This step might involve migrating one or more atoms at a time. The property E_{th} here is different from the widely known threshold displacement energy[160], where the latter one is the minimum energy received by a lattice atom to be displaced into an interstitial site. Here E_{th} is defined as the minimum energy received by cluster atoms to activate cluster diffusion and is assumed to be the same for all atoms in the cluster. The rate of steps J induced by electron radiation can be estimated as $\Phi \times \sigma_{th} \times N_{atom}$. In this equation Φ is the electron flux, σ_{th} is the

electron-beam-induced displacement cross section for $E_T > E_{th}$, and N_{atom} is the number of atoms participating in the diffusion process of the cluster (N_{atom} is included in the estimate of J as we assume a step can be induced whenever any atom in the cluster receives $E_T > E_{th}$). Assuming that the number of steps to complete a migration between symmetry equivalent sites is N_{step}, the diffusion coefficient can be written as

$$D = \frac{a^2}{2d} \cdot \frac{J}{N_{step}} = \frac{a^2}{2d} \cdot \frac{\Phi \sigma_{th} N_{atom}}{N_{step}} = \frac{a^2}{2d} \cdot \frac{\Phi \sigma_{th}}{x}, \quad (4\text{-}2)$$

where d has the same meaning as in Equation (4-1), a is the migration distance between neighboring symmetry equivalent sites (~0.3 nm), and x is the ratio of N_{step} to N_{atom}. A reasonable range of values for the ratio x is 0.5–2.0[52, 159, 161] (also see Appendix A2). At the sample surface the electron flux Φ_0 is known, but dynamical diffraction of the electron wave in the crystal along the zone axis modulates the flux Φ as a function of sample thickness. Using a multislice simulation of electron beam in 4H-SiC we found that Φ can vary between 0.4 Φ_0 and 1.4 Φ_0 throughout the sample's depth (details in Appendix A2). As a cluster can exist at any depth, these minimum and maximum values of Φ are used to determine the lower and upper limits of the diffusion coefficient D.

In order to estimate E_{th} we use the fact that in our experiments there is no observable displacement of clusters under 60 keV even at high electron flux. As shown earlier, the absence of observed diffusion implies the clusters have a diffusion coefficient smaller than $D = 3\times10^{-4}$ nm^2/s. Combining this value with $\Phi = 1.99\times10^7$ e$^-$/nm^{2}s (the maximum flux in the sample under 60 keV electron beam) and Equation (4-1), one can estimate the lower limit of the threshold energy E_{th} to be 10.7 eV. This value of E_{th} is 2-3 times the typical migration barrier of small carbon interstitial clusters reported in literature (4.3–7.5 eV)[159]. This result is intuitive as the

momentum transferred from the high-energy electron to a cluster atom will generally not align along the path of minimum migration energy for the excited step, yielding E_{th} values significantly higher than typical migration energies.

Using the value of E_{th} = 10.7 eV estimated from 60 keV experiments, we can now calculate the diffusion coefficient D of clusters under 200 keV electron radiation. The results are shown as a function of the electron flux Φ in Figure 4-3b. For each value of x the straight lines represent the maximum and minimum values of D determined assuming $\Phi = 1.4\Phi_0$ and $\Phi = 0.4\Phi_0$, respectively. The diffusion coefficients predicted by the model are on the same order of magnitude as the ones measured experimentally, and a quantitative agreement can be reached for reasonable and physically-justifiable parameters of the model. Furthermore, the model predicts a linear increase of diffusivity with electron flux, similar to that seen in experimental data in Figure 3-9b, although within the error bars of the experimental data it is not obvious whether the trend is also linear. Finally, our model predicts that reducing the beam energy will lower D, since the electron-beam-induced atomic displacement cross-section σ_{th} decreases monotonically with decreasing energy[158] and since D is proportional to σ_{th} in Equation (4-2). This prediction is again consistent with our experimental observation that diffusion coefficient for 60 keV electrons is significantly lower than for the case of 200 keV electrons. The results of the model strongly support our hypothesis that ballistic collision is the mechanism controlling experimentally observed radiation-induced mobility of self-interstitial clusters in SiC. A more quantitative analysis of diffusion coefficients would require performing experiments under other electron irradiation conditions, which are challenging to carry out in TEM. Nevertheless our experiments provide sufficient evidence for the ballistic collision mechanism proposed for the observed diffusion of defect clusters.

4.3 Discussions and implications

The combined results of STEM, *ab initio* MD simulations and electron beam-cluster collision model demonstrate that small interstitial clusters in SiC can become mobile under irradiation – contrary to what had been previously assumed. Based on the results of our 200 keV electron radiation experiments, the radiation-induced diffusion distance of these clusters is on the order of nanometers over hundreds of seconds. The distance can be larger if the materials are under radiation for longer times such as in the service of nuclear reactors. Such an enhanced mobility of clusters can potentially affect local defect dynamics including coalescence of neighboring clusters, recombination between clusters and vacancies as well as annealing of clusters at nearby sinks. Such processes can play a role in defect evolution in irradiated or ion-implanted materials because they impact the rate of damage accumulation and thereby also multiple properties of these materials relevant for their applications. The phenomenon of radiation induced diffusion of clusters has been considered in a recent study to interpret experimentally measured black spot defect size and density in irradiated SiC. By including radiation induced diffusivity of defect clusters in a cluster dynamics model, this study correctly reproduced the cluster size and density in Kr irradiated SiC[162].

Although it is known that in metals radiation can lead to the one-dimensional diffusion of interstitial loops along the glide direction[163-165], the underlying mechanism is entirely different from the one discussed here. Unlike in ceramics, in metals interstitial loops have inherently relatively low migration barriers (on the order of 0.02 eV[166]) and therefore they are mobile at room temperature. These otherwise mobile loops can become trapped by pinning points, such as solute atoms, and the role of radiation is to release the loops from traps[165]. Thus in this case radiation is not the driving force for defect migration, but rather it allows interstitial loops to

undergo thermal diffusion that would occur in the absence of trapping solutes. The situation is qualitatively different when it comes to ceramics where it is generally accepted that clusters of self-interstitials or vacancies are immobile at room temperature due to their high inherent migration barriers (typically between 4 and 7 eV[159, 167-168]). Therefore, the observed diffusion of clusters in SiC is an athermal process induced by radiation, rather than triggered by radiation. . Nevertheless our experiments provide sufficient evidence for the ballistic collision mechanism proposed for the observed diffusion of defect clusters.

Based on the results of this study, it is also possible that one could use electron beam to anneal out undesirable interstitial clusters, which otherwise are known to persist even at high annealing temperatures[169]. While our measurements were carried out on SiC (a materials in itself important for many technological applications), we expect that similar behavior can be observed in other covalent or ionic-covalent materials if high resolution imagining techniques are used to monitor defect kinetics.

Chapter 5 Tilt Grain Boundaries as Defect Sinks in SiC*

It is known that interfaces, such as GBs, can act as defect sinks[93, 105, 170]. However, the questions of how GBs accommodate these defects and how these defects in turn change the sink ability of GBs are not fully understood. For small angle tilt GBs, which are composed of sets of edge dislocations in the interface, it is established that point defects can be absorbed to edge dislocations by dislocation climb. For example, by load interstitials to tilt GBs in Mo, Novoselov *et al.*[112] showed tilt GBs accommodate defects by edge dislocation climb and GB energy evolves in a repeatable pattern as a function of the number of interstitials loaded onto GBs. Similar repeatable pattern in GB energy and free volume were also reported in continuous loading vacancies onto tilt GBs in Cu[113-114]. Besides dislocation climb, Frolov *et al.*[115] recently found that edge dislocation core in tilt GBs in Cu can reconstruct in response to different atom density at the interface. They proposed this could be one possible mechanism that tilt GBs can accommodate a certain amount of interstitials and vacancies under irradiation environments.

Those studies discussed above on tilt GB structure change to accommodate defects are very helpful. However, in real conditions, defect diffusion along GBs to other sinks and defect accumulation at GBs to drive structural change can happen simultaneously. It is of great importance to consider both processes in one model to simulate the real-time evolution of GBs under irradiation conditions. However, this ambition has been challenged by the timescale of different kinetic process. For investigation of defect properties and GB structural evolution, atomic simulations such as MD and DFT are the most appropriate techniques. While the timescale for defect segregation to GBs and defect diffusion along GBs is usually beyond that of typical atomic simulation timescale. In this case, KMC or rate theory based modeling is

necessary. Therefore, it is necessary to develop multiscale simulations to shed light on this complicated question.

In this section, the investigation on the kinetics of self-interstitials at small-angle tilt GBs (STGBs) and the impact of this kinetics on the long-term evolution of STGBs in irradiated SiC is presented. In SiC it is well known that vacancies diffuse much slower (*ab initio* migration barriers of C and Si vacancies are 3.66 eV and 2.70 eV, respectively)[29] as compared to interstitials (*ab initio* migration barriers of C and Si interstitials are 0.67 eV and 0.83 eV, respectively)[29] and therefore the defect fluxes to GBs are dominated by interstitials[54]. However, the kinetics of interstitials and clusters in GBs in SiC has not been reported yet and it is not known how GBs transport and annihilate these defects. In addition, for multi-component materials, defect flux to GBs may be off-stoichiometric[54] For instance, because the migration barrier of C interstitial (C_i) is lower than that of Si interstitial (Si_i), the flux of C_i to GBs is likely to be higher than that of Si_i. It is unclear how the off-stoichiometric flux affects the sink strength of GBs. Understanding this effect may also be relevant for other multi-component ceramics (e.g., ZrC[171]) that are proposed as cladding and structural component in reactors.

5.1 Structures of small-angle tilt GBs in SiC

Diffusion of defects along GBs to reach other sinks, such as surfaces and triple junctions, has been often considered an important pathway for annihilating defects in fine-grained materials[93-94, 105]. In order to determine the diffusivities of interstitials in STGBs in SiC, we constructed six STGBs with the tilt axis along the [001] direction and three STGBs with the tilt axis along the [011] direction. [001] and [011] STGBs with tilt angles smaller than 35^o were generated in a bicrystal supercell. When we attach two grains together to create an interface, some atoms might

be too close to each other. Therefore if two atoms were found at a distance smaller than 1.9 Å, one of them was removed. When deciding which atom to delete, we applied a rule that we maintain C-Si bonds across the interface and avoid energetically less favorable homonuclear bonds (C-C or Si-Si). We generated structures with both stoichiometric and off-stoichiometric dislocation cores (either with an excess of C or Si atoms) in order to find a configuration with the lowest GB energy. A schematic drawing of the supercell is shown in Figure 5-1a. The size of the supercell is approximately 8.0 nm × 3.5 nm × 9.1 nm along *x*, *y*, and *z* directions, respectively. We apply periodic boundary conditions in the directions parallel to the boundary plane (*x* and *z* axes). We make the outermost 4 layers of atoms normal to the *y* axis as rigid. The rigid slabs are allowed to move along the *y* direction to relax stress, and the length of the system along *y* direction is large enough to avoid unphysical interactions between GBs and the rigid slabs. Molecular dynamics (MD) simulations are used to optimize atomic structure of the GBs and to relax stresses in all directions.

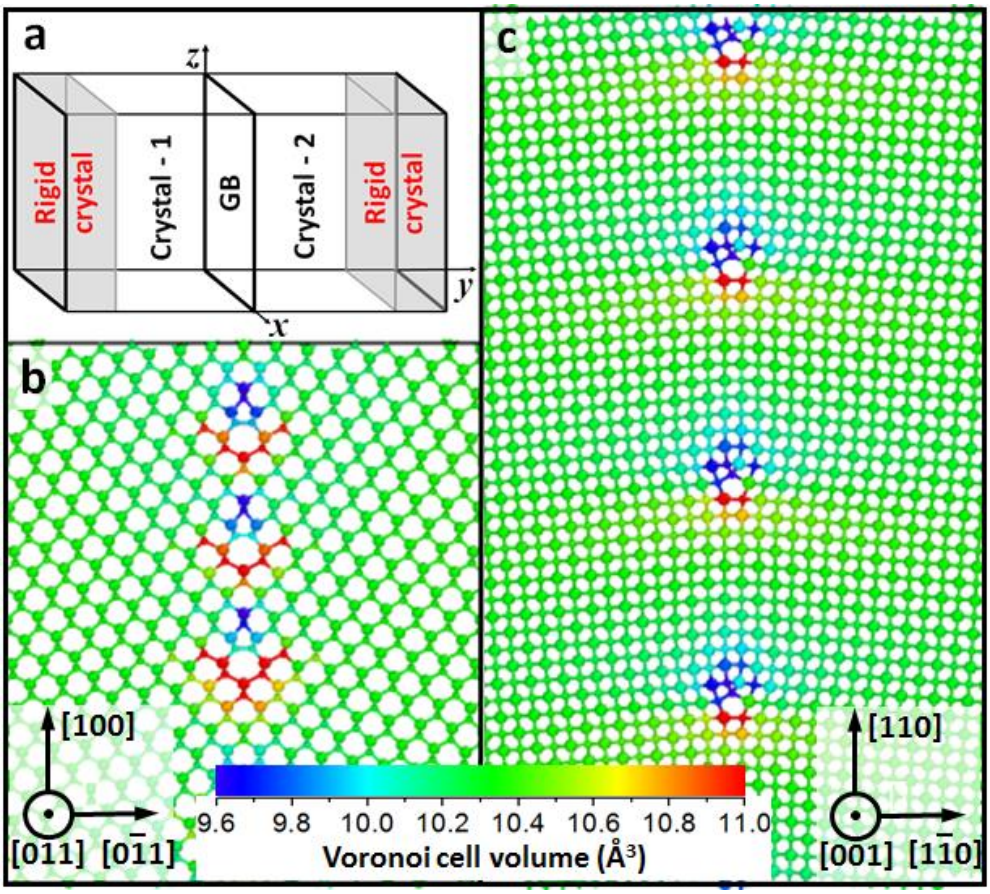

Figure 5-1 | The simulation supercell and GB structures. **a**, Schematic drawing of the bicrystal supercell; **b**, Tilt axial view of [011] (15$\bar{5}$), Σ73, θ = 13.4°; **c**, tilt axial view of [001] (670), Σ85, θ = 8.8°. Si and C atoms are shown as large and small spheres, respectively. Atoms in panel **b** and **c** are colored by the Voronoi cell volume[172]. This volume is a measure of a local strain field.

To find the energetically most favorable configurations, we first perform simulation in a constant volume, constant temperature (NVT) ensemble at T = 1000 K for 20 ns with a time step of 1fs. The system was then quenched to 0 K in 50 ps in constant temperature and pressure (NPT) ensemble for 20 ns with a time step of 0.5 fs to ensure the external pressure was relaxed to zero. Finally, we use the conjugate gradient method to minimize the system energy and we calculate GB energy E_{GB} as

$$E_{\mathrm{GB}} = (E_{\mathrm{cell}} - N_{\mathrm{C}} \times \mu_{\mathrm{C}} - N_{\mathrm{Si}} \times \mu_{\mathrm{Si}})/A \tag{5-1}$$

Here, E_{cell} is the energy of the supercell, and N_C and N_{Si} are the numbers of C and Si atoms, respectively. μ_C and μ_{Si} are the chemical potentials for C and Si atoms, respectively, and we choose $\mu_C = \mu_{Si} = 0.5\times\mu_{SiC}$ where μ_{SiC} is the energy of bulk 3C-SiC. For [001] and [011] STGBs, we found that boundaries with excess C atoms in the core (Figs.4-1b and 4-1c) have the lowest GB energy. Therefore, we use the boundaries with excess C atoms throughout our study. The optimized GB structures of [001] and [011] STGBs have similar structural units as the equivalent GBs in diamond, cubic-Si, and SiC [22, 173-174]. The Gao-Weber potential[130] is used in our MD simulations. This potential was chosen here not only because it can correctly describe GB structure, but also because it can describe the kinetics of intrinsic defects with a reasonable agreement with first principle calculations. For instance, the migration barrier of C interstitials in bulk is 0.74 ± 0.05 eV according to Gao-Weber potential[175] and 0.67 eV according to DFT[29]. The optimized structures of [001] and [011] STGBs consist of similar structural units as those previously found in diamond, cubic-Si, and SiC [22, 173-174]. In Figs. 4-1b and 4-1c, respectively, we show two representative STGBs structures, [011] $(15\bar{5})$ Σ73 and [001] (670) Σ85 (where Σ represents coincidental site lattice, […] represents the tilt axis, and (…) represents the GB plane). As expected, these STGBs are comprised of sets of edge dislocations at the interface. Detailed

information (e.g., tilt angles, Σ value, and GB energies) of the 9 total STGBs used in this study can be found in Appendix A3 FigureS15.

5.2 Diffusivity of interstitials in small-angle tilt GBs in SiC

In order to identify the GS structure of interstitials in GBs, we first load a single interstitial on one dislocation line in the GB plane. The system was heated to 1250 K in 5 ns and then quenched to 0 K in 5 ns with a time step of 0.01 fs in NVT ensemble using Gao-Weber potential[130]. We performed on the average 3 heat-quench cycles for each defect and each GB. Snapshots of the simulations were saved every 5 ps (producing ~2,000 snapshots per one heat-quench cycle) and each of the saved configurations was relaxed at 0 K using the conjugate gradient method. The binding energy E_b (or the segregation energy) of interstitials in each relaxed configuration was calculated as

$$E_b = E_{defect}^{GB} - E_{defect}^{intra\_grain} \quad (5\text{-}2)$$

where E_{defect}^{GB} is the energy of the bicrystal supercell with a defect at GB, $E_{defect}^{intra\_grain}$ is the energy of the same bicrystal supercell with a defect far away from the GB (in the crystalline region). The lowest E_b configurations are taken to be the ground states of C_i and Si_i in [001] and [011] STGBs. Binding energies of C and Si interstitial to [001] and [011] tilt GBs are listed in Appendix A3 Table S2.

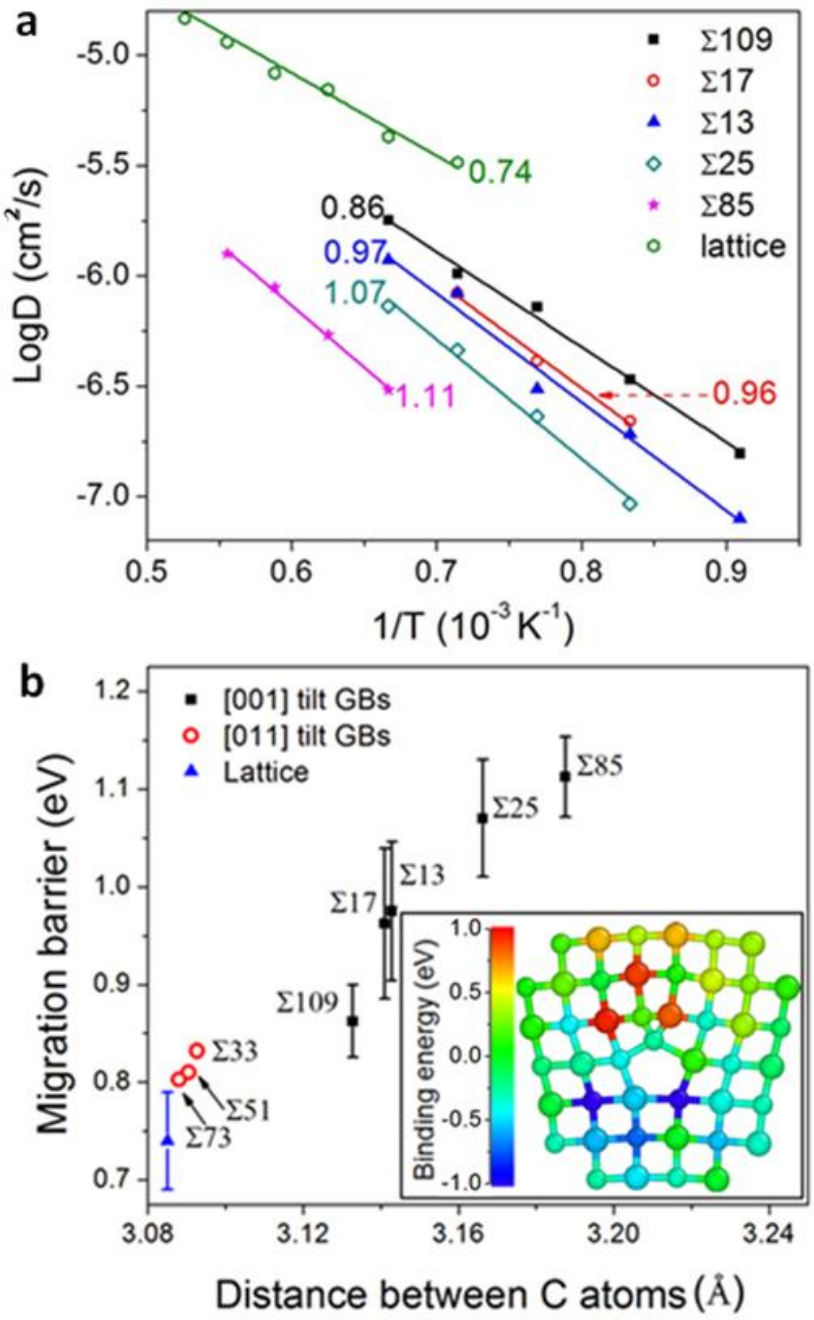

Figure 5-2 | Diffusion coefficients and migration barriers of C_i at GBs. **a**, Arrhenius plot of diffusion coefficients of C_i at [001] tilt GBs; numbers at the ends of each line represent the extrapolated migration barrier in eV; **b**, The migration barrier as a function of distance between C atoms along the minimum energy pathway. The inset shows the binding energy of C_i forming a dumbbell at different lattice sites near a dislocation core in [001] Σ85 STGB. Negative binding

energy (colored blue) means that the site is energy favorable for C_i. Large spheres represent Si atoms, and small spheres represent C atoms.

We calculated diffusion coefficients for carbon (C_i) and silicon (Si_i) interstitials in STGBs (Appendix A3 Table S2). These diffusion coefficients are plotted as a function of temperature in Figure 5-2a. By fitting the Arrhenius relationship to the data in Figure 5-2a, we determined migration energy barriers, which are shown in Figure 5-2b. Our calculations found that the diffusion coefficients of C_i in [001] STGBs are lower than in the bulk SiC by 1-2 orders of magnitude. Examination of C_i trajectories reveals that in [001] STGBs, C_i diffuses predominantly on a dislocation line along the tilt axis. The migration barrier of C_i along the tilt axis (E_m^{core}) is in the range of 0.81 – 1.11 eV, which is higher than the migration barrier in bulk (E_m^{bulk} = 0.74 ± 0.05 eV, calculated using the same empirical potential)[175]. The increase in the migration barrier in [001] STGBs was validated for selected structures by density functional theory (DFT) calculations and the climbing image nudged elastic band method (details in Appendix A3). In [011] STGBs, C_i was also found to migrate primarily along the tilt axis and the migration barrier was found to be in the range of 0.80 – 0.83 eV. This value is slightly higher than the migration barrier in bulk SiC.

It is interesting to ask why the interstitial migration barriers in STGBs are higher than in the bulk, since GBs have been often considered to be pathways for fast transport of defects[176-178] To understand the mechanisms underlying diffusion along GBs, in Figure 5-2b we plot the migration barriers of C_i as a function of the distance between C lattice atoms along the migration pathway. Here, the distance between C lattice atoms is used because MD trajectories show that when C_i diffuses along the dislocation line in STGB, this defect always attaches itself to lattice C atoms to form dumbbells. As shown in Figure 5-2b the migration barriers of C-C dumbbells

increase monotonically with the distance between C lattice atoms along the migration path for both [001] and [011] STGBs. This trend means that indeed diffusion is controlled by the transition from one dumbbell configuration to another and this transition is in turn controlled by the distance between C atoms along the migration path. This observation is in contrast to typical models of interstitial diffusion, where a larger spacing between GB atoms provides more open space for transport of interstitials and leads to a lower migration barrier as compared to the bulk diffusion[179]. In the case of STGBs in SiC, although interstitials do segregate, as expected, to the tensile regions in the GBs (there is more free volume for the interstitial in these regions), the same tensile strain that lowers formation energy of interstitials at these sites, leads to an increase of migration barriers because of the increased distance between C atoms.

Our MD simulations found that in all STGBs considered in this study Si_i is immobile on the MD time scales (μs) at temperatures up to 1500 K. The lack of mobility of Si_i can be attributed to the local structural changes of GBs that take place when Si_i is incorporated (details are discussed in Appendix A3).

In addition to the diffusion of interstitials along the dislocation line, we have also investigated diffusion along the direction parallel to the tilt axis, but still within the GB (e.g., diffusion along the [110] direction in the [001] STGBs shown in Figure 5-1c). Along this direction there are alternating regions of tensile and compressive strains; these strains arise due to the presence of edge dislocations that comprise the STGB. The tensile regions are energetically favorable for interstitials (because of the larger free volume) and there is a significant energy cost associated with the migration of the interstitials through the compressive regions. For instance, as shown in the inset of Figure 5-2b, the energy of C_i increases by 2.0 – 2.5 eV when C_i moves from the tensile region (below the dislocation core) to the compressive

region (above the dislocation core). It follows that the migration barrier is at least 2.0 eV. A similar lower bound on the migration barrier (1.6 eV) was found by us for the [011] STGBs. These barriers are much higher than the corresponding E_m^{core} at each GB (Table S2 in Appendix A3). In addition, the high binding energies of interstitials to dislocation core (Table S2 in Appendix A3) make it unlikely for interstitials to leave the boundaries. These two factors explain the one-dimensional diffusion of interstitials along dislocation cores observed in our MD simulations.

5.3 Annihilation of defect by jogs and jog nucleation

Interstitials arriving at a GB may bind to dislocation lines at pre-existing jogs, leading to dislocation climb. Annealing of defects at jogs involves multiple kinetic processes, including diffusion from bulk to dislocation cores, diffusion along dislocation cores to jogs, and attaching to jogs. It is important to ask whether annihilation of interstitials at jogs is limited by the diffusion of defects or by the reaction of attaching to jogs. In order to answer this question, in Figure 5-3 we plot the energy landscape for C_i diffusion from bulk to a dislocation core and from the core to jogs in [001] Σ85. First, one C_i diffuses from bulk to dislocation cores with a migration barrier of 0.74 eV (E_m^{bulk}). As C_i approaches GBs within a distance of 1 nm, the entire energy landscape as well as the transition barriers are lowered due to the interaction with dislocations[93] . The binding energy (E_b^{core}) of C_i to dislocation core is approximately 1.6 eV. When C_i reaches a dislocation core, the migration barrier increases to 1.2 eV (E_m^{core}) because of the stretched interatomic distance near the core, as discussed in Section 4.1.2. As C_i approaches the jog, the migration barrier starts to decrease at a distance of approximately 1 nm away from the jog. The activation energy barrier (~1 eV) for C_i attaching to a jog is lower than the migration barrier along the dislocation line (E_m^{core}= 1.2 eV). Therefore, the annihilation of interstitials at

jogs at STGBs of SiC can be considered to be a diffusion controlled process. Besides, the binding energy of C_i to jogs (E_b^{jog}) is as high as 1.5 eV so it is unlikely that once C_i is attached to a jog, it will be re-emitted and it will diffuse away from jogs. This binding energy is defined as the energy change when moving an interstitial from a jog to a ground-state configuration in bulk SiC.

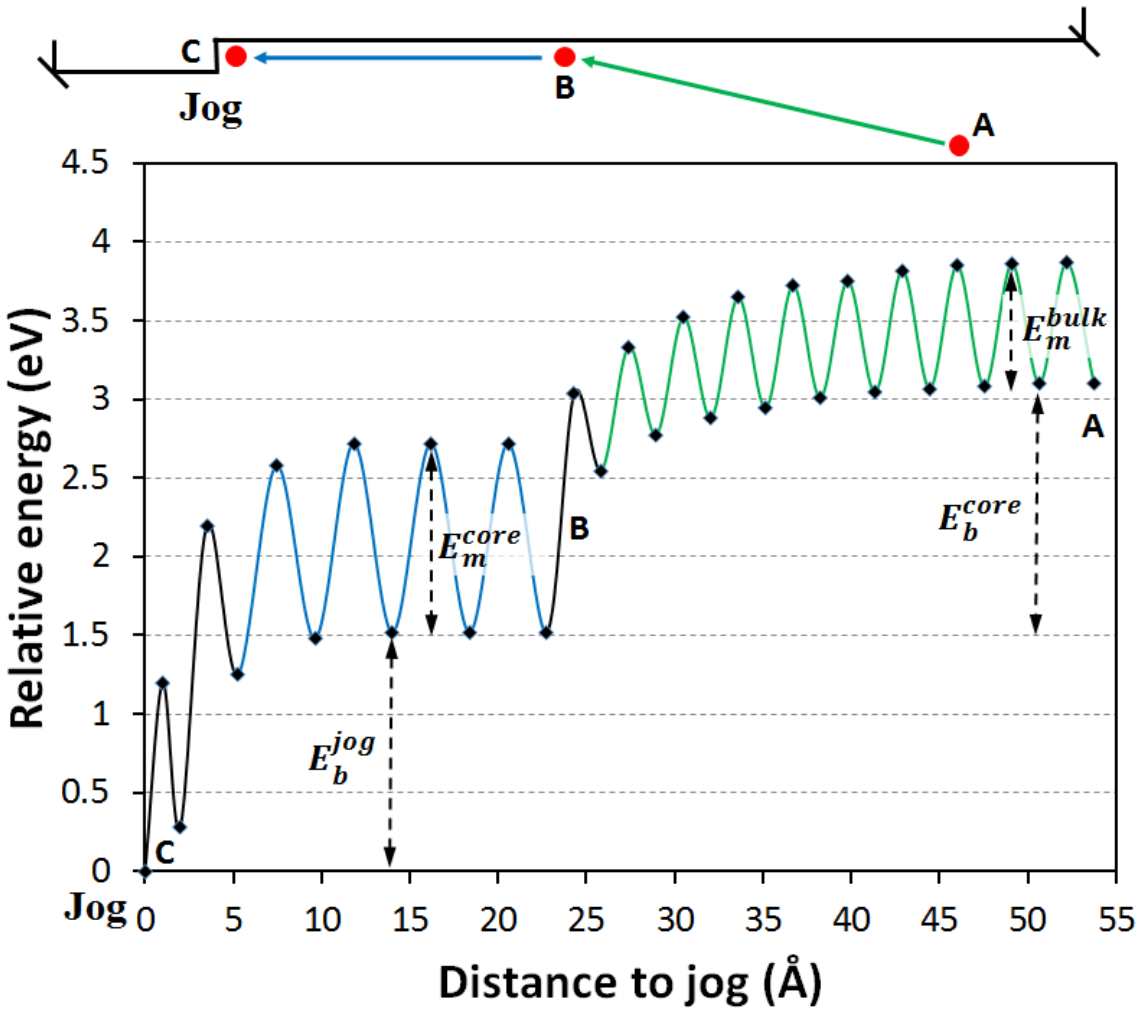

Figure 5-3 | The energy landscape for annihilating of C_i at jogs. Position A represents C_i in the bulk, B represents C_i segregated to dislocation cores at STGBs, and C represents C_i attached to jogs. In the schematic drawing, the green straight line represents the migration of C_i from bulk SiC to the dislocation core, and the blue straight line represents the migration of C_i along the dislocation line to a jog. The corresponding parts of the energy landscape are labeled using the same color scheme. E_b^{core} is the binding energy of C_i from bulk to dislocation cores, E_b^{jog} is the binding energy of C_i from dislocation core to jogs, E_m^{bulk} is the migration barrier of C_i in bulk SiC, and E_m^{core} is the migration barrier of C_i at dislocation core along the dislocation line.

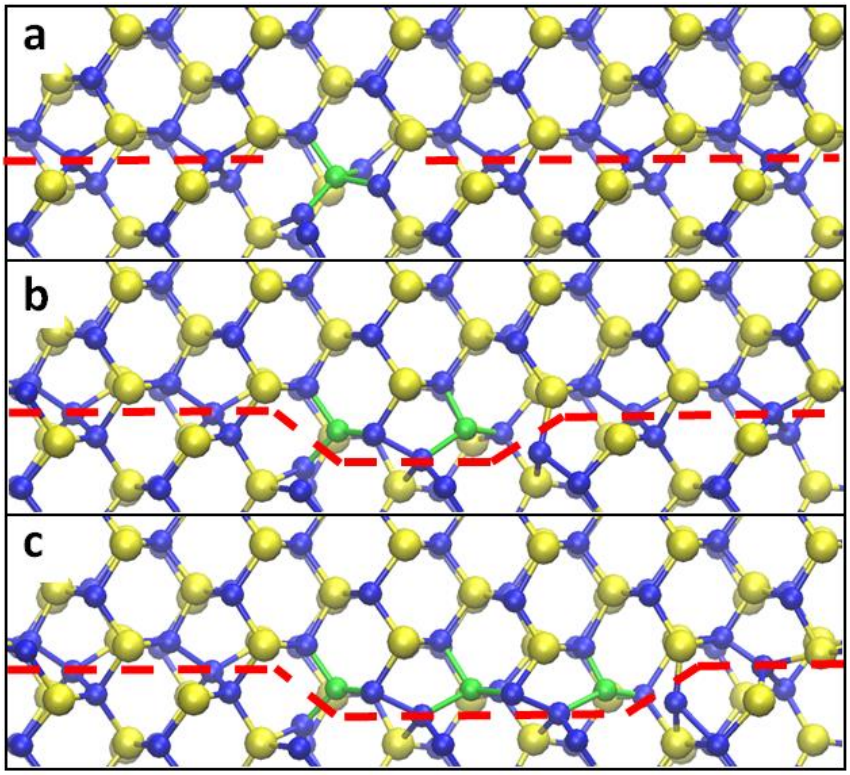

Figure 5-4 | Nucleation process of a jog from C_i clusters**. a**, A di-C_i cluster: the regular structure of dislocation line was disrupted at the site where the cluster was incorporated; **b**, A jog nucleated from 4-C_i cluster; and **c**, Jog extension by loading two more C_i to the jog shown in **b**. The red dashed lines mark the position of the dislocation line. Jogs are present at the location where the dislocation line is shifted. Large yellow spheres represent Si atoms, and small blue spheres represent C atoms. Newly incorporated C atoms residing at Si sites are colored green. Newly incorporated C atoms residing at C sites are colored blue in the same fashion as other C atoms in the lattice.

Interstitials that have segregated to GBs can not only attach themselves to existing jogs, but they can also agglomerate into clusters[105]. Because of the high migration barriers of interstitial clusters in SiC[159], annihilation of clusters by diffusion is limited. However, when a cluster is formed at STGBs, it can be annihilated by nucleating a new jog on a dislocation line. The

activation energy for jog nucleation and the minimum cluster size required for nucleation are important parameters that determine the jog nucleation rate. In order to determine these parameters and to understand the mechanisms of jog nucleation, we conduct MD simulations at elevated temperatures. We first introduce a di-C_i cluster on the dislocation line and keep the system in equilibrium at 1250 K for 100 ns. The structure of di-C_i cluster after annihilating is shown in Figure 5-4a. No diffusion or dissociation was observed in the simulation. Two more C_i were then loaded next to the di-C_i cluster at a distance of a few angstroms. The system was subsequently heated to 1250 K for 20 ns, followed by a quench to 0 K in 500 ps. In this process we found that a pair of jogs was nucleated from the 4-C_i cluster, as shown by the shift of the red line in Figure 5-4b. We repeated the above simulations at different temperatures (the lowest temperature was 500 K) for both stoichiometric (the same number of C_i and Si_i) and off-stoichiometric (C_i only) clusters, and the nucleation of a jog pair was observed in all simulations within MD timescale (up to μs). We can estimate the upper bound for the reaction barrier of the nucleation process by assuming that one nucleation event took place at 500 K over the time of 1 μs. The upper bound estimate of the energy barrier is 0.66 eV, and it is lower than the migration barrier of C_i in bulk (0.74 eV) and in GBs (0.81-1.1 eV). This implies that the nucleation of jogs from interstitials clusters is a fast process and that rate of jog nucleation is controlled by diffusion of interstitials along the GB. In addition, our simulations show that nucleation of a jog in STGBs requires a cluster with sizes as small as four interstitials as seen in the simulations. The nucleated jog pair can further annihilate nearby interstitials, as shown in Figure 5-4c where two C_i were loaded near the jog and annihilated at 1250 K within tens of ns.

The above analysis implies that a dislocation climb in STGBs can take place even if the flux of interstitials is off-stoichiometric. Since C interstitials can be incorporated into STGBs as

antisites (C_{Si}, shown as green spheres in Figure 5-4), the atomic plane left behind a climbing dislocation is rich in C antisites. This is different from the climb mechanism proposed by Petroff and Kimerling[180-181] for binary III-V semiconductors with a zinc blend crystal structure. According to their mechanism, if only one type of interstitials (e.g., of species A) diffuses to a jog in an alloy AB, then a Frenkel pair (an interstitial and a vacancy) of species B can nucleate near the jog. The interstitial of species B is then absorbed by the jog in order to keep the dislocation core stoichiometric and as the result the climbing dislocation leaves behind a vacancy rich dislocation plane. In contrast, in SiC, dislocation climb in STGBs does not require an equal number of C and Si atoms and it can take place by absorption of C_i only (leaving behind a plane rich in C_{Si}). However, stoichiometry is still energy preferable in SiC. Our MD simulations found that if a Si_i is found next to a dislocation core or near a C-rich plane, it will undergo a reaction with C_{Si} (i.e., $C_{Si} + Si_i \rightarrow Si_{Si} + C_i$) to restore the local stoichiometry. This reaction has been found to be both thermodynamically favorable[29, 130] and kinetically feasible (i.e., with a barrier of 0.68 eV[29]) in bulk SiC.

To test the generality of our results, we repeated the above studies for other [001] and [011] STGBs and we found the same general processes of interstitial annihilating at jogs and jog nucleation from interstitial clusters (Appendix A3). The following conclusions can therefore be made about defect annihilation in STGBs in SiC: (1) annihilation of defects at jogs is diffusion controlled (i.e., the energy barrier to defect attachment is lower than the barrier to diffusion); (2) jog nucleation from an existing interstitial cluster can be viewed effectively as a barrierless process (i.e., the nucleation barrier is lower than the migration energy); (3) the minimum number of interstitials needed to nucleate a jog pair is four, regardless of the cluster composition.

5.4 Multiple roles of small-angle tilt GBs in annihilating defects

So far we have illustrated the details of kinetics of several processes that can annihilate interstitials in STGBs in SiC. These processes include pipe diffusion to other sinks, pipe diffusion to existing jogs, and jog nucleation from clusters. Here, we develop a dislocation line model that takes into account these processes as well as the flux of defects to GBs in order to predict how STGBs annihilate radiation-induced defects at long time scales. In this model, we use one single dislocation line to represent sets of edge dislocations at STGBs. This simplification is valid under two assumptions. First, each dislocation in a STGB annihilates defects independently. This assumption can be justified because of the high activation energy (over 1.6 eV) for interstitials to migrate between dislocations within STGBs, so there is no mass transport among dislocations. Second, all dislocations in one STGB behave similarly in response to uniform defect fluxes to GBs. Under this scenario, each dislocation receives similar numbers of interstitials from bulk and they climb at similar rates. The distance between neighboring dislocations is maintained and they will not run into each other. The length of the dislocation line is taken to be equal to the average grain diameter. The ends of the dislocation line are assumed to be ideal sinks for defects such as surface and triple junctions[105, 182]. Once interstitials have diffused to either end of the dislocation line, they are annihilated by these sinks and therefore removed from the dislocation line. The flux of defects to the dislocation line is determined by the irradiation conditions (i.e., the dose rate, temperature, and grain size) and by the spacing between dislocation lines in a chosen STGB configuration. When interstitials reach a dislocation line, they can undergo one-dimensional diffusion along the dislocation line. They can also form clusters with other interstitials or be annihilated by attaching to existing jogs and clusters.

The dislocation line model is based on the following facts which are found in MD simulations of STGBs in SiC:

1. C_i performs one dimensional diffusion along the dislocation line with a barrier that is different for each STGBs. However, we found that when predicting the role of GBs in annihilating defects, it is not critical to choose a specific GB and the corresponding migration barrier. This is because the definition of diffusion length to dislocation length (parameter λ), contains information about defect kinetic parameters, including the migration barrier. This is illustrated in details in Appendix A3.
2. Movement of a jog by a unit distance requires attachment of 2 interstitials to the jog. This is due to the nature of dislocations in SiC. Specifically, as shown in Figs. 4-1b and 4-1c, the dislocation plane is composed of 2 atomic layers. If a pair of C_i or Si_i is attached to the jog, no antisite is produced as the jog moves. If two C_i are attached to the jog, a C antisite is produced during the movement of the jog.
3. Once formed, C-rich core and C-rich half plane are stable in the system.
4. Si_i does not diffuse along GB, but it can restore the stoichiometry of a C-rich site (if it diffused to such a site from bulk SiC). A mobile C_i is released during this process.
5. Clusters are immobile, and can nucleate a jog when the cluster size is equal to or larger than four and this is a barrierless process.
6. Interstitial re-emission to bulk was ignored for the following reasons. We can calculate the rate Γ of an event as $\Gamma = ve^{(-E/kT)}$ where v is vibrational frequency of atoms, E is the activation energy barrier, k is the Boltzmann constant, and T is temperature. In the temperature range of interest (500 – 1000 K), we found that the hop rate during diffusion is 2 – 3 orders of magnitude higher than the re-emission rate (migration barriers and

binding energies are listed in Table S2 in Appendix A3). Therefore, it is reasonable to assume that diffusion dominates the kinetics of interstitials at STGBs.

7. Ends of the dislocation line are ideal sinks, such as surfaces and triple-junctions. This assumption has been often used for GB models such as those reported in literatures[105, 182].

The model was developed in the following steps. First, the flux J of interstitials to STGBs was calculated from the rate theory model reported in Ref[54]. J is in the units of #/(m^2×s) and the fluxes under various irradiation conditions are listed in Table S3 in Appendix A3. Given the spacing d between dislocation lines in a given STGB, the flux to dislocation line can be approximated as $J \times d$ (in the units of #/(m×s)). The length of a dislocation line L in STGB was assumed to be equal to the grain diameter, and then the time interval Δt to load one interstitial to dislocation line was calculated as $\Delta t=(J \times d \times L)^{-1}$ in the units of seconds. That means that one interstitial is loaded to the dislocation line every Δt seconds, and the predefined ratio of C_i flux to Si_i interstitial flux to GBs determines whether a C_i or Si_i is loaded. In the meantime, mobile C_i at GBs diffuse one dimensionally along the dislocation line by a distance of $(2Dt_{step})^{0.5}$, where $(2Dt_{step})^{0.5}$ is the average diffusion distance of C_i within a single time step of t_{step} ($<\Delta t$). After the diffusion of C_i within a small time step of t_{step}, an algorithm was implemented to check conditions for events such as cluster formation, annihilation of interstitials at jogs and dislocation ends, jog nucleation, etc. The criterion to determine whether these events can occur is detailed in Appendix A3. The simulation clock was advanced by t_{step} in each step in the dislocation line model. Within each time step, events such as loading interstitials to the dislocation line, diffusion of interstitials, and annihilation of interstitials to jogs, etc., are considered. A pseudo-code that shows the implementation of the model is shown in Appendix A3. Snapshots from the dislocation line simulations are shown in Figure 5-5 and a movie of a full simulation can be

found in Video S5 in Appendix A3. Snapshots from simulations carried out using the dislocation line model are shown in Figure 5-5.

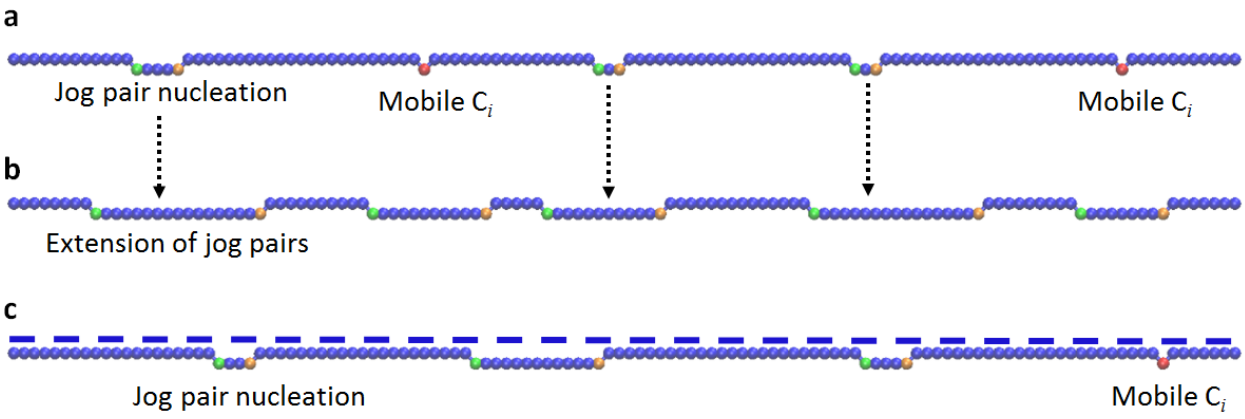

Figure 5-5 | Snapshots from the dislocation line simulations. **a**, Initial stage, where mobile C_i are loaded onto the line and diffuse to form clusters and nucleate jogs; **b**, Extension of jog pairs by absorbing interstitials; and **c**, The entire dislocation line climbs down by a unit length, and new jogs nucleate on the line. Mobile C_i are colored red, jogs moving to the left are colored green, and jogs moving to the right are colored orange. The initial position of the dislocation line is shown by the straight dashed line in panel **c**.

The flux of defects to GBs was calculated by using *ab initio* based rate theory model described in Ref.[54]. The rate theory model predicts that the flux of defects to GBs is dominated by interstitials, and that the ratio of the C_i flux to the Si_i flux (C/Si) to GBs ranges from 10 to 20, depending on the irradiation conditions. However, the rate theory model from Ref. [54] ignores the possibility of defect clusters formation inside the grain, which assumption may potentially affect the stoichiometry of the flux. To take into account the uncertainties of the rate theory model, we treat the C/Si ratio as a parameter in our dislocation line model and we set it to be 1, 10, 20, and 100 to simulate cases of stoichiometric, as well as slightly, medium, and highly off-stoichiometric fluxes.

Simulations with the dislocation line model were performed for the following range of conditions: 1 – 5 displacement per atom (dpa) under irradiation conditions of 10^{-5} – 10^{-3} dpa/s, at temperatures of 200 – 1100 K, and with the grain diameters of 0.1 – 20 μm. This set of parameters covers most of the experimetnal conditions reported in studies on radiation resistance of nano- and microcrystalline SiC [98-102, 183-184]. In addition, we developed a single parameter λ to represent interstitial accumulation rate at STGBs for various STGBs, grain sizes, and irradiation conditions. This parameter is defined as the interstitial diffusion distance divided by the dislocation line length (grain diameter). The interstitial diffusion distance is in turn defined as the average C_i diffusion distance along the dislocation line before the arrival of the next interstitial to any place on the dislocation line. It is calculated as $(2D\Delta t)^{0.5}$, where D is the diffusion coefficient of C_i along the dislocation line and Δt is the time interval between the arrivals of interstitials to the dislocation line. Δt is determined by the flux of interstitials to GBs, which in turn depends on the exact irradiation condition. A high value of λ implies a high chance for interstitials to diffuse to the ends of the dislocaiton line and a low chance to form clusters with the next interstitial arriving to GBs within the time interval Δt. Therefore, a high value of λ represents a low defect accumulation rate on the dislocation line. The values of λ of STGBs under various irradiation conditions are listed in Appendix A3 Table S3.

When performing simulations with the dislocaiton line model, we count the number of interstitials that diffused to the ends of the dislocation line (e.g., surfaces and triple junctions), and the number that is annihilated by a dislocation climb (i.e., attaching to existing jogs and nucleating new jogs). We will refer to the regime when more than 50% of interstitials diffuse to other sinks along STGBs as a diffusion channel regime, and the regime when more than 50% are annihilated by dislocation climb as the climb regime. In Figure 5-6, we plot the number of

interstitials in the diffusion channel regime (labeled as channel in Figure 5-6) and the dislocation climb regime (labeled as climb in the same figure) as a percentage of the total number of interstitials segregated to GBs. The horizontal axis corredsponds to the parameter λ, as defined previously.

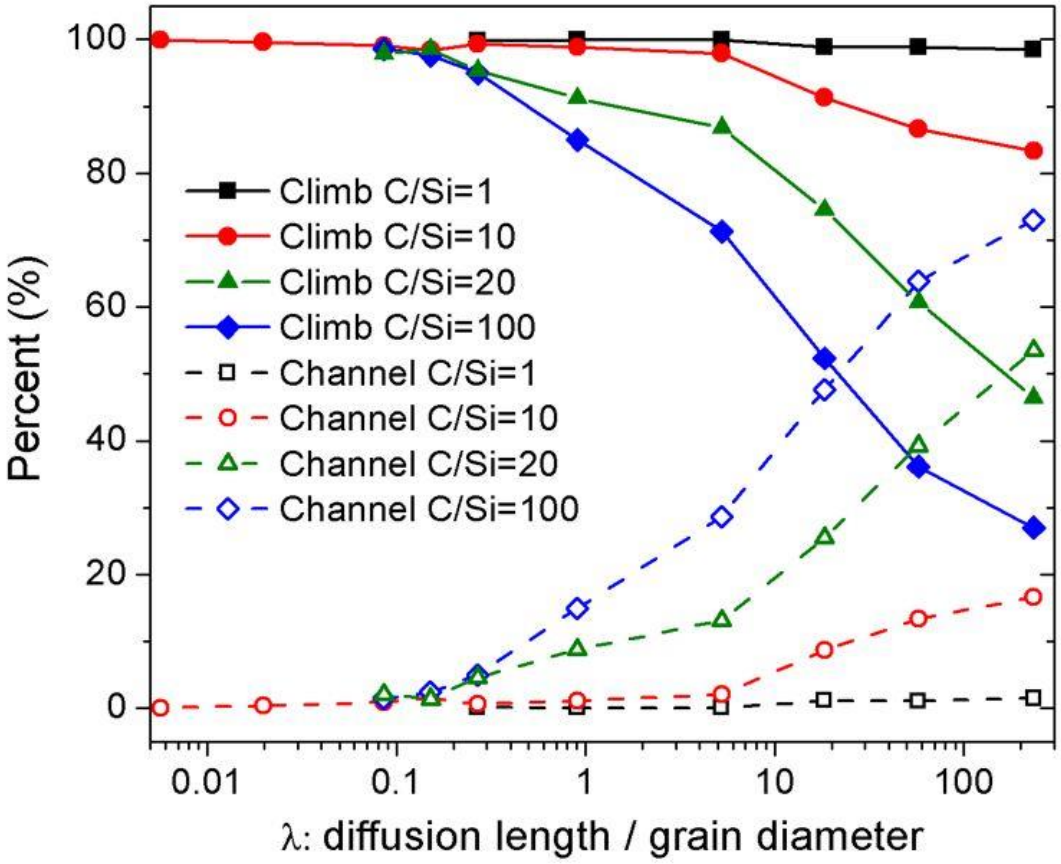

Figure 5-6 | The role of STGBs in annihilating defects under various irradiation conditions. Climb means annealing of defects at jogs or by jog nucleation. Channel means diffusion of defects along GBs to other sinks. C/Si means the ratio of Ci to Sii that diffuse to GBs as defined in the main text.

Our dislocation line model predicts that the role of STGBs in annihilating radiation damage in SiC depends on the accumulation rate of interstitials at GBs, which is determined by the grain

size and the irradiation conditions. For the case of an off-stoichiometric flux with C/Si = 20 or 100, there is a transition between the diffusion channel regime and the dislocation climb regime as a function of irradiation conditions and grain size. The diffusion channel regime occurs under conditions where the ratio λ is higher than 20. In general, this corresponds to cases (according to Appendix A3 Table S3) of a relatively small grain (less than 100 nm in diameter) irradiated to a low dose rate (lower than 10^{-3} dpa/s) at a high temperature (higher than 800 K). Under these conditions, C_i that have segreated to GBs can diffuse quickly along dislocation lines to reach other sinks. This process allows C_i to avoid gettting trapped in immobile defect clusters along the dislocation line. The dislocation climb regime is found when a material has either a relatively large grain size (diameter larger than 100 nm), or it is irradiated to a high dose rate (10^{-3} dpa/s and higher), or it is irradated at relatively low temperatures (800 K and lower). Under these conditions more than 50% of C_i that diffused to STGBs are annihilated by dislocation climb. Immobile C_i clusters unavoidably form at GBs because of the high concentration of C_i, a slow diffuion as well as the long diffusion distance required to reach other sinks. Interstitial clusters can nucleate jogs when cluster consists of at least four interstitials. An increase in the jog density at GBs further rises the fraction of interstitials that are annihilated by dislocation climb. The situation is qualitatively different for stoichiometric (C/Si = 1) and slightly off-stoichiometric fluxes (C/Si = 10), where we find STGBs mainly annihilate segregated interstitials by dislocation climb. In these cases, a high concentration of Si_i reached GBs and became immobilized on the dislocation line due to structural reconstruction discussed in Appendix A3. These immobile Si_i can trap mobile Ci_i to form clusters, which in turn nucleate jogs and annihilate additional defects.

5.5 Discussion and conclusions

Defect clusters are usually considered to be detrimental to the thermomechanical properties of irradiated materials. As clusters are generally immobile, they cannot be easily annealed and their accumulation can lead to swelling, creep, and embrittlement. However, in STGBs in SiC, interstitial clusters can be beneficial as they can easily nucleate new jogs, which in turn serve as sinks for other defects and hence increase GBs' sink ability. The ability of STGBs to transport point defects and to annihilate defect clusters implies a high sink strength of this type of boundaries. This conclusion is consistent with the experimental observation of an increased radiation resistance of nc-SiC grown by chemical vapor deposition (CVD)[101-102]. The CVD-grown nc-SiC samples have a texture and therefore contain a high concentration of low-angle GBs as compared to randomly oriented grains in a micro-crystalline samples[101-102]. Since studies on other types of nc-SiC samples have shown this material to have a lower resistance to radiation-induced amorphization than the microcrystalline SiC[101-102], it is possible that the STGBs present in CVD samples contribute to their increased radiation resistance. Other phenomena proposed to be responsible for the increased resistance of CVD grown nc-SiC samples include the presence of stacking faults in these samples[102, 185] and the long-range stress-field of STGBs that increases the defect flux to STGBs[93] in SiC.

Our dislocation line model can also provide information about the rate of dislocation climb in STGBs under irradiation. We found the climb rate to be sensitive to the grain size. For μc-SiC (e.g., grain diameter ~ 1 μm), the climb rate is less than 1 atomic spacing (~ 0.2 nm) per dpa in the dislocation climb regime. For nc-SiC (e.g., grain diameter ~ 50 nm) in the dislcoation climb regime, the climb rate can be as large as 5 atomic spacings (~ 1 nm) per dpa. Because dislocation lines at STGBs in larger grains are longer, they require higher numbers of interstitials to attach in

order for the entire dislocation to climb one unit atomic spacing. Therefore, dislocation lines in STGBs in larger grains have a low climb rate per dpa as compared to their conterparts in smaller grains. The high dislocation climb rate at STGBs in nc-SiC implies GBs undergo significant structural evolutions under irradiation. For instance, dislocation cores can climb to triple junctions or surfaces and be annihilated there. In the meantime, new dislocation cores can nucleate at the boundaries to maintain the grain misorientation. However, this is unlikely to happen in μc-SiC because of the low climb rate.

In summary, we found that once interstitials have segregated to the STGBs, the pipe diffusion of these defects in these GBs is slower than bulk diffusion. This is because the stretched interatomic distance at dislocation cores raises the migration barrier of interstitial dumbbells. Furthermore, we found that the annihilation of interstitials at jogs has a low activation energy and thus is a diffusion-controlled process. Jog nucleation from interstitial clusters is also found to be a process with a very low activation energy (relatively to the migration energy barriers) when the cluster size is equal to or larger than four, regardless of its composition. Finally, a dislocation line model was developed to take into account defect flux to GBs, pipe diffusion of defects in STGBs, and interactions between defects and jogs. This model reveals the multiple roles of STGBs in annihilating radiation-induced defects in SiC. It predicts that STGBs mainly serve as a diffusion channel for defects to reach other sinks like surface when the defect accumulation rate at boundaries is low. The diffusion channel regime occurs in nano-crystalline materials with small grain diameter (smaller than 100 nm) irradiated under low dose rate (lower than 10^{-3} dpa/s) at high temperature (higher than 873 K). In other cases, when the accumulation rate is high, most of the defects diffused to STGBs are annihilated by dislocation climb.

Chapter 6 Twist Grain Boundaries as Defect Sinks in SiC

While interactions between defects and tilt GBs as well as the long-term structural evolution of tilt GBs are relatively well understood, the question of how twist GBs evolve to accommodate defects has been rarely touched. Compared to edge dislocations in tilt GBs, screw dislocation network in twist GBs is far more complicated and it is still unclear how exactly screw dislocations can annihilate point defects. So far, only few studies[118-119] tentatively try to answer this question. In early 2012, Matínze *et al.*[118] investigated the segregation of vacancies to {001} twist GBs in Cu by a KMC model. The {001} twist GBs feature square grid of screw dislocations. They found under low vacancy loading rate, vacancies can diffuse to dislocation networks and form voids. While under high vacancy loading rate, vacancies aggregate and form voids at both dislocation core and in non-dislocation region in the GB plane. Later that year, this group investigated the segregation of vacancies in {110} twist GBs in bcc Fe and {111} twist GBs in fcc Cu using an advanced KMC model[119]. The Fe {110} twist GBs feature hexagonal screw dislocation network, and the Cu {111} twist GBs feature alternating stacking fault (SF) and unfaulted region in triangular shape separated by partial dislocations. A strong preference for vacancy to segregate to dislocation intersections was reported in both cases. What's more interesting, they found vacancies aggregation at dislocation intersections in Cu {111} twist GBs can lead to the shrink of SF area. From these studies, it is obvious twist GB structure undergoes noticeable structural change as defect accumulated at the interface. However, the number of vacancies loaded at GBs in these studies is too few (correspond to 10^{-4} dpa) to conclude long term evolution of twist GBs under irradiation.

A good understanding of how twist GBs evolve to accommodate defects is very important. On the one hand, twist GB is one major category of GBs (tilt, twist, mixed) and its radiation

response are relevant for applications of poly-crystalline materials for components in reactors. On the other hand, a good understanding of twist GB's response to defect accumulation also provides insight on how general GBs (a combination of both tilt and twist feature) behave under irradiation, which is of broader interest to GB-defect interaction but still unclear up-to-date. Another interesting aspect of this question is how screw dislocations absorb defects. Unlike edge dislocations climb to absorb point defects in tilt GBs, screw dislocations in twist GBs cannot climb. Previous studies found screw dislocation can absorb point defects or frank loops by forming mixed dislocation in the shape of helical turns[186-190]. These mixed dislocations can climb to absorb defects due to its edge component. However, it is unclear whether screw dislocations at GBs with constrains from neighboring lattice can still accommodate defects in a similar way.

In this study, we investigate defect kinetics in {001} and {111} small-angle twist GBs and structural evolution of these GBs to accommodate defects in SiC. It is important to note that defect flux to GBs in irradiated SiC is predicted to be dominated by interstitials rather than vacancies from an *ab initio* based rate theory model[54, 116]. Therefore, in this study we will focus on the kinetics of interstitials at twist GBs and how interstitial accumulation can drive GB structural evolution in SiC in the long run.

6.1 Defect segregation and kinetics at {001} twist GBs

The common structure of {001} twist GBs with twisting angle from 5° to 12.5° is shown in Figure 6-1a by using Σ85 θ=8.8° as an example. The interface is a square grid of screw dislocations with Burgers vector $\vec{B} = \frac{a}{2}[110]$ or $\frac{a}{2}[\bar{1}10]$. The distance d between parallel dislocations depends on the twist angle θ by:

$$d = \left|\vec{B}\right| / 2\sin(\frac{\theta}{2}) \tag{6-1}$$

Similar square grid of screw dislocations on (001) twist GBs have been observed by electron microscopy or atomic simulations in fcc metal Cu[118] and Au[191]. All{001} twist GBs generated in this study were detailed in Figure S21 in Appendix A4.

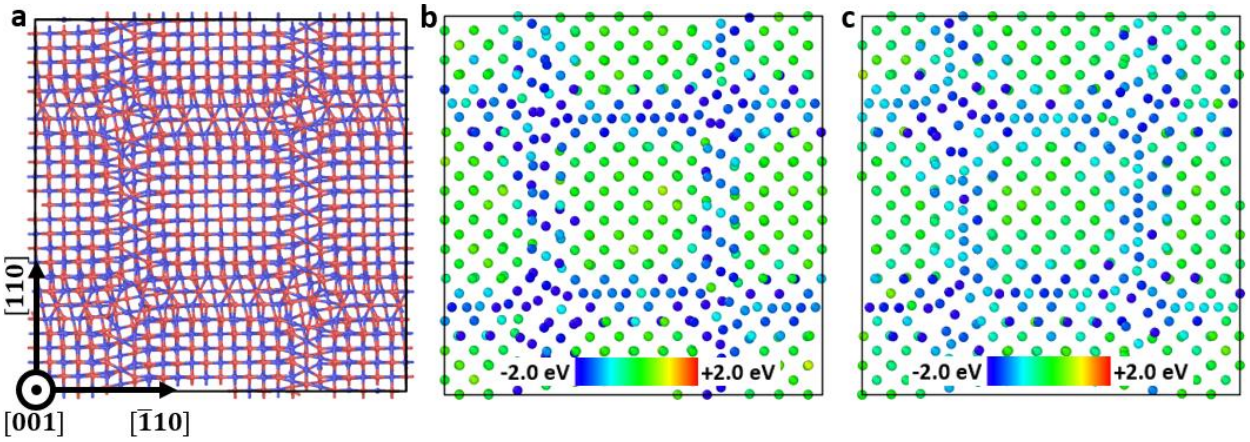

Figure 6-1 | Atom structure and defect segregation energy at (001) Σ85 θ=8.8° twist GBs. **a**, atom structure; **b**, segregation energy of C interstitials; **c**, segregation energy of Si interstitials. In panel **a**, atoms in red are C and others in blue are Si.

With the interface structure determined, we now exam the segregation energy of interstitials at GBs by using

$$E_{seg} = E_{defect}^{GB} - E_{defect}^{bulk} \tag{6-2}$$

where E_{defect}^{GB} is the energy of a bi-crystal supercell with one interstitial at GB, E_{defect}^{bulk} is the energy of the same supercell with one interstitial in lattice away from both GB and the frozen layers (in Figure 6-1). With this definition, a negative value of the segregation energy means it is energy favorable to form an interstitial at that site. Interstitials are loaded at different positions in the GB, followed by a 50 ps NVT simulation at 500K and a fast quenching to relax the structure. Results are shown in Figure 6-1b and 6-1c. It is clear that dislocations and multiple dislocation intersections (MDI) are strong traps to interstitials in the interface, and MDI are stronger than

dislocations. To be more specific, the segregation of C interstitial is around -2.4 eV on dislocations, and approximate -3.4 eV at MDIs. The segregation energy of Si interstitial is around -1.8 eV on dislocations, and -3.5 eV at MDIs. It is clear there is a deep potential well for both C and Si interstitials at MDIs. Besides, we also found the interaction between defect and GB is short-ranged. Interstitial formation energies are altered by GBs only within 2 layers of atoms next to the GB plane on each side.

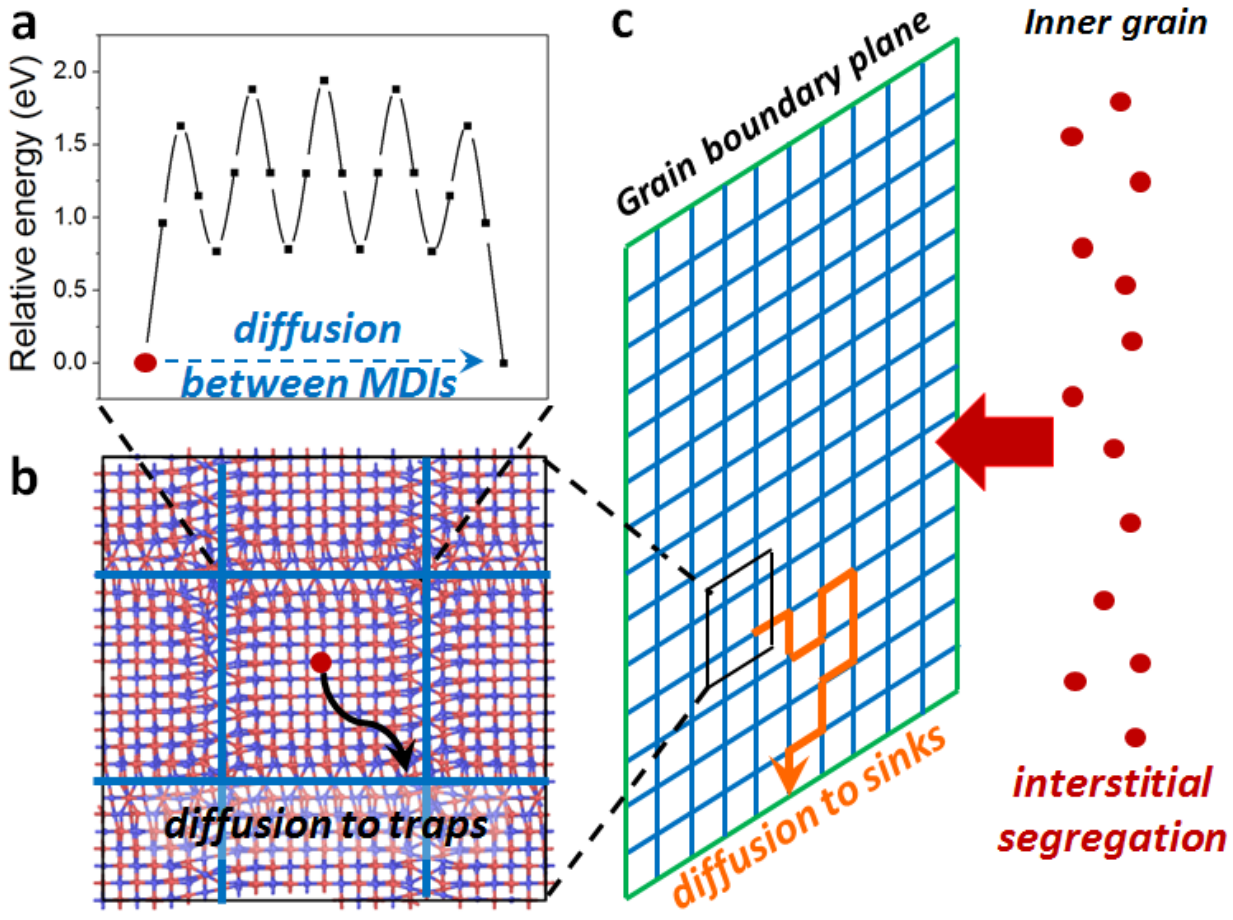

Figure 6-2 | Kinetic processes of interstitials at {001} twist GBs.

Our previous study on small-angle tilt GBs concluded multiple roles of tilt GBs in annihilating defects. Depending on grain size and radiation conditions, tilt GBs can either transport defects to other sinks (triple junctions or surface) as a diffusion channel, or remove

defects by GB structure evolution (growing lattice by dislocation climb in tilt GB). It is important to exam whether twist GBs can play multiple roles in removing defects under various irradiation conditions. Here we are going to compare the timescale of several kinetic processes at (001) twist GBs. The first process is segregation of interstitials from inner grain to grain boundaries, shown as the red arrow in Figure 6-2c. Once interstitials segregated to GBs, they can either diffuse through the lattice to reach dislocation grid (black arrows in Figure 6-2b), or diffuse along dislocation grid to reach the ends of GBs (orange trajectory in Figure 6-2c). The ends of GBs are assumed to be defect sinks such as triple junctions or surfaces that can annihilate these defects. The timescale of these kinetic processes determines how fast twist GBs can transport defects to other sinks under a certain defect flux to the interface, and therefore determines whether there will be defect accumulation at twist GBs.

Here we use t_{seg} to denote the timescale of interstitials segregation to GBs in the unit of second. It means the average time interval between the arrivals of two successive interstitials from inner grain to GBs. t_{seg} can be calculated from interstitial flux J (#/nm^2·s) to GBs, as determined from an *ab initio* based rate theory model[54]. Details on implementation and parameters used in this model can be found in Ref.[54]. Here we varies the grain radius r of SiC and radiation environments (dpa rate, temperature, total dpa) to consider a wide range of conditions. By assuming the area of GB to be πr^2, we can obtain t_{seg} by $(J\cdot \pi r^2)^{-1}$. The time of interstitials diffusion through lattice region inside the interface to dislocation grid is denoted as t_{trap} (unit: second), and is approximated as

$$t_{trap} = \frac{(d/2)^2}{4D} \tag{6-3}$$

where D is diffusivity of interstitials in bulk SiC[175], d is the distance between parallel dislocations, and a factor of 4 is used for 2-dimensional diffusion. The time of interstitials

diffusion along dislocation grid to reach ends of GBs is denoted as t_{sink} (unit: second). To determine t_{sink}, we employ a similar strategy of coarse grain modeling of GBs as implemented in Ref.[192]. First of all N_{step} for interstitials to diffuse from the center of GB to ends. t_{sink} can be calculated as $N_{step} \times \tau$.

Results of t_{seg}, t_{trap}, and t_{sink} for SiC in various grain size under different radiation conditions are shown in Table S4 in Appendix A4 and the general trend is summarized here. First of all, $t_{trap} << t_{seg}$ under all circumstances. This is because the diffusion distance in process t_{trap} is only 1 nm (half distance between MDIs) in Σ85 or becomes even short in GBs with higher twisting angles. Given the high mobility of interstitials in SiC in the temperature range 573 - 1173 K, it is not surprising to conclude t_{trap} to be in the timescale of ns - ps. However, t_{seg} is in a timescale beyond μs due to the long diffusion distance (grain radius in tens of nm to μm) in the segregation process. Therefore, we can conclude interstitials that segregated to twist GBs can quickly diffuse to and get trapped at dislocations or MDIs. It is unlikely for two or more interstitials to form clusters in lattice in-between dislocation grids within the GB plane. Second, $t_{seg} << t_{sink}$ for most cases. Interstitial diffusion along dislocation grid to reach sinks is found to be retard because of the deep potential well at MDIs (e.g., at least 1.6 eV for C interstitial to escape as shown in Figure 6-2a). This implies interstitials will accumulate at MDIs in twist GBs and therefore drive GB structural change in the long run. Exceptions are SiC in small grain size (blow 100 nm) irradiated in low dose rate (below 10^{-5} dpa/s) at high temperature (over 873 K). Under this condition, interstitials can frequently escape from MDIs and diffuse a short distance to sinks. The above analysis on t_{seg}, t_{trap}, and t_{sink} is also true for Si interstitial considering the even deeper potential well at MDIs (1.7 eV plus migration barrier). Therefore, we can conclude interstitials

accumulation on dislocation grid, especially at MDIs, in (001) twist GBs under most irradiation conditions.

6.2 Microstructural evolution of {001} twist GBs under interstitial flux

As we have determined that interstitials accumulation in (001) twist GBs, it is of critical importance to explore how GBs evolve to accommodate these defects. To model long term evolution of GBs under defect accumulation, here we employ the grand canonical Monte Carlo (GCMC) simulation combined with molecular dynamics as implemented in LAMMPS. In GCMC, a C or Si atom is tentatively loaded to a random position in a predefined zone, and then the energy of the loaded atom in that position is calculated and compared with a predefined external chemical potential μ. The lower energy of the loaded atom with respect to μ, the higher chance this loading event will be accepted. Therefore, atoms are more likely to be loaded on energy favorable sites in a predefined zone by using GCMC. This feature makes GCMC a great tool to explore long term evolution of GBs under defect accumulation if we assume defects can have enough time to diffuse to low energy sites in the GB plane (validated later in Section 4.2.3). In order to relax the structure after loading interstitials, we run GCMC together with molecular dynamic simulation. In implementation, we run fixed volume MD simulations at a constant temperature, and every N timesteps the GCMC code is called M times to load interstitials. The loading zone for GCMC is set as a 1 nm thick slab centered at GB. The values of μ and frequency of GCMC loading (M/N) are changed from case to case in our simulations to adjust the loading rate as well as the stoichiometry of loaded C/Si atoms. However, loading a large amount of interstitials into a fixed volume supercell can lead to stress build up which in turn can

affect GB evolution in the long run. To relax the accumulated stress, we shut down GCMC for 1 ps in every 10 ps and run grand canonical simulation (NPT) within this 1 ps. Then GCMC is resumed with fixed volume supercell whose stress is literally relaxed to a small magnitude. The alternating runs of GCMC+MD and NPT can ensure continuous defect loading at energy favorable sites, structure relaxation as well as stress relaxation.

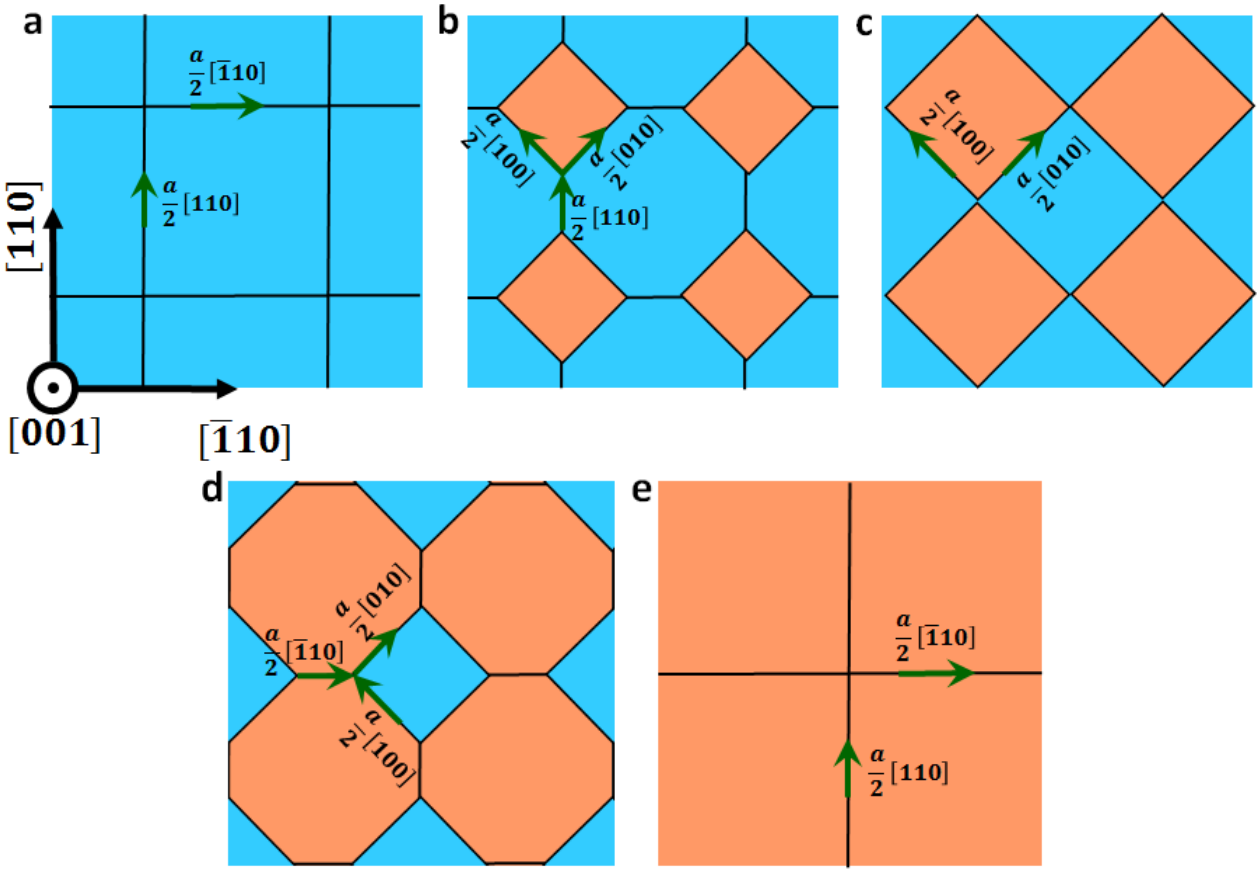

Figure 6-3 | Loop nucleation and extension in {001} twist GBs under interstitial flux. Black lines represent dislocations, and green arrows represent the screw component of Burger vector of each segment.

By loading interstitials onto the GB plane, we found (001) twist GBs accommodate interstitials by nucleation and extension of interstitials loops. Snapshots of simulation trajectories

are shown in Figure S22 in Appendix A4 and here we use a schematic drawing to better demonstrate the evolution process. Starting from an intact GB (Figure 6-3a), the first set of interstitials segregated to GBs quickly get trapped at MDIs because of the low segregation energy at these sites. As interstitials accumulate at MDIs, they reorganize to nucleate dislocation loops in square shape (origin squares in Figure 6-3b). The edges of the loop are mixed dislocation with edge component of $\vec{B}_E = \frac{a}{2}[001]$ and screw component of $\vec{B}_S = \frac{a}{2}[010]$ or $\frac{a}{2}[100]$. The edge component comes from the nature of an interstitial loop lying in (001) plane. The screw component (green arrows and labels in Figure 6-3) is necessary to accommodate the twisting angle between top and bottom crystals. Screw components of Burgers vector of dislocations connected at each MDI are balanced, as shown by the example in Figure 6-3b. With more and more interstitials attached to interstitial loops, these loops extend (Figure 6-3c) and connect with each other (Figure 6-3d) to reproduce the pure screw dislocations with $\vec{B} = \frac{a}{2}[110]$ or $\frac{a}{2}[\bar{1}10]$. These loops continue to absorb interstitials until a complete (001) plane is grown in this way (Figure 6-3e). Staring from the GB structure in Figure 6-3e, interstitials segregated to GB can nucleate loops at MDIs again (blue squares in Figure 6-3d). These loops then extend (blue squares in Figure 6-3c and Figure 6-3b) to grow a complete (001) plane (Figure 6-3a).

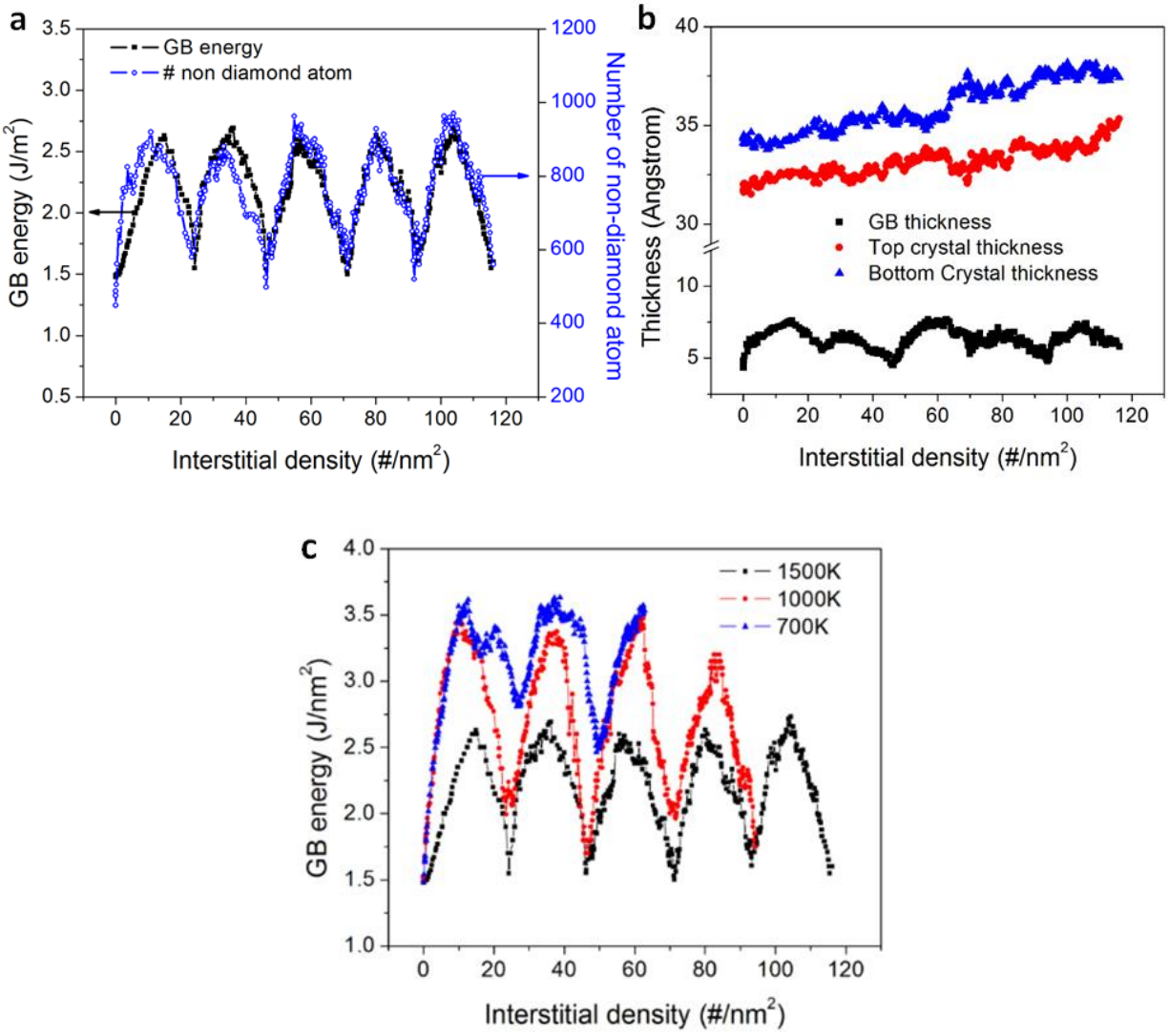

Figure 6-4 | The repeating pattern in {001} twist GB evolution under interstitial flux. **a**, GB energy and number of non-diamond atoms; **b**, GB, top and bottom crystal thickness; **c**, GB energy change at different temperatures.

The pattern of absorbing interstitials by loop nucleation and extension can also be characterized in terms of GB energy, disorder magnitude, and GB thickness, shown in Figure 6-4. The disorder magnitude is represented by the number of atoms with at least one nearest neighbor atom displaced from cubic diamond lattice. These atoms are termed as non-diamond here and they are identified by the structural analysis function implemented in Ovito[193]. GB thickness is

calculated as 2 times of the standard deviation of the coordination of these non-diamond atoms along the thickness dimension (perpendicular to the GB plane). As we can see from Figure 6-4a and 6-4b, GB energy, number of non-diamond atoms and GB thickness follow a clear pattern as a function of the density of loaded interstitials. Because crystal layers grow from loop nucleation, the thickness of top and bottom crystals grows linearly with the density of interstitial loaded. This implies {001} twist GBs are un-saturatable in absorbing interstitials if the stress build up from crystal growth can be relaxed.

Because loop nucleation and extension are both kinetic processes, they depend highly on the loading rate of interstitials and the temperatures to anneal the supercell. To exam whether the pattern observed above is generally valid for a wide range of sceneries, we repeated the simulations at different temperatures and loading rates. The principle of adjusting temperature and loading rate here is to use low loading rate at low temperature. The results on GB energy change with interstitial density are shown in Figure 6-4c. At lower temperatures, the intermediate states (e.g., at the density of $10/nm^2$) and the ground state (e.g., at the density of $21/nm^2$) have higher GB energies than those relaxed at higher temperatures. This is because the slow kinetics at low temperature cannot fully optimize the structure within the limited timescale of MD simulations. However, the repeatable pattern is clear at temperature as low as 700 K. This implies loop nucleation and extension induced by interstitial flux to {001} twist GBs is generally valid over a wide range of temperatures. We also exanimated how the stoichiometry of interstitial flux can affect GB microstructural evolution. We find this pattern is valid for a wide range of stoichiometry from C:Si = 1:1 to only C interstitial loading. A high concentration of C antisites can accumulate at GBs when more C interstitials than Si interstitials are loaded onto GBs.

6.3 Defect segregation and kinetics at {111} twist GBs

The common structure of small angle {111} twist GB is shown in Figure 6-5a using $(11\bar{1})$ Σ507 θ=4.4° as an example. The GB plane is composed of alternating triangular stacking fault (SF) regions and cubic regions (3C). The SF regions are formed due to the dissociation of primitive screw dislocations (thin black lines in Figure 6-5a) into partials (thin green lines in the same figure). The dislocation reaction of the dissociation process is:

$$\frac{a}{2}[\bar{1}10]\ (primitive\ screw) \rightarrow \frac{a}{6}[\bar{1}21]\ (partial) + \frac{a}{6}[\bar{2}1\bar{1}]\ (partial) \qquad (6\text{-}4)$$

These stacking fault are intrinsic SF with stacking sequence of (ABC)(BC)(ABC) along [111] direction. Similar structure has been reported in experimental observation and simulations of fcc metals with low SF energy, such as Cu[194-195]. The SF energy in 3C-SiC is negative[196-197], so it is energy favorable to form SF and partial dislocations at (111) twist GBs in SiC. GBs with different twisting angles differ in the distance between parallel primitive screw dislocations. Again, the distance can be determined by the twisting angle by using Equation (6-1).

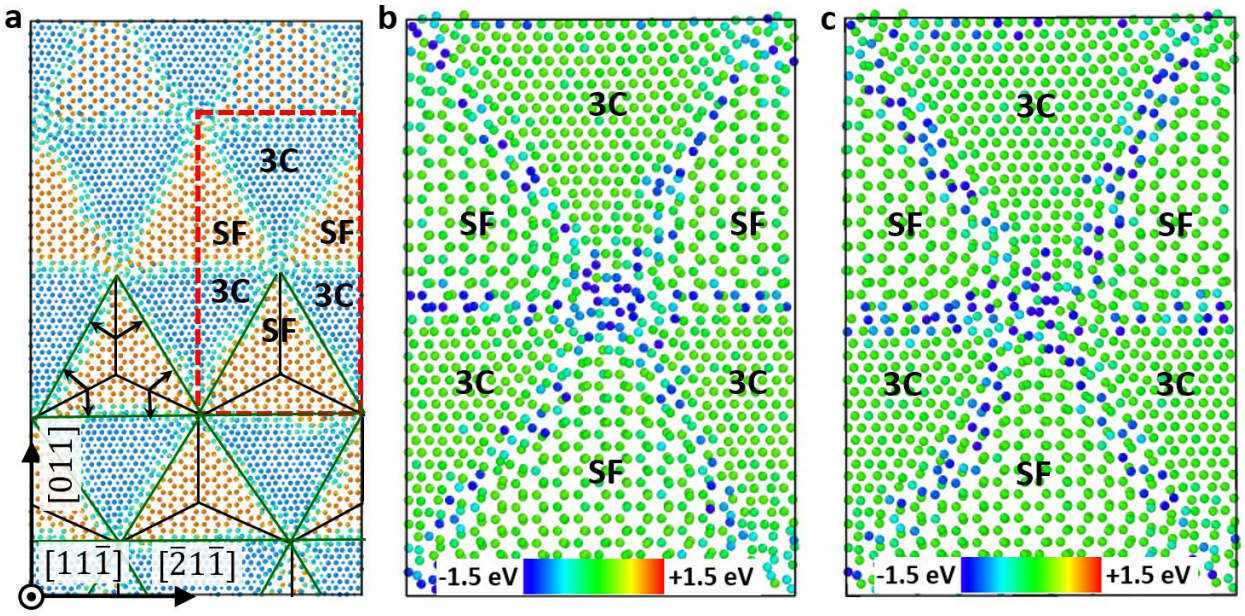

Figure 6-5 | Atom structure and defect segregation energy at $(11\bar{1})$ Σ507 θ=4.4° twist GBs. **a**, GB structure; **b**, C interstitial segregation energy; **c**, Si interstitial segregation energy. In panel **a**, atoms in blue have cubic SiC (3C) structure, atoms in red are in stacking fault, and atoms in cyan are on partial dislocations. Thin black lines represent the $\frac{a}{2}\langle 110\rangle$ screw dislocations before faulting, thin green lines represent the $\frac{a}{6}\langle 211\rangle$ partials after faulting. The black arrows show the formation of stacking faults by dissociation of primitive screw dislocations into partial dislocations. The red dashed square shows the region where interstitial segregation energies are calculated and shown in panel **b** and **c**.

With the most stable structure identified, we now exam the segregation energy of interstitials at different sites at these GBs. The results are shown in Figure 6-5b and 6-5c for C and Si interstitials in Σ507 GB. It is clear partials and MDIs are strong traps for interstitials and MDIs are stronger sinks. To be more specific, segregation energy of C interstitials is approximate -0.27 eV in SF, (-1.4,-1.0) eV on partial dislocations, and (-1.9, -1.3) eV at MDIs. Segregation energy of Si interstitials is zero at both 3C and SF regions, (-2.0, -1.2) eV on partial dislocations, and (-

2.1, -3.1) at MDIs. Here we provide a range of segregation energy on partials and MDIs because the atomic structures of partials and MDIs vary slightly from site to site. Similar as {001} twist GBs, we found a deep potential well at MDIs for both C and Si interstitials.

Here we perform a similar analysis on t_{seg}, t_{trap}, and t_{sink} as detailed in R1.1 to investigate defect accumulation at {111} twist GBs. First, t_{seg} is the same as that in {001} twist GBs because it is independent on GB characters. Second, t_{trap} is recalculated by using the inter-MDI distance in {111} twist GBs. Then, we adjust the inter-MDI diffusion 1-D KMC model with energy landscape in {111} twist GBs to determine the inter-MDI diffusion time τ. Finally, a two-dimensional random walk simulation on triangular mesh of GB plane is performed to obtain number of inter-MDI hops N_{step} for interstitials to diffuse to sinks. With τ and N_{step} ready, we can obtain the time for interstitial to diffuse to other sinks t_{sink}. Values of t_{seg}, t_{trap}, and t_{sink} under various radiation conditions are detailed in Table S4 in Appendix A4. Similar as {001} twist GBs, interstitials are found to quickly diffuse to dislocation grid or MDIs because $t_{trap} << t_{seg}$. At low temperature (below 873 K) and high radiation dose rate (higher than 10^{-4} dpa/s) in SiC with large grains (diameter > 100 nm), we found $t_{seg} << t_{sink}$. This is because the deep potential well at MDIs traps interstitials at low temperature and retards the overall mobility along the dislocation grid to reach sinks. This can lead to interstitial accumulation at GB plane and therefore it is necessary to investigate microstructural evolution of defect-loaded GBs. In nano-grain SiC (diameter <100 nm) irradiated at high temperature (over 873 K) and low dose rate (lower than 10^{-4} dpa/s), t_{sink} is comparable or even smaller than t_{seg}. In these cases, defects segregated to GBs can quickly diffuse along the grid to reach other sinks. Once again, we see multiple roles of GBs in annihilating defects under different radiation conditions.

6.4 Microstructural evolution of {111} twist GBs under interstitial flux

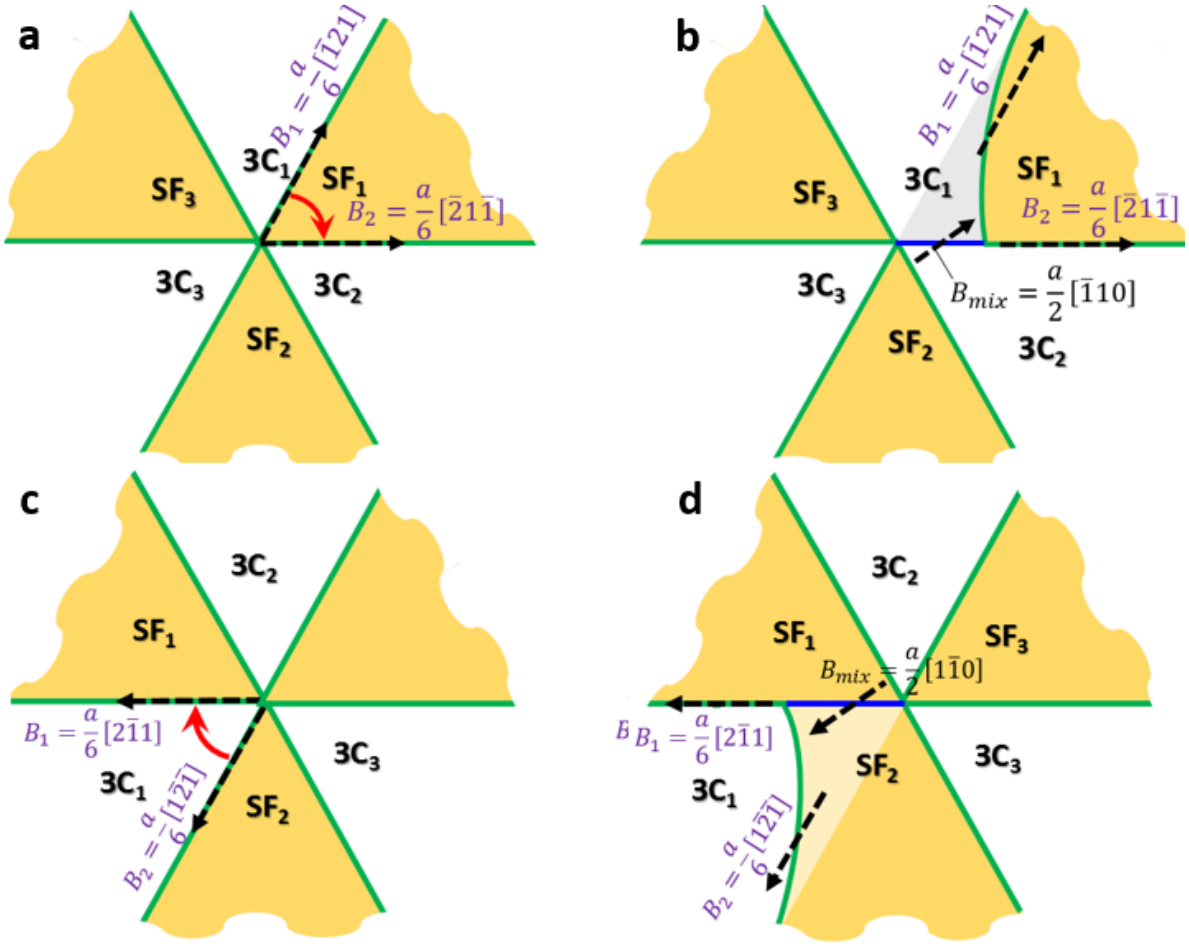

Figure 6-6 | Unfaulting and faulting process to form mixed dislocations in $(11\bar{1})$ twist GB. a and b, unfaulting process; c and d, faulting process. Green lines are partial dislocations, and blue lines are the newly formed mixed dislocations. Black dashed arrows show the direction of Burgers vector of each dislocation segment. Red arrows in panel a and c show the glide direction of one partial towards another partial.

To explore how {111} twist GBs evolve to accommodate these defects, we employ the same GCMC and MD method to load stoichiometric C/Si interstitial to the interface. We found (111) twist GBs absorb interstitials by the climb of mixed dislocations. The mixed dislocations are formed either by shrinkage of SF (or unfaulting, shown in Figure 6-6a and 6-6b) or by extension of SF (or faulting, shown in Figure 6-6c and 6-6d). In the unfaulting process, one partial dislocation glides towards a neighboring partial dislocation that is separated by SF (glide direction is shown by the red arrow in Figure 6-6a), and therefore unfault this SF region. This produces a mixed dislocation with both edge and screw components. The dislocation reaction of this process is:

$$\frac{a}{6}[\bar{1}21]\ (partial) + \frac{a}{6}[\bar{2}1\bar{1}](partial) \rightarrow \frac{a}{2}[\bar{1}10]\ (mixed\ dislocation) \qquad (6\text{-}5)$$

and the edge and screw components of the mixed dislocation is demonstrated as:

$$\frac{a}{2}[\bar{1}10]\ (mixed\ dislocation) = \frac{a}{4}[011]\ (edge) + \frac{a}{4}[\bar{2}1\bar{1}]\ (screw) \qquad (6\text{-}6)$$

Due to the edge component of the mixed desolation, it can climb along $[11\bar{1}]$ direction to absorb interstitials. In the faulting process, one partial dislocation glides towards a neighboring partial dislocation that is separated by 3C region (glide direction is shown by the red arrow in Figure 6-6c), and therefore fault this 3C region to produce SF. Similarly, this process produces a mixed dislocation that can climb along $[11\bar{1}]$ direction to absorb interstitials. It is important to note that the faulting and unfaulting process is energy favorable only when interstitials are presented at GB. This is because the newly formed mixed dislocation can climb to absorb interstitials so the system energy can be lowered by moving interstitials to grow crystal there. However, because primitive dislocations have higher elastic energy than dissociated partials so these processes are energy unfavorable without the presence of interstitials.

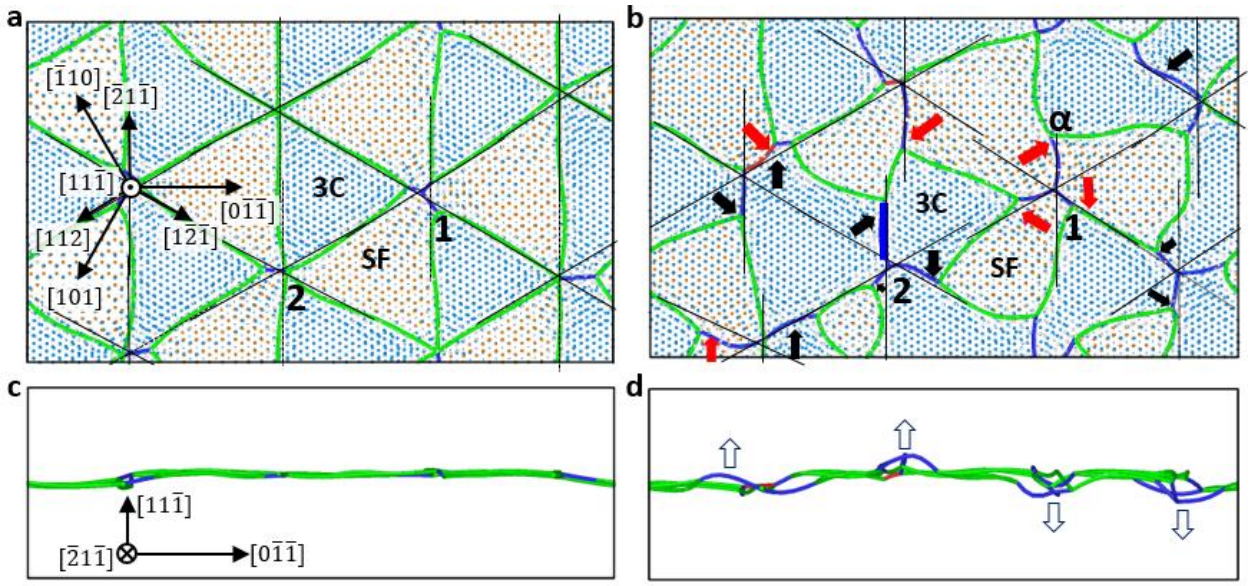

Figure 6-7 | Evidence of faulting and unfaulting process at $(11\bar{1})$ twist GBs induced by interstitial loading. **a**, GBs without interstitial loading; **b**, GBs loaded with 215 C interstitials; **c** and **d**, in-plane view of GBs in panel **a** and **b**. Green lines are partial dislocations with Burgers vector of $\frac{a}{6}\langle 211\rangle$ and blue lines are primitive dislocations with Burgers vector of $\frac{a}{2}[011]$. Thin black lines serve as a reference to note crystal directions at each MDI. The red and black arrows in panel **b** show evident faulting and unfaulting processes to form mixed dislocations as detailed in Figure 6-6. The thick blue line in panel **b** highlights the mixed dislocation segment whose atomic structure is detailed in Figure 6-8. The unfilled arrows in panel **d** show the climbing directions of mixed dislocations. Dislocations are identified and visualized by dislocation analysis implemented in Ovito[134].

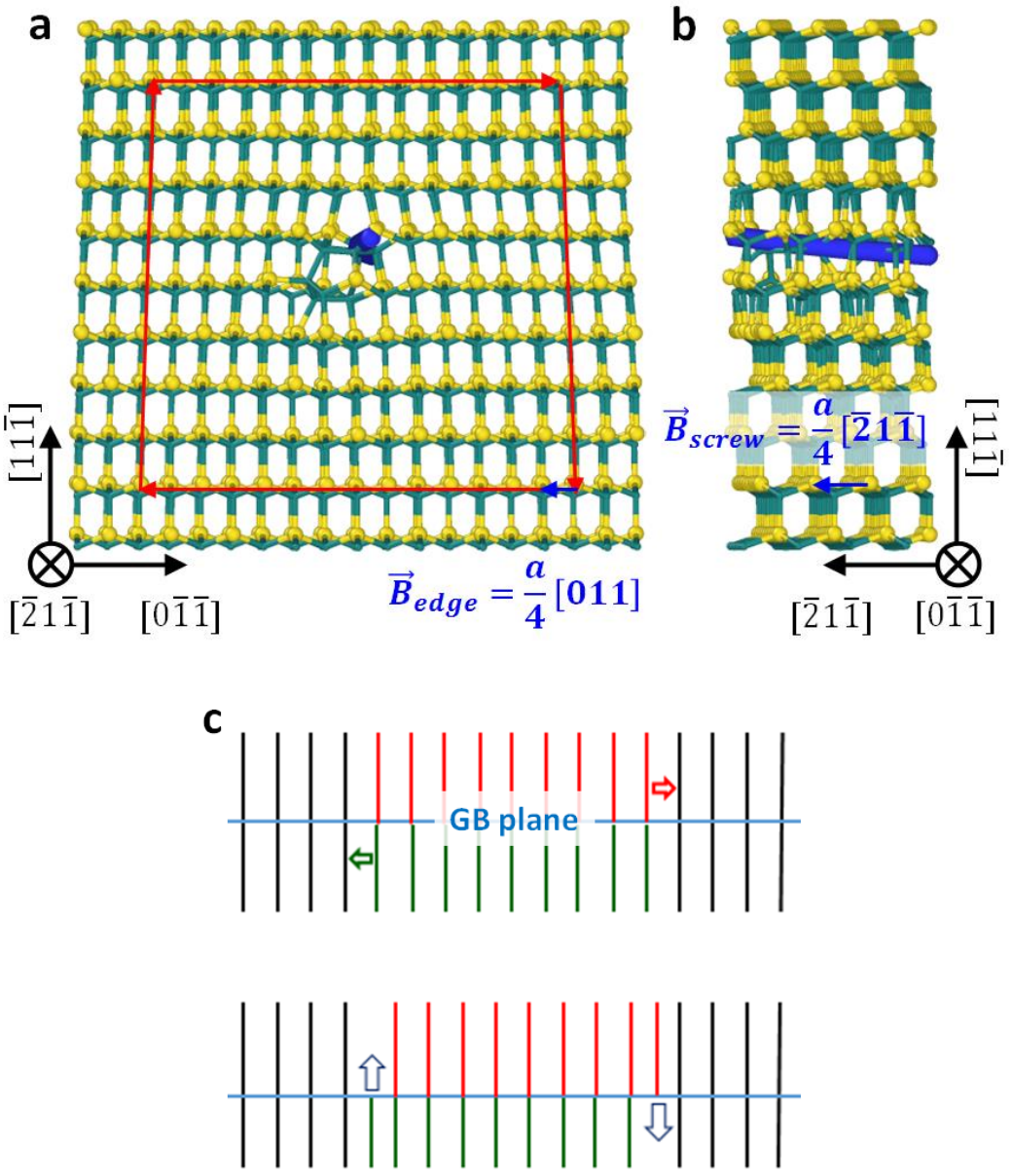

Figure 6-8 | Atom structure around the dislocation segment highlighted by thick blue line in Fix. 8b. **a**, Projection along the dislocation line direction; **b**, Projection perpendicular to the dislocation line; **c**, Formation of dislocation dipole by shifting atom planes locally. In panel **a** and **b**, large yellow spheres are Si, small green spheres are C, the blue line is the dislocation segment, and the blue arrow is the Burgers vector determined from a Burgers circuit labeled by the red arrows.

Evidence of formation and climb of mixed dislocations is shown in Figure 6-7 and Figure 6-8. Network of partial dislocations in an intact GB is shown by green lines in Figure 6-7a, and in-plane view of the GB is shown in Figure 6-7c. The structure of GBs loaded with 215 C interstitials (density: 1.93 #/nm^2) and in-plane view are shown in Figure 6-7b and 6-7d. It is clear GB structure changes significantly due to the load of interstitials, and this change is induced by the formation and climb of mixed dislocations. One example is MDI labeled as "1" in Figure 6-7a and 6-7b where all initial 3C regions around it were faulted to become SF (this process is shown by red arrows in Figure 6-7b). The newly formed dislocations (blue lines in Figure 6-7b) aligns along <211> directions but not <011> which is the direction of their Burgers vector. This implies the nature of mixed dislocation. Another example is MDI labeled as "2" where all initial SF regions around it were unfaulted to be 3C regions (this process is shown by black arrows in Figure 6-7b). The atomic structure around the mixed dislocation segment is highlighted by the thick blue line in Fix. 8b is shown in Figure 6-9a and 6-9b. This mixed dislocation is formed by the reaction in Equation (6-5) and its edge and screw component are shown in Equation (6-6). From the projection along dislocation line direction in Figure 6-8a, we can easily identify an edge vector of $\frac{a}{4}[011]$ by drawing a Burgers circuit around the dislocation core. In another projection perpendicular to the dislocation line, the screw vector of $\frac{a}{4}[\bar{2}1\bar{1}]$ can be clearly determined from the Burgers vector (blue arrow). All evident faulting and unfaulting process are labeled by red and black arrows in Figure 6-7b so readers can exam them to picture the GB structure evolution.

These newly formed mixed dislocation climbs along $[11\bar{1}]$ or $[\bar{1}\bar{1}1]$ direction out of the GB plane to accommodate interstitials, as labeled by the empty arrows in Figure 6-7d. It is important to note that some mixed dislocations climb upwards along $[11\bar{1}]$ while others climb downwards

along $[11\bar{1}]$, as shown in Figure 6-7d. This is because as the faulting or unfaulting process produces one mixed dislocation, it has to be compensated at another position by a similar process to produce a mixed dislocation climbing at the opposite direction. This literately likes the formation of a dislocation dipole by shifting parts of top and bottom crystals locally, as shown in Figure 6-8e. Another nature of the mixed dislocation is that at least one end of the mixed dislocation is pinned to the SF plane. To be more specific, the end connected with two partials separating SF and 3C regions (e.g., point α in Figure 6-7b) is pinned to the SF plane. This end can only move if the SF plane is shifted upwards or downwards due to thermal vibration or stress. The other end, if connected with only mixed dislocations (e.g., MDI labeled as "1" in Figure 6-7b), can move due to the collective climb of these connected dislocations. This is the reason why these mixed dislocations develop curvatures in the in-plane view and therefore increase in dislocation length as they climb to absorb interstitials.

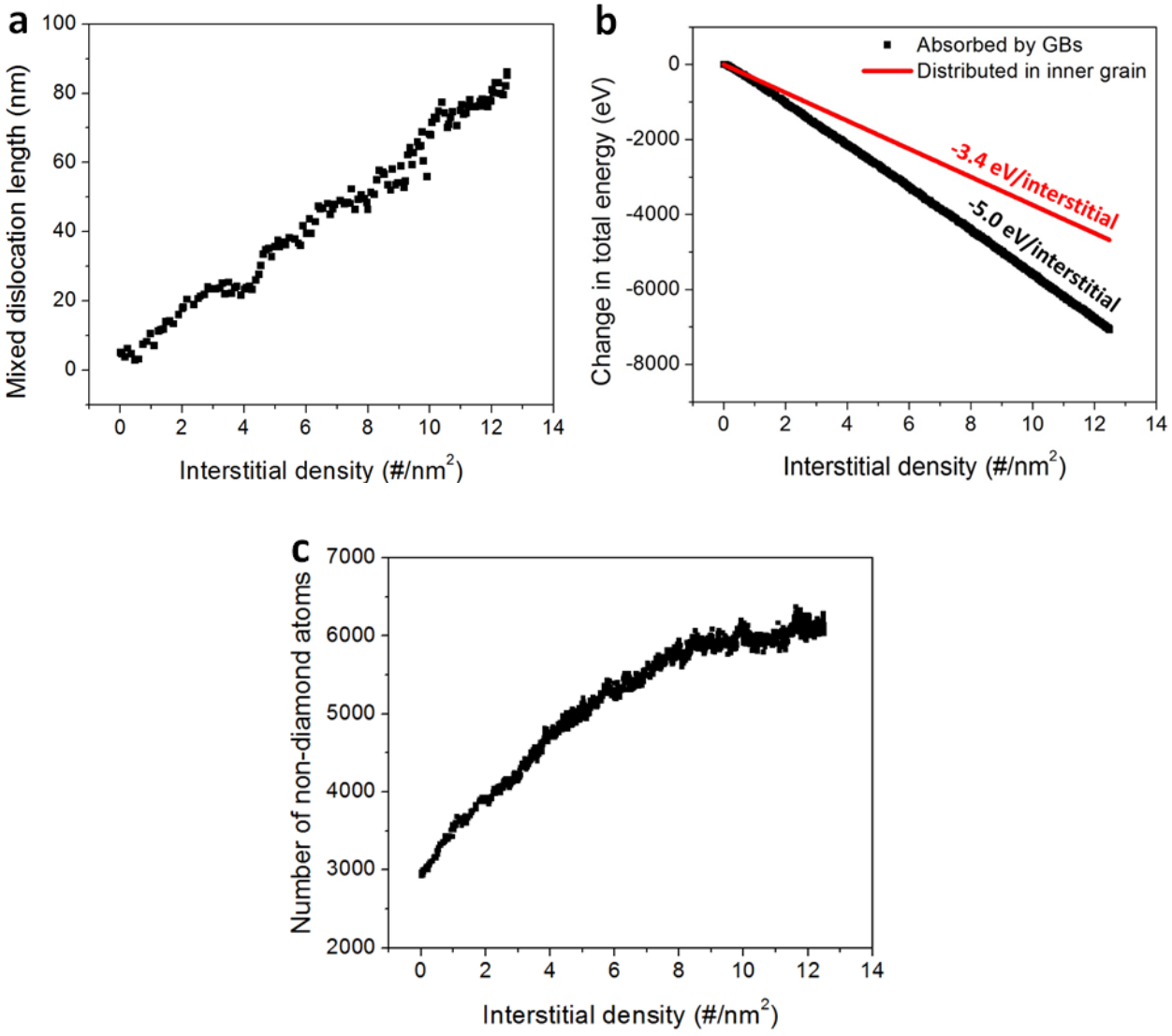

Figure 6-9 | Long term evolution of {111} twist GBs under interstitial flux. **a**, length of mixed dislocations; **b**, change in supercell energy; **c**, number of non-diamond/SF atoms.

The long term evolution of {111} twist GBs to absorb interstitials is characterized and shown in Figure 6-9. Figure 6-9a shows a linear relationship between mixed dislocation length and loaded interstitial density. This is an evidence to support that mixed dislocations climb to absorb interstitials. Because attaching of interstitials to dislocations grows lattice, it is always energy favorable for interstitials diffuse to these dislocations rather than stay in the lattice. This preference is quantified in Figure 6-9b, where changes in bi-crystal supercell energy as a

function of loaded interstitial density are plotted for two cases. In the case shown by black squares, interstitials are absorbed by these mixed dislocations, obtained from interstitial loading simulations. In the other case shown by the red line, interstitials are randomly distributed in bulk without interactions among them. It is evident that segregation to GBs and attachment to dislocations are more energy favorable than staying in bulk by a magnitude of approximate 1.6 eV/interstitial. This implies the structural evolution in {111} twist GBs will not lead to saturation in absorbing interstitials. Furthermore, extension of dislocations out the GB plane will not lead to amorphization of the interface in the long run. Here we characterize amorphization by the number of non-diamond and non-SF atoms. Atoms in SF are excluded because SF is stable and even energy favorable in cubic SiC[196-197]. The trend between non-diamond/SF atoms and number density of loaded interstitials are shown in Figure 6-9c. In the beginning of loading, the number of non-diamond/SF atoms increases at a high rate because the formation of mixed dislocations whose core deviates from diamond and SF structure. As a certain amount of mixed dislocations is developed, the increase rate reduces gradually because interstitials are converted to crystal lattice by dislocation climb. The climb process do not significantly increase the number of disordered atoms. Besides, by varying the stoichiometry of C/Si atoms loaded onto the GB, we found the similar trend as reported for C:Si = 1:1 loading. Again, C antisites can accumulate when more C interstitials than Si interstitials are loaded.

6.5 Discussions and conclusions

First of all, we found MDIs play a critical role in understanding defect kinetics in twist GBs and GB structure evolution. This is because MDIs are strong traps for interstitials. On the one hand, the deep potential well at MDIs raises the barrier for defect diffusion and therefore retards the mobility of defects along dislocation grids. On the other hand, the deep potential wells at

MDIs attract defects and initiate structural evolution there. Analysis on defect diffusivity at GBs and defect flux to GBs shows twist GBs play different roles in annihilating defects in various radiation conditions. In large grain size SiC irradiated at low temperature and low dose rate, defects don't have high thermal energy to actively escape from MDIs. So there are high chances that defects cluster at MDI and GBs annihilate these defects by structural evolution. While in small grain size SiC irradiated at high temperature and low dose rate, defects can frequently hop among MDIs due to the increased thermal energy. In this case, twist GBs mainly serve as a diffusion channel for defects to reach other sinks.

Second, we found both {001} and {111} twist GBs have to form dislocations with edge component in order to absorb interstitials. This is because screw dislocations naturally developed in twist GBs cannot climb but edge dislocations can. If dislocations with edge component can form in GBs, they can climb to grow lattice by absorbing point defects. Different twist GBs differ in the way of forming edge dislocations. In {001} twist GBs, interstitial loops nucleate at MDIs in the GB plane and dislocations around the edge of loops have edge component. In {111} twist GBs, one partial dislocation glide toward another partial to form a mixed dislocation with both edge and screw component. This process can either fault or unfault the region between the two partials. A similar behavior of {111} twist GB was reported in Cu[119]. Upon loading a little amount of vacancies, the author found vacancies segregate to MDIs and are delocalized by the shrinkage of SF area. Here we advances the understanding of this process by providing detailed analysis on dislocation reactions and the afterward evolution of GBs upon further defect loading. Given the two twist systems in SiC exanimated in this study and the {111} twist GB reported in Cu, we believe it is universal for twist GBs to develop dislocations with edge component in order to absorb point defects. The question how other twist GB systems such as {011} twist GBs or

even high angle twist GBs develop mixed dislocations to absorb point defects requires further investigation.

In summary, we investigated defect kinetics and long-term microstructural evolution of {001} and {111} twist GBs in SiC under interstitial flux. Dislocation networks and dislocation intersections in the GB plane are strong traps for both C and Si interstitials. Because of the deep potential well at dislocation intersections, point defect diffusion along the dislocation grid is retard and this can lead to defect accumulation at GBs under defect flux in the long run. By using a combination of grand canonical Monte Carlo and molecular dynamics, we revealed the structural evolution in both types of twist GBs. In {001} twist GBs, interstitials aggregate at dislocation intersections and nucleate interstitial loops lying on {001} plane. These loops can extend to absorb incoming interstitials from bulk until a full {001} f lattice plane grows at the interface. The initial screw dislocation grid is recovered in this way and new loops can nucleate and extend again from intersections. This repeating structural evolution enables {001} twist GBs to accommodate a huge amount of interstitials under irradiation. In {111} twist GBs, we found the faulting and unfaulting processes at dislocation intersections to form mixed dislocations with both edge and screw components. Interstitials are absorbed by the climb of these mixed dislocations out of the GB plane. The common feature of developing dislocations with edge component in both types of twist GBs suggests this could be a universal way for twist GBs to accommodate point defects. The continuous formation and climb of mixed dislocations imply twist GBs are unsaturatable sinks for radiation induced defects in SiC.

Chapter 7 Summary and Future Work

In this thesis, I have employed multiscale simulation techniques to investigate the long term evolution of radiation induced defects in SiC.

First of all, by programing and implementing an on-the-fly KMC model, I fully explored the migration behavior of the most stable carbon tri-interstitial cluster in SiC. It is found this cluster migrates with high barriers (minimum barrier 4.3 eV) and in a multistep process. With the high barriers detected, I show that the most stable cluster is immobile at temperatures below 1100 K, and that it only has limited diffusivity up to 1500 K. At temperatures beyond 1500 K, this cluster can be annihilated by dissociation into smaller clusters and single interstitials. Because this carbon tri-interstitial cluster is a basic building block for larger interstitial clusters in SiC, similar diffusion behavior is expected for larger clusters. Therefore, one can conclude that the thermal diffusivity of interstitial clusters in SiC is extremely low over a wide range of temperatures.

In collaboration with STEM scientists, we found tiny interstitial clusters can diffuse at room temperature under the influence of electron beam. It was experimentally verified that the athermal diffusion phenomenon is induced by the elastic collision between energetic electrons and cluster atoms. This is the first report of direct observation of radiation-induced diffusion of defect clusters in bulk materials in literature. A model was developed to predict the radiation induced diffusivity of clusters and it predicts diffusivity on the same order of magnitude with experimental measurements. This study implies thermally immobile clusters can diffuse under certain irradiation environments. The radiation induced mobility of cluster may lead to consequences such as cluster coalesces or diffuse to nearby sinks such as grain boundaries. The above studies on cluster diffusion provide important insights and parameters for other models

such as cluster dynamics to investigate microstructure evolution in SiC. In fact, with the knowledge of cluster diffusion in SiC demonstrated in this thesis, we now become able to predict cluster evolution in SiC with good agreement with experimental measurements.

The response of tilt and twist GBs to radiation induced defect fluxes to GBs has also been investigated to shed light on the radiation response of polycrystalline SiC. I first demonstrated the exact role of tilt GBs in annihilating defects in SiC under various radiation environments. I found that once interstitials have segregated to tilt GBs, pipe diffusion of defects in these GBs is slower than bulk diffusion. This is because the stretched interatomic distance at dislocation cores raises the migration barrier of interstitial dumbbells. Furthermore, I showed that the annihilation of interstitials at jogs has low activation energies and thus is a diffusion-controlled process. Jog nucleation from interstitial clusters is also found to happen with barriers no higher than the diffusion barrier of interstitials when cluster size is equal to or larger than four, regardless of its composition. Finally, a dislocation line model was developed to take into account defect flux to GBs, pipe diffusion of defects in tilt GBs, and interactions between defects and jogs. This model reveals the multiple roles of tilt GBs in annihilating radiation-induced defects in SiC. It predicts that tilt GBs mainly serve as a diffusion channel for defects to reach other sinks like surface when the defect accumulation rate at boundaries is low. The diffusion channel regime occurs in nano-crystalline materials with small grain diameter (smaller than 100 nm) irradiated under low dose rate (lower than 10^{-3} dpa/s) at high temperature (higher than 873 K). In other cases, when the accumulation rate is high, most of the defects diffused to tilt GBs are annihilated by dislocation climb.

The response of {001} and {111} twist GBs to fluxes of radiation induced defects was also investigated. Screw dislocation networks and dislocation intersections in twist GB plane are

found to be strong traps for both C and Si interstitials. Because of the deep potential wells at dislocation intersections, point defect diffusion along the screw dislocation grid is retard and this can lead to defect accumulation at GBs under many circumstances. By using a combination of grand canonical Monte Carlo and molecular dynamics, I revealed the structural evolution of both types of twist GBs to annihilate accumulated interstitials. In {001} twist GBs, interstitials aggregate at dislocation intersections and nucleate interstitial loops lying at the interface. These loops can extend to absorb incoming interstitials, and this process leads to the continuous growth of {001} lattice plane at the interface. In {111} twist GBs, I found the formation of mixed dislocations with both edge and screw components. This is enabled by the faulting and unfaulting of stacking fault initiated at dislocation intersections. Interstitials are absorbed by the climb of these mixed dislocations out of the GB plane. The common feature of climbing dislocations with edge components in both types of twist GBs suggests this is a universal way for twist GBs to accommodate point defects. Because of the continuous formation and climb of dislocations, twist GBs can behave as unsaturatable sinks to radiation induced defects.

A future work continuing the current research on GBs would be investigating how defects are transported and accommodated in general GBs with both tilt and twist features. General GBs are common in polycrystalline materials so their response to defect fluxes under irradiation is of vital importance. The methods developed in studies on tilt and twist GBs such as KMC models and grand canonical Monte Carlo simulations can be readily adapted to investigate response of general GBs to defect fluxes. Another interesting topic to investigate is the radiation response of large-angle tilt and twist GBs. In large-angle GBs, the distance between dislocation cores are so small that dislocation cores overlap with each other. These GB structures can differ significantly from small-angle tilt/twist GBs and so does their radiation response. Furthermore, GBs' structure

evolution under defect fluxes predicted by simulations can potentially be verified by experiments. For instance, by fabricating bi-crystal SiC samples properly, pure tilt/twist GBs can be obtained. Investigation of radiation effects on these bi-crystal samples will be extremely helpful to understand how GBs annihilate defects and provide comparison to simulation predictions. These works can help to develop a full understanding of GBs' sink strength in SiC and therefore improved resistance to radiation damages by interfacial engineering.

References

1. Pensl, G.; Choyke, W., Electrical and optical characterization of SiC. ***Physica B: Condensed Matter*** 1993, *185* (1-4), 264-283.

2. Abderrazak, H.; Hmida, E. S. B. H., *Silicon carbide: Synthesis and properties*. ***INTECH Open Access Publisher*****:** 2011.

3. Katoh, Y.; Snead, L. L.; Szlufarska, I.; Weber, W. J., Radiation effects in SiC for nuclear structural applications. ***Curr. Opin. Solid St. M.*** 2012, *16* (3), 143-152.

4. Snead, L. L.; Nozawa, T.; Katoh, Y.; Byun, T.-S.; Kondo, S.; Petti, D. A., Handbook of SiC properties for fuel performance modeling. ***J. Nucl. Mater.*** 2007, *371* (1), 329-377.

5. Azevedo, C., Selection of fuel cladding material for nuclear fission reactors. ***Eng. Fail. Anal.*** 2011, *18* (8), 1943-1962.

6. Kohyama, A.; Kishimoto, H., SiC/SiC composite materials for nuclear applications. ***Nucl. Safety Simu.*** 2013, *4* (2), 72-79.

7. Iveković, A.; Novak, S.; Dražić, G.; Blagoeva, D.; de Vicente, S. G., Current status and prospects of SiC f/SiC for fusion structural applications. ***J. Eur. Ceram. Soc.*** 2013, *33* (10), 1577-1589.

8. Tan, L.; Allen, T. R.; Hunn, J. D.; Miller, J. H., EBSD for microstructure and property characterization of the SiC-coating in TRISO fuel particles. ***J. Nucl. Mater.*** 2008, *372* (2), 400-404.

9. Hosemann, P.; Martos, J.; Frazer, D.; Vasudevamurthy, G.; Byun, T. S.; Hunn, J. D.; Jolly, B. C.; Terrani, K.; Okuniewski, M., Mechanical characteristics of SiC coating layer in TRISO fuel particles. ***J. Nucl. Mater.*** 2013, *442* (1), 133-142.

10. Miller, G.; Petti, D.; Maki, J. In *Development of an integrated performance model for triso-coated gas reactor particle fuel*, 1st International Topical Meeting on High Temperature Reactor Technology (HTR), Petten, Netherlands, ***Citeseer***: 2002.

11. Knorr, J.; Lippmann, W.; Reinecke, A.-M.; Wolf, R.; Kerber, A.; Wolter, A., SiC encapsulation of (V) HTR components and waste by laser beam joining of ceramics. ***Nucl. Eng. Des.*** 2008, *238* (11), 3129-3135.

12. Kerber, A.; Knorr, J., SiC Encapsulation of High-Level Waste for Long-Term Immobilization. ***Atw. Internationale Zeitschrift fuer Kernenergie*** 2013, *59* (1), 8-13.

13. O'Donnell, C. Advancing nuclear fuel: an important milestone in accident-tolerant fuel. https://www.inl.gov/article/advancing-nuclear-fuel/.

14. Honorato, E. L. The High Temperature Reactor and the TRISO coated fuel particle. https://eddiehonorato.wordpress.com/tag/triso-coated-fuel-particle/.

15. Motta, A. T.; Couet, A.; Comstock, R. J., Corrosion of zirconium alloys used for nuclear fuel cladding. ***Ann. Rev. Mater. Res.*** 2015, *45*, 311-343.

16. Pint, B. A.; Terrani, K. A.; Brady, M. P.; Cheng, T.; Keiser, J. R., High temperature oxidation of fuel cladding candidate materials in steam–hydrogen environments. ***J. Nucl. Mater.*** 2013, *440* (1), 420-427.

17. Hirayama, H.; Kawakubo, T.; Goto, A.; Kaneko, T., Corrosion behavior of silicon carbide in 290 C water. ***J. Am. Ceram. Soc.*** 1989, *72* (11), 2049-2053.

18. Kim, W.-J.; Hwang, H. S.; Park, J. Y.; Ryu, W.-S., Corrosion behaviors of sintered and chemically vapor deposited silicon carbide ceramics in water at 360 C. ***J. Mater. Sci. Lett.*** 2003, *22* (8), 581-584.

19. Snead, L.; Zinkle, S.; White, D., Thermal conductivity degradation of ceramic materials due to low temperature, low dose neutron irradiation. ***J. Nucl. Mater.*** 2005, *340* (2), 187-202.

20. Li, J.; Porter, L.; Yip, S., Atomistic modeling of finite-temperature properties of crystalline β-SiC: II. Thermal conductivity and effects of point defects. ***J. Nucl. Mater.*** 1998, *255* (2), 139-152.

21. Crocombette, J.-P.; Proville, L., Thermal conductivity degradation induced by point defects in irradiated silicon carbide. ***Appl. Phys. Lett.*** 2011, *98* (19), 191905.

22. Wojdyr, M.; Khalil, S.; Liu, Y.; Szlufarska, I., Energetics and structure of <001> tilt grain boundaries in SiC. ***Model. Simul. Mater. Sci.*** 2010, *18* (7), 075009.

23. Snead, L. L.; Katoh, Y.; Connery, S., Swelling of SiC at intermediate and high irradiation temperatures. ***J. Nucl. Mater.*** 2007, *367*, 677-684.

24. Kondo, S.; Koyanagi, T.; Hinoki, T., Irradiation creep of 3C–SiC and microstructural understanding of the underlying mechanisms. ***J. Nucl. Mater.*** 2014, *448* (1), 487-496.

25. Audren, A.; Benyagoub, A.; Thomé, L.; Garrido, F., Ion implantation of Cs into silicon carbide: Damage production and diffusion behaviour. ***Nucl. Instrum. Meth. B*** 2007, *257* (1), 227-230.

26. Audren, A.; Benyagoub, A.; Thome, L.; Garrido, F., Ion implantation of iodine into silicon carbide: Influence of temperature on the produced damage and on the diffusion behaviour. ***Nucl. Instrum. Meth. B*** 2008, *266* (12), 2810-2813.

27. Friedland, E.; Malherbe, J.; Van der Berg, N.; Hlatshwayo, T.; Botha, A.; Wendler, E.; Wesch, W., Study of silver diffusion in silicon carbide. ***J. Nucl. Mater.*** 2009, *389* (2), 326-331.

28. Demkowicz, P.; Hunn, J. D.; Morris, R. N.; Harp, J.; Baldwin, C. A.; Winston, P.; Ploger, S.; Montgomery, F. C. *Preliminary evaluation of fission product release from AGR-1 coated particles*; ***Oak Ridge National Laboratory (ORNL)***: 2012.

29. Shrader, D.; Khalil, S. M.; Gerczak, T.; Allen, T. R.; Heim, A. J.; Szlufarska, I.; Morgan, D., Ag diffusion in cubic silicon carbide. ***J. Nucl. Mater.*** 2011, *408* (3), 257-271.

30. Ko, H.; Deng, J.; Szlufarska, I.; Morgan, D., Ag diffusion in SiC high-energy grain boundaries: Kinetic Monte Carlo study with first-principle calculations. ***Comput. Mater. Sci.*** 2016, *121*, 248-257.

31. Khalil, S.; Swaminathan, N.; Shrader, D.; Heim, A. J.; Morgan, D. D.; Szlufarska, I., Diffusion of Ag along Σ3 grain boundaries in 3C-SiC. ***Phys. Rev. B*** 2011, *84* (21), 214104.

32. Stcmton, D.; Angeiini, P.; Caputo, A. J.; Lackey, W., Coating of crystalline nuclear waste forms to improve inertness. ***J. Am. Ceram. Soc.*** 1982, *65* (8), 394-398.

33. Stinton, D. P.; Lackey, W. J.; Aneglini, P., Immobilization of radioactive cesium in pyrolytic-carbon-coated zeolite. ***J. Am. Ceram. Soc.*** 1983, *66* (6), 389-392.

34. Bryan, D. S. S.; Levitskaia, C. H. T.; Thallapally, J. M. P.; Weber, R. S. W.; ichard Zheng, R., Processes for removal and immobilization of ^{14}C, ^{129I}, and ^{85}Kr. ***Report PNNL Pacific Northwest National Laboratory, Richland, WA*** 2009.

35. Gao, F.; Weber, W. J., Recovery of close Frenkel pairs produced by low energy recoils in SiC. ***J. Nucl. Mater.*** 2003, *94* (7), 4348-4356.

36. Cheng, T.; Baney, R. H.; Tulenko, J., The effects of oxygen, carbon dioxide and water vapor on reprocessing silicon carbide inert matrix fuels by corrosion in molten potassium carbonate. ***J. Nucl. Mater.*** 2011, *411* (1), 126-130.

37. Grover, B.; Maki, J.; Petti, D. *Completion of the first NGNP advanced gas reactor fuel irradiation experiment, AGR-1, in the Advanced Test Reactor*; ***Idaho National Laboratory (INL)***: 2010.

38. Zinkle, S. J., Fusion materials science: Overview of challenges and recent progress. ***Phys. Plasmas*** 2005, *12* (5), 058101.

39. Giancarli, L.; Golfier, H.; Nishio, S.; Raffray, R.; Wong, C.; Yamada, R., Progress in blanket designs using SiC f/SiC composites. ***Fusion Eng. Des.*** 2002, *61*, 307-318.

40. Sawan, M.; Katoh, Y.; Snead, L. L., Transmutation of silicon carbide in fusion nuclear environment. ***J. Nucl. Mater.*** 2013, *442* (1), S370-S375.

41. Sawan, M.; Snead, L.; Zinkle, S., Radiation damage parameters for SiC/SiC composite structure in fusion nuclear environment. ***Fusion Sci. Tech.*** 2003, *44* (1), 150-154.

42. Katoh, Y.; Kondo, S.; Snead, L. L., DC electrical conductivity of silicon carbide ceramics and composites for flow channel insert applications. ***J. Nucl. Mater.*** 2009, *386*, 639-642.

43. Handy, E. M.; Rao, M. V.; Holland, O.; Jones, K.; Derenge, M.; Papanicolaou, N., Variable-dose (10^{17}–10^{20} cm^{-3}) phosphorus ion implantation into 4H–SiC. ***J. App. Phys.*** 2000, *88* (10), 5630-5634.

44. Costello, J.; Tressler, R., Oxygen penetration into silicon carbide ceramics during oxidation. ***Ceram. Int.*** 1985, *11* (2), 39-44.

45. Katoh, Y.; Snead, L. L.; Parish, C. M.; Hinoki, T., Observation and possible mechanism of irradiation induced creep in ceramics. ***J. Nucl. Mater.*** 2013, *434* (1-3), 141-151.

46. Bockstedte, M.; Mattausch, A.; Pankratov, O., Ab initio study of the migration of intrinsic defects in 3C−SiC. ***Phys. Rev. B*** 2003, *68* (20), 205201.

47. Zhang, Y.; Sachan, R.; Pakarinen, O. H.; Chisholm, M. F.; Liu, P.; Xue, H.; Weber, W. J., Ionization-induced annealing of pre-existing defects in silicon carbide. ***Nature commun.*** 2015, *6*.

48. Steeds, J. W.; Evans, G. A.; Danks, L. R.; Furkert, S.; Voegeli, W.; Ismail, M. M.; Carosella, F., Transmission electron microscope radiation damage of 4H and 6H SiC studied by photoluminescence spectroscopy. ***Diam Relat Mater*** 2002, *11* (12), 1923-1945.

49. Was, G. S., *Fundamentals of radiation materials science: metals and alloys*. ***Springer*****:** 2016.

50. Devanathan, R.; Weber, W.; Gao, F., Atomic scale simulation of defect production in irradiated 3C-SiC. ***J. Appl. Phys.*** 2001, *90* (5), 2303-2309.

51. Gao, F.; Weber, W. J.; Devanathan, R., Atomic-scale simulation of displacement cascades and amorphization in β-SiC. ***Nucl. Instrum. Meth. B*** 2001, *180* (1), 176-186.

52. Jiang, C.; Morgan, D.; Szlufarska, I., Structures and stabilities of small carbon interstitial clusters in cubic silicon carbide. ***Acta Mater.*** 2014, *62*, 162-172.

53. Liu, C.; Szlufarska, I., Formation of interstitial clusters in SiC during cascade ***In preparation***.

54. Swaminathan, N.; Morgan, D.; Szlufarska, I., Ab initio based rate theory model of radiation induced amorphization in β-SiC. ***J. Nucl. Mater.*** 2011, *414* (3), 431-439.

55. Swaminathan, N.; Wojdyr, M.; Morgan, D. D.; Szlufarska, I., Radiation interaction with tilt grain boundaries in β-SiC. ***J. Appl. Phys.*** 2012, *111* (5), 054918.

56. Hodgson, E.; Malo, M.; Manzano, J.; Moroño, A.; Hernandez, T., Radiation induced modification of electrical conductivity for three types of SiC. ***J. Nucl, Mater.*** 2011, *417* (1), 421-424.

57. Madar, R., Materials science: Silicon carbide in contention. ***Nature*** 2004, *430* (7003), 974-975.

58. Casady, J. B.; Johnson, R. W., Status of silicon carbide (SiC) as a wide-bandgap semiconductor for high-temperature applications: A review. ***Solid State Electron*** 1996, *39* (10), 1409-1422.

59. Agarwal, S. E. S. a. A., *Advances in Silicon Carbide Processing and Applications*. ***Artech House*****:** 2004.

60. Patrick, L.; Choyke, W., Localized vibrational modes of a persistent defect in ion-implanted SiC. ***J. Phys. Chem. Solids*** 1973, *34* (3), 565-567.

61. Sridhara, S. G.; Nizhner, D. G.; Devaty, R. P.; Choyke, W. J.; Dalibor, T.; Pensl, G.; Kimoto, T., D_{II} revisited in an modern guise - 6H- and 4H-SiC. ***Mater. Sci. Forum*** 1998, *264-2*, 493-496.

62. Sridhara, S. G.; Carlsson, F. H. C.; Bergman, J. P.; Henry, A.; Janzen, E., Investigation of an Ion-Implantation Induced High Temperature Persistent Intrinsic Defect in SiC. ***Mater. Sci. Forum*** 2001, *353-356*, 377-380.

63. Gavrikov, A.; Knizhnik, A.; Safonov, A.; Scherbinin, A.; Bagatur'yants, A.; Potapkin, B.; Chatterjee, A.; Matocha, K., First-principles-based investigation of kinetic mechanism of SiC (0001) dry oxidation including defect generation and passivation. ***J. Appl. Phys.*** 2008, *104* (9), 093508.

64. Shen, X.; Pantelides, S. T., Identification of a major cause of endemically poor mobilities in SiC/SiO 2 structures. ***Appl. Phys. Lett.*** 2011, *98* (5), 053507.

65. Shen, X.; Oxley, M. P.; Puzyrev, Y.; Tuttle, B.; Duscher, G.; Pantelides, S. T., Excess carbon in silicon carbide. ***J. Appl. Phys.*** 2010, *108* (12), 123705.

66. Alfieri, G.; Kimoto, T., Capacitance spectroscopy study of deep levels in Cl-implanted 4H-SiC. ***J. Appl. Phys.*** 2012, *112* (6), 063717.

67. Snead, L.; Zinkle, S.; Hay, J.; Osborne, M., Amorphization of SiC under ion and neutron irradiation. ***Nucl. Instrum. Meth. B*** 1998, *141* (1), 123-132.

68. Katoh, Y.; Kondo, S.; Snead, L. L., Microstructures of beta-silicon carbide after irradiation creep deformation at elevated temperatures. ***J. Nucl. Mater.*** 2008, *382* (2-3), 170-175.

69. Tyburska-Püschel, B.; Zhai, Y.; He, L.; Liu, C.; Boulle, A.; Voyles, P.; Szlufarska, I.; Sridharan, K., Size distribution of black spot defects and their contribution to swelling in irradiated SiC. ***J. Nucl, Mater.*** 2016, *476*, 132-139.

70. Katoh, Y.; Snead, L. L. In *Mechanical properties of cubic silicon carbide after neutron irradiation at elevated temperatures*, Effects of Radiation on Materials: 22nd Symposium, ***ASTM International***: 2006.

71. Katoh, Y.; Snead, L. L.; Golubov, S. I., Analyzing irradiation-induced creep of silicon carbide. ***Mech. Prop. Perf. Eng .Ceram. Comp. III*** 2007, *28*, 297-306.

72. Gittus, J., Theory of dislocation-creep due to the frenkel defects or interstitialcies produced by bombardment with energetic particles. ***Philos. Mag.*** 1972, *25* (2), 345-354.

73. Torpo, L.; Marlo, M.; Staab, T.; Nieminen, R., Comprehensive ab initio study of properties of monovacancies and antisites in 4H-SiC. ***J. Phys.-Condens. Mat.*** 2001, *13* (28), 6203.

74. Baranov, P. G.; Soltamov, V. A.; Soltamova, A. A.; Astakhov, G. V.; Dyakonov, V. D. In *Point defects in SiC as a promising basis for single-defect, single-photon spectroscopy with room temperature controllable quantum states*, Materials Science Forum, ***Trans Tech Publ***: 2013; pp 425-430.

75. Zheng, M. J.; Swaminathan, N.; Morgan, D.; Szlufarska, I., Energy barriers for point-defect reactions in 3C-SiC. ***Phys Rev B*** 2013, *88* (5).

76. Alfieri, G.; Monakhov, E.; Svensson, B.; Linnarsson, M. K., Annealing behavior between room temperature and 2000° C of deep level defects in electron-irradiated n-type 4H silicon carbide. ***J. Appl. Phys.*** 2005, *98* (4), 043518.

77. He, L.; Jiang, H.; Zhai, Y.; Liu, C.; Szlufarska, I.; Tyburska-Puschel, B.; Sridharan, K.; Voyles, P., Atomic Resolution Imaging of Black Spot Defects in Ion Irradiated Silicon Carbide. ***Microscopy and Microanalysis*** 2015, *21* (S3), 1337-1338.

78. Price, R., Neutron irradiation-induced voids in β-silicon carbide. ***J. Nucl, Mater.*** 1973, *48* (1), 47-57.

79. Li, W.; Zhao, J.; Wang, D., An amorphous SiO_2/4H-SiC (0001) interface: Band offsets and accurate charge transition levels of typical defects. ***Solid State Commun.*** 2015, *205*, 28-32.

80. Ettisserry, D.; Salemi, S.; Goldsman, N.; Potbhare, S.; Akturk, A.; Lelis, A. In *Identification and quantification of 4H-SiC (0001)/SiO 2 interface defects by combining density functional and device simulations*, Simulation of Semiconductor Processes and Devices (SISPAD), 2013 International Conference on, ***IEEE***: 2013; pp 396-399.

81. Iskandarova, I.; Khromov, K.; Knizhnik, A.; Potapkin, B., The role of neutral point defects in carrier mobility degradation in bulk 4H-SiC and at 4H-SiC/SiO2 interface: First-principles investigation using Green's functions. ***J. Appl. Phys.*** 2015, *117* (17), 175703.

82. Mattausch, A.; Bockstedte, M.; Pankratov, O., Interstitials in SiC: a model for the DII center. ***Physica B*** 2001, *308*, 656-659.

83. Mattausch, A.; Bockstedte, M.; Pankratov, O., Carbon antisite clusters in SiC: A possible pathway to the DII center. ***Phys. Rev. B*** 2004, *69* (4), 045322.

84. Mattausch, A.; Bockstedte, M.; Pankratov, O., Structure and vibrational spectra of carbon clusters in SiC. ***Phys. Rev. B*** 2004, *70* (23), 235211.

85. Ko, H.; Kaczmarowski, A.; Szlufarska, I.; Morgan, D., Optimization of self-interstitial clusters in 3C-SiC with genetic algorithm. ***J. Nucl, Mater.*** 2017.

86. Watanabe, Y.; Morishita, K.; Kohyama, A., Composition dependence of formation energy of self-interstitial atom clusters in β-SiC: Molecular dynamics and molecular statics calculations. ***J. Nucl. Mater.*** 2011, *417* (1), 1119-1122.

87. Kiritani, M., Electron radiation induced diffusion of point defects in metals. ***J. Phys. Soc. Jap.*** 1976, *40* (4), 1035-1042.

88. Kotakoski, J.; Mangler, C.; Meyer, J. C., Imaging atomic-level random walk of a point defect in graphene. ***Nature commun.*** 2014, *5*.

89. Kotakoski, J.; Krasheninnikov, A.; Kaiser, U.; Meyer, J., From point defects in graphene to two-dimensional amorphous carbon. ***Phys. Rev. Lett.*** 2011, *106* (10), 105505.

90. Kotakoski, J.; Meyer, J.; Kurasch, S.; Santos-Cottin, D.; Kaiser, U.; Krasheninnikov, A., Stone-Wales-type transformations in carbon nanostructures driven by electron irradiation. ***Phys. Rev. B*** 2011, *83* (24), 245420.

91. Nepijko, S. A.; Klimenkov, M.; Kuhlenbeck, H.; Freund, H.-J., Transmission electron microscopy study of platinum clusters on Al2O3/NiAl„110… under the influence of electron irradiation. ***J. Vac. Sci. Technol. A*** 1998, *17*.

92. Kondo, S.; Katoh, Y.; Snead, L. L., Analysis of grain boundary sinks and interstitial diffusion in neutron-irradiated SiC. ***Phys. Rev. B*** 2011, *83* (7), 075202.

93. Jiang, C.; Swaminathan, N.; Deng, J.; Morgan, D.; Szlufarska, I., Effect of grain boundary stresses on sink strength. ***Mater. Res. Lett.*** 2014, *2* (2), 100-106.

94. Vattré, A.; Jourdan, T.; Ding, H.; Marinica, M.-C.; Demkowicz, M., Non-random walk diffusion enhances the sink strength of semicoherent interfaces. ***Nature Commun.*** 2016, *7*.

95. Bai, X.-M.; Voter, A. F.; Hoagland, R. G.; Nastasi, M.; Uberuaga, B. P., Efficient annealing of radiation damage near grain boundaries via interstitial emission. ***Science*** 2010, *327* (5973), 1631-1634.

96. Shen, T. D.; Feng, S.; Tang, M.; Valdez, J. A.; Wang, Y.; Sickafus, K. E., Enhanced radiation tolerance in nanocrystalline MgGa2O4. ***Appl. Phys. Lett.*** 2007, *90* (26), 263115-263500.

97. Han, W.; Demkowicz, M. J.; Mara, N. A.; Fu, E.; Sinha, S.; Rollett, A. D.; Wang, Y.; Carpenter, J. S.; Beyerlein, I. J.; Misra, A., Design of radiation tolerant materials via interface engineering. ***Advanced materials*** 2013, *25* (48), 6975-6979.

98. Jiang, W.; Wang, H.; Kim, I.; Zhang, Y.; Weber, W. J., Amorphization of nanocrystalline 3C-SiC irradiated with Si^{+} ions. ***J. Mater. Res.*** 2010, *25* (12), 2341-2348.

99. Jiang, W.; Jiao, L.; Wang, H., Transition from Irradiation-Induced Amorphization to Crystallization in Nanocrystalline Silicon Carbide. ***J. Am. Ceram. Soc.*** 2011, *94* (12), 4127-4130.

100. Jamison, L.; Sridharan, K.; Shannon, S.; Szlufarska, I., Temperature and irradiation species dependence of radiation response of nanocrystalline silicon carbide. ***J. Mater. Res.*** 2014, *29* (23), 2871-2880.

101. Zhang, Y.; Ishimaru, M.; Varga, T.; Oda, T.; Hardiman, C.; Xue, H.; Katoh, Y.; Shannon, S.; Weber, W. J., Nanoscale engineering of radiation tolerant silicon carbide. ***Phys. Chem. Chem. Phys.*** 2012, *14* (38), 13429-13436.

102. Jamison, L.; Zheng, M.-J.; Shannon, S.; Allen, T.; Morgan, D.; Szlufarska, I., Experimental and ab initio study of enhanced resistance to amorphization of nanocrystalline silicon carbide under electron irradiation. ***J. Nucl. Mater.*** 2014, *445* (1), 181-189.

103. Wang, X.; Jamison, L.; Sridharan, K.; Morgan, D.; Voyles, P.; Szlufarska, I., Evidence for cascade overlap and grain boundary enhanced amorphization in silicon carbide irradiated with Kr ions. ***Acta Mater.*** 2015, *99*, 7-15.

104. Tschopp, M. A.; Solanki, K.; Gao, F.; Sun, X.; Khaleel, M. A.; Horstemeyer, M., Probing grain boundary sink strength at the nanoscale: Energetics and length scales of vacancy and interstitial absorption by grain boundaries in α-Fe. ***Phys. Rev. B*** 2012, *85* (6), 064108.

105. Uberuaga, B. P.; Vernon, L. J.; Martinez, E.; Voter, A. F., The relationship between grain boundary structure, defect mobility, and grain boundary sink efficiency. ***Sci. Rep.*** 2015, *5*, 9095.

106. Bhatia, M.; Solanki, K., Energetics of vacancy segregation to symmetric tilt grain boundaries in hexagonal closed pack materials. ***J. App. Phys.*** 2013, *114* (24), 244309.

107. Suzuki, A.; Mishin, Y., Atomistic modeling of point defects and diffusion in copper grain boundaries. ***Interface Sci.*** 2003, *11* (1), 131-148.

108. Kapikranian, O.; Zapolsky, H.; Patte, R.; Pareige, C.; Radiguet, B.; Pareige, P., Point defect absorption by grain boundaries in α-iron by atomic density function modeling. ***Phys. Rev. B*** 2015, *92* (22), 224106.

109. Suzuki, A.; Mishin, Y., Atomic mechanisms of grain boundary diffusion: Low versus high temperatures. ***J. Mater. Sci.*** 2005, *40* (12), 3155-3161.

110. Suzuki, A.; Mishin, Y., Interaction of point defects with grain boundaries in fcc metals. ***Interface Sci.*** 2003, *11* (4), 425-437.

111. Esfandiarpour, A.; Feghhi, S.; Shokri, A., Effects of atomic grain boundary structures on primary radiation damage in α-Fe. ***Nucl. Instrum. Meth. B*** 2015, *362*, 1-8.

112. Novoselov, I.; Yanilkin, A., Impact of segregated interstitials on structures and energies of tilt grain boundaries in Mo. ***Comp. Mater. Sci.*** 2016, *112*, 276-281.

113. Foley, D.; Tucker, G. J., Quantifying grain boundary damage tolerance with atomistic simulations. ***Model. Simul. Mater. Sci.*** 2016, *24* (7), 075011.

114. Yu, W.; Demkowicz, M., Non-coherent Cu grain boundaries driven by continuous vacancy loading. ***J. Mater. Sci.*** 2015, *50* (11), 4047-4065.

115. Frolov, T.; Olmsted, D. L.; Asta, M.; Mishin, Y., Structural phase transformations in metallic grain boundaries. ***Nat. Commun.*** 2013, *4*, 1899.

116. Jiang, H.; Wang, X.; Szlufarska, I., The multiple roles of small-angle tilt grain boundaries in annihilating radiation damage in SiC. ***Sci. Rep.*** 2017, *7*, 42358.

117. Millett, P. C.; Aidhy, D. S.; Desai, T.; Phillpot, S. R.; Wolf, D., Grain-boundary source/sink behavior for point defects: an atomistic simulation study. ***Int. J. Mater.Res.*** 2009, *100* (4), 550-555.

118. Martínez, E.; Hirth, J. P.; Nastasi, M.; Caro, A., Structure of a 2◦ (010) Cu twist boundary interface and the segregation of vacancies and He atoms. ***Phys. Rev. B*** 2012, *85* (6), 060101.

119. Martínez, E.; Caro, A., Atomistic modeling of long-term evolution of twist boundaries under vacancy supersaturation. ***Phys. Rev. B*** 2012, *86* (21), 214109.

120. Martin, R. M., *Electronic structure: basic theory and practical methods*. ***Cambridge university press*****:** 2004.

121. Kresse, G.; Joubert, D., From ultrasoft pseudopotentials to the projector augmented-wave method. ***Phys Rev B*** 1999, *59* (3), 1758.

122. Sheppard, D.; Terrell, R.; Henkelman, G., Optimization methods for finding minimum energy paths. ***J. Chem. Phys.*** 2008, *128* (13), 134106.

123. Henkelman, G.; Uberuaga, B. P.; Jónsson, H., A climbing image nudged elastic band method for finding saddle points and minimum energy paths. ***J. Chem. Phys.*** 2000, *113* (22), 9901-9904.

124. Frenkel, D.; Smit, B., *Understanding molecular simulation: from algorithms to applications*. ***Academic press*****:** 2001; Vol. 1.

125. Stillinger, F. H.; Weber, T. A., Computer simulation of local order in condensed phases of silicon. ***Phys. Rev. B*** 1985, *31* (8), 5262.

126. Tersoff, J., Modeling solid-state chemistry: Interatomic potentials for multicomponent systems. ***Phys. Rev. B*** 1989, *39* (8), 5566.

127. Erhart, P.; Albe, K., Analytical potential for atomistic simulations of silicon, carbon, and silicon carbide. ***Phys. Rev. B*** 2005, *71* (3), 035211.

128. Lucas, G.; M, B.; L, P., An environment-dependent interatomic potential for silicon carbide: calculation of bulk prpperties, high pressure phases, point and extended defects, and amorphous structures. ***J. Phys.: Condens. Matter*** 2010, *22* (3).

129. Vashishta, P.; Kalia, R. K.; Nakano, A.; Rino, J. P., Interaction potential for silicon carbide: a molecular dynamics study of elastic constants and vibrational density of states for crystalline and amorphous silicon carbide. ***J. Appl. Phys.*** 2007, *101* (10), 103515.

130. Gao, F.; Weber, W. J., Empirical potential approach for defect properties in 3C-SiC. ***Nucl. Instrum. Meth. B*** 2002, *191* (1), 504-508.

131. Lambrecht, W.; Segall, B.; Methfessel, M.; Van Schilfgaarde, M., Calculated elastic constants and deformation potentials of cubic SiC. ***Phys. Rev. B*** 1991, *44* (8), 3685.

132. Kamitani, K.; Grimsditch, M.; Nipko, J.; Loong, C.-K.; Okada, M.; Kimura, I., The elastic constants of silicon carbide: A Brillouin-scattering study of 4H and 6H SiC single crystals. ***J. Appl. Phys.*** 1997, *82* (6), 3152-3154.

133. Tsuzuki, H.; Branicio, P. S.; Rino, J. P., Structural characterization of deformed crystals by analysis of common atomic neighborhood. ***Comput. Phys. Commun.*** 2007, *177* (6), 518-523.

134. Stukowski, A.; Bulatov, V. V.; Arsenlis, A., Automated identification and indexing of dislocations in crystal interfaces. ***Model. Simul. Mater. Sci.*** 2012, *20* (8), 085007.

135. Voter, A. F., Parallel replica method for dynamics of infrequent events. ***Phys. Rev. B*** 1998, *57* (22), 13985-13988.

136. Voter, A. F., A method for accelerating the molecular dynamics simulation of infrequent events. ***J. Chem. Phys.*** 1997, *106*, 4665-4677.

137. Sorensen, M. R.; Voter, A. F., Temperature-accelerated dynamics for simulation of infrequent events. ***J. Chem. Phys.*** 2000, *112* (21), 9599-9606.

138. Jónsson, G. H. a. H., A dimer method for finding saddle points on high dimensional ptential surfaces using only first derivatives. ***J. Chem. Phys.*** 1999, *111* (15), 7010-7022.

139. Mousseau, N.; Beland, L. K.; Brommer, P.; Joly, J.-F.; EI-Mellouhi, F.; Machado-Charry, E.; Marinica, M.-C.; Pochet, P., The Activation-Relaxation Technique: ART Nouveau and Kinetic ART. ***J. At., Mol. Opt. Phys.*** 2012, *2012*.

140. Barkema, G. T.; Mousseau, N., Event-Based Relaxation of Continuous Disordered Systems. ***Phys. Rev. Lett.*** 1996, *77* (21), 4358-4361.

141. Malek, R.; Mousseau, N., Dynamics of Lennard-Jones clusters: A characterization of the activation-relaxation technique. ***Phys. Rev. E*** 2000, *62* (6), 7723-7728.

142. Cances, E.; Legoll, F.; Marinica, M.-C.; Minoukadeh, K.; Willaime, F., Some improvements of the activation-relaxation technique method for finding transition pathways on potential energy surfaces. ***J. Chem. Phys.*** 2009, *130* (11).

143. Eduardo, M.-C.; Beland, L. K.; Caliste, D.; Genovese, L.; Deutsch, T.; Mousseau, N.; Pochet, P., Optimized energy landscape exploration using the ab initio based activation-relaxation technique. ***J. Chem. Phys.*** 2011, *135* (3).

144. Kushima, A.; Lin, X.; Li, J.; Eapen, J.; Mauro, J. C.; Qian, X.; Diep, P.; Yip, S., Computing the viscosity of supercooled liquids. ***J. Chem. Phys.*** 2009, *130* (22).

145. Jiang, C.; Morgan, D.; Szlufarska, I., Carbon tri-interstitial defect: A model for the D_{II} center. ***Phys. Rev. B*** 2012, *86* (14).

146. Schuh, D. R. a. C. A., Yield stress in metallic glasses: The jamming-unjamming transition studied through Monter Carlo simulations based on the activation-relaxation technique. ***Phys. Rev. B*** 2009, *80* (18).

147. Joubert, G. K. a. D., From ultrasoft pseudopotentials to the projector augmented-wave method. ***Phys. Rev. B*** 1999, *59*, 1758-1775.

148. Carlsson, F. H. C.; Sridhara, S. G.; Hallen, A.; Bergman, H. P.; Janzen, E., D_{II} PL Intensity Dependence on Dose, Implantation Temperature and Inplanted Species in 4H- and 6H-SiC. ***Mater. Sci. Forum*** 2003, *433-436*, 345-348.

149. Sullivan, W.; Steeds, J. W., A Study of the DII Defect after Electron Irradiation and Annealing of 4H SiC. ***Mater. Sci. Forum*** 2007, *556-557*, 319-322.

150. Ziegler, J. F., SRIM-2003. ***Nucl. Instrum. Methods Phys. Res. B*** 2004, *219*, 1027-1036.

151. Yankovich, A. B.; Berkels, B.; Dahmen, W.; Binev, P.; Sanchez, S.; Bradley, S.; Li, A.; Szlufarska, I.; Voyles, P. M., Picometre-precision analysis of scanning transmission electron microscopy images of platinum nanocatalysts. ***Nature Commun.*** 2014, *5*, 4155.

152. Muller, D. A.; Nakagawa, N.; Ohtomo, A.; Grazul, J. L.; Hwang, H. Y., Atomic-scale imaging of nanoengineered oxygen vacancy profiles in SrTiO3. ***Nature*** 2004, *430* (7000), 657-661.

153. Zinkle, S., Effect of irradiation spectrum on the microstructural evolution in ceramic insulators. ***J. Nucl. Mater.*** 1995, *219*, 113-127.

154. Yasuda, K.; Kinoshita, C.; Morisaki, R.; Abe, H., Role of irradiation spectrum in the microstructural evolution of magnesium aluminate spinel. ***Philos. Mag. A*** 1998, *78* (3), 583-598.

155. Hirano, R.; Sato, Y.; Tsuchida, H.; Tajima, M.; Itoh, K. M.; Maeda, K., Photoluminescence Study of Radiation-Enhanced Dislocation Glide in 4H-SiC. ***Appl. Phys. Express*** 2012, *5* (9), 091302.

156. Pandya, C., Total ionization cross-sections for Si2, SiC, SiC2 and Si2C molecules. ***J. Phy. Conf. Ser.*** 2014, *488* (5), 052001.

157. Lee, J.; Zhou, W.; Pennycook, S. J.; Idrobo, J.-C.; Pantelides, S. T., Direct visualization of reversible dynamics in a Si6 cluster embedded in a graphene pore. ***Nature commun.*** 2013, *4*, 1650.

158. Meyer, J. C.; Eder, F.; Kurasch, S.; Skakalova, V.; Kotakoski, J.; Park, H. J.; Roth, S.; Chuvilin, A.; Eyhusen, S.; Benner, G., Accurate measurement of electron beam induced displacement cross sections for single-layer graphene. ***Phys. Rev. Lett.*** 2012, *108* (19), 196102.

159. Jiang, H.; Jiang, C.; Morgan, D.; Szlufarska, I., Accelerated atomistic simulation study on the stability and mobility of carbon tri-interstitial cluster in cubic SiC. ***Comp. Mater. Sci.*** 2014, *89*, 182-188.

160. Devanathan, R.; Weber, W. J., Displacement energy surface in 3C and 6H SiC. ***J. Nucl. Mater.*** 2000, *278* (2), 258-265.

161. Rajagopalan, M.; Tschopp, M.; Solanki, K., Grain boundary segregation of interstitial and substitutional impurity atoms in alpha-iron. ***JOM*** 2014, *66* (1), 129-138.

162. Liu, C.; He, L.; Zhai, Y.; Tyburska-Püschel, B.; Voyles, P.; Sridharan, K.; Morgan, D.; Szlufarska, I., Evolution of small defect clusters in ion-irradiated 3C-SiC: combined cluster dynamics modeling and experimental study. ***Acta Mater.*** 2017, *125*, 377-389.

163. Arakawa, K.; Ono, K.; Isshiki, M.; Mimura, K.; Uchikoshi, M.; Mori, H., Observation of the one-dimensional diffusion of nanometer-sized dislocation loops. ***Science*** 2007, *318* (5852), 956-959.

164. Matsukawa, Y.; Zinkle, S. J., One-dimensional fast migration of vacancy clusters in metals. ***Science*** 2007, *318* (5852), 959-962.

165. Satoh, Y.; Abe, H.; Matsunaga, T., Radiation-induced glide motion of interstitial clusters in concentrated alloys. ***Philos. Mag.*** 2014, *94* (19), 2170-2187.

166. Osetsky, Y. N.; Bacon, D.; Serra, A.; Singh, B.; Golubov, S., Stability and mobility of defect clusters and dislocation loops in metals. ***J. Nucl. Mater.*** 2000, *276* (1), 65-77.

167. Razumovskiy, V. I.; Ruban, A. V.; Odqvist, J.; Korzhavyi, P. A., Vacancy-cluster mechanism of metal-atom diffusion in substoichiometric carbides. ***Phys. Rev. B*** 2013, *87* (5), 054203.

168. Zobelli, A.; Ewels, C.; Gloter, A.; Seifert, G., Vacancy migration in hexagonal boron nitride. ***Phys. Rev. B*** 2007, *75* (9), 094104.

169. Sullivan, W.; Steeds, J. W., A Study of the DII Defect after Electron Irradiation and Annealing of 4H SiC. ***Mater. Sci. Forum*** 2007, *556*, 319-322.

170. Beyerlein, I. J.; Demkowicz, M. J.; Misra, A.; Uberuaga, B. P., Defect-interface interactions. ***Prog. Mater. Sci.*** 2015, *74*, 125-210.

171. Snead, L. L.; Katoh, Y.; Kondo, S., Effects of fast neutron irradiation on zirconium carbide. ***J. Nucl. Mater.*** 2010, *399* (2), 200-207.

172. Voronoï, G., Nouvelles applications des paramètres continus à la théorie des formes quadratiques. ***J. Reine. Angew. Math.*** 1908, *134*, 198-287.

173. Nazarov, A.; Shenderova, O.; Brenner, D. W., Elastic models of symmetrical< 001> and< 011> tilt grain boundaries in diamond. ***Phys. Rev. B*** 2000, *61* (2), 928.

174. Zhang, J.; Wang, C.-Z.; Ho, K.-M., Finding the low-energy structures of Si [001] symmetric tilted grain boundaries with a genetic algorithm. ***Phys. Rev. B*** 2009, *80* (17), 174102.

175. Gao, F.; Weber, W. J.; Posselt, M.; Belko, V., Atomistic study of intrinsic defect migration in 3C-SiC. ***Phys. Rev. B*** 2004, *69*, 245205.

176. Huang, J.; Meyer, M.; Pontikis, V., Is pipe diffusion in metals vacancy controlled? a molecular dynamics study of an edge dislocation in copper. ***Phys. Rev. Lett.*** 1989, *63* (6), 628.

177. Mishin, Y.; Gust, W., Grain boundary diffusion metals versus non-stoichiometric compounds. ***Ionics*** 2001, *7* (4-6), 247-263.

178. Picu, R.; Zhang, D., Atomistic study of pipe diffusion in Al–Mg alloys. ***Acta Mater.*** 2004, *52* (1), 161-171.

179. Ziebarth, B.; Mrovec, M.; Elsässer, C.; Gumbsch, P., Influence of dislocation strain fields on the diffusion of interstitial iron impurities in silicon. ***Phys. Rev. B*** 2015, *92* (11), 115309.

180. Petroff, P.; Kimerling, L., Dislocation climb model in compound semiconductors with zinc blende structure. ***Appl. Phys. Lett.*** 1976, *29* (8), 461-463.

181. Petroff, P., Point defects and dislocation climb in III-V compounds semiconductors. ***Le Journal de Physique Colloques*** 1979, *40* (C6), C6-201-C6-205.

182. Adlakha, I.; Solanki, K., Structural stability and energetics of grain boundary triple junctions in face centered cubic materials. ***Sci. Rep.*** 2015, *5*, 8692.

183. Jamison, L.; Xu, P.; Sridharan, K.; Allen, T. In *Radiation resistance of nanocrystalline silicon carbide*, Advances in Materials Science for Environmental and Nuclear Technology II-Materials Science and Technology 2010 Conference and Exhibition, MS and T'10, 2011; p 161.

184. Jiang, W.; Wang, H.; Kim, I.; Bae, I.-T.; Li, G.; Nachimuthu, P.; Zhu, Z.; Zhang, Y.; Weber, W. J., Response of nanocrystalline 3C silicon carbide to heavy-ion irradiation. ***Phys. Rev. B*** 2009, *80* (16), 161301.

185. Ishimaru, M.; Zhang, Y.; Shannon, S.; Weber, W. J., Origin of radiation tolerance in 3C-SiC with nanolayered planar defects. ***Appl. Phys. Lett.*** 2013, *103* (3), 033104.

186. Bakaev, A.; Terentyev, D.; Grigor'ev, P. Y.; Zhurkin, E., Interaction between mobile dislocations and perfect dislocation loops in Fe-Ni-Cr austenitic alloy systems. ***J. Surf. Investig-X-ra*** 2015, *9* (2), 290-299.

187. Balluffi, R., Mechanisms of dislocation climb. ***Phys. Stat. Sol.*** 1969, *31* (2), 443-463.

188. Rodney, D., Atomic modeling of irradiation-induced hardening. ***CR Phys.*** 2008, *9* (3), 418-426.

189. Serra, A.; Bacon, D., Atomic-level computer simulation of the interaction between 1/3 <11-20> {1-100} dislocations and 1/3 <11-20> interstitial loops in α-zirconium. ***Model. Simul. Mater. Sci.*** 2013, *21* (4), 45007-45021.

190. Rodney, D., Molecular dynamics simulation of screw dislocations interacting with interstitial frank loops in a model FCC crystal. ***Acta Mater.*** 2004, *52* (3), 607-614.

191. Di, Z.; Bai, X.-M.; Wei, Q.; Won, J.; Hoagland, R. G.; Wang, Y.; Misra, A.; Uberuaga, B. P.; Nastasi, M., Tunable helium bubble superlattice ordered by screw dislocation network. ***Phys. Rev. B*** 2011, *84* (5), 052101.

192. Deng, J.; Morgan, D.; Szlufarska, I., Kinetic Monte Carlo simulation of the effective diffusivity in grain boundary networks. ***Comp. Mater. Sci.*** 2014, *93*, 36-45.

193. Maras, E.; Trushin, O.; Stukowski, A.; Ala-Nissila, T.; Jonsson, H., Global transition path search for dislocation formation in Ge on Si (001). ***Comp. Phys. Commun.*** 2016, *205*, 13-21.

194. Dai, S.; Xiang, Y.; Srolovitz, D. J., Structure and energy of (111) low-angle twist boundaries in Al, Cu and Ni. ***Acta Mater.*** 2013, *61* (4), 1327-1337.

195. Dai, S.; Xiang, Y.; Srolovitz, D. J., Atomistic, generalized Peierls–Nabarro and analytical models for (111) twist boundaries in Al, Cu and Ni for all twist angles. ***Acta Mater.*** 2014, *69*, 162-174.

196. Käckell, P.; Furthmüller, J.; Bechstedt, F., Stacking faults in group-IV crystals: An ab initio study. ***Phys. Rev. B*** 1998, *58* (3), 1326.

197. Lindefelt, U.; Iwata, H.; Öberg, S.; Briddon, P. R., Stacking faults in 3C−, 4H−, and 6H−SiC polytypes investigated by an ab initio supercell method. ***Phys. Rev. B*** 2003, *67* (15), 155204.

198. Kohl, H.; Reimer, L., *Transmission Electron Microscopy: Physics of Image Formation*. ***Springer-Verlag New York*****:** 2008.

199. Jablonski, A.; Salvat, F.; Powell, C. J., *NIST Electron Elastic-Scattering Cross-Section Database - Version 3.2*. ***National Institute of Standards and Technology, Gaithersburg, MD*****:** 2010.

200. Salvat, F.; Jablonski, A.; Powell, C. J., ELSEPA—Dirac partial-wave calculation of elastic scattering of electrons and positrons by atoms, positive ions and molecules. ***Comp. Phys. Commun.*** 2005, *165* (2), 157-190.

201. Yan, Q.; Wang, J.; Chen, D.; Gigax, J.; Shao, L., Displacement cross sections of electron irradiated graphene and carbon nanotubes. ***Nucl. Instrum. Meth. B*** 2015, *350*, 20-25.

202. Kirkland, E. J., *Advanced computing in electron microscopy*. ***Springer Science & Business Media*****:** 2010.

203. Capitani, G. C.; Di Pierro, S.; Tempesta, G., The 6H-SiC structure model: Further refinement from SCXRD data from a terrestrial moissanite. ***Am. Mineral.*** 2007, *92* (2-3), 403-407.